IN THE UNITED STATES PATENT AND TRADEMARK OFFICE

Applicant(s): He, et al. Application No.: 10/582,820 Filed: 10/8/2008 Title: Single Molecule Detection Using Molecular Motors Attorney Docket No.: 60224US	Confirmation No. **7416** Art Unit: 1634 Examiner: SISSON, BRADLEY L

Commissioner for Patents
P.O. Box 1450
Alexandria, VA 22313-1450

STATEMENT UNDER 37 C.F.R. § 1.132

Dear Commissioner:

1. I, Wayne Frasch, Ph.D. do state:

2. I am an inventor of the subject matter which is claimed and for which a patent is sought in the above-identified patent application which is a national phase entry of the international patent filed on 12/17/2004 as PCT International Application Number PCT/US04/42358 corresponding to US Application No. 10/582,820.

3. I joined the faculty at Arizona State University in fall 1989 where I am now a Professor in the faculty of Biomedicine and Biotechnology and a member of the ASU Center for the Study of Early Events in Photosynthesis.

4. I previously held a faculty position at the University of Michigan in Ann Arbor, and was a visiting research scientist at the Mayo Clinic. I have served on NIH study sections for Physical Biochemistry and for Biophysics and Biochemistry of Membranes, and have

been a Fellow of the Horace Rackham Foundation as well as the Eli Lilly Foundation. I was recently appointed to serve on the editorial board of the Journal of Biological Chemistry.

5. In 1985-1986, I served on the NSF/USDA/DOE advisory panel to establish the Plant Science Centers Program.

6. The purpose of this statement is to present published evidence of the state of the skill in the art prior for certain specific techniques known prior to the filing of the application and which could be used by one skilled in the art combined with the novel devices and methods disclosed for the first time by the instant application.

7. The following references are directed to the state of the art in Single molecule fluorescence resonance energy transfer:

Börsch M, Diez M, Zimmermann B, Reuter R, Gräber P.
"Stepwise rotation of the gamma-subunit of EFoF1-ATP synthase observed by intramolecular single-molecule fluorescence resonance energy transfer."
FEBS Lett. 2002 Sep 11;527(1-3):147-52.
PMID:12220651

Börsch M, Turina P, Eggeling C, Fries JR, Seidel CA, Labahn A, Gräber P.
"Conformational changes of the H+-ATPase from Escherichia coli upon nucleotide binding detected by single molecule fluorescence."
FEBS Lett. 1998 Oct 23;437(3):251-4.

8. The following reference is directed to the state of the art in Dark-field Microscopy:

Yasuda et al., "Resolution of distinct rotational substeps by submillisecond kinetic analysis of F1 ATPase," Nature 410, 19 April 2001, 898-904.

9. The following references are directed to the state of the art in Single-molecule fluorescence lifetime anisotropy:

Häsler K, Engelbrecht S, Junge W. "Three-stepped rotation of subunits gamma and epsilon in single molecules of F-ATPase as revealed by polarized, confocal fluorometry."
FEBS Lett. 1998 Apr 24;426(3):301-4.

Bowen B, Woodbury N., "Single-molecule fluorescence lifetime and anisotropy measurements of the red fluorescent protein, DsRed, in solution."
Photochem Photobiol. 2003 Apr;77(4):362-9.

10. The following reference is directed to the state of the art in Atomic Force Microscopy

Ando T, Kodera N, Takai E, Maruyama D, Saito K, Toda A. 2001.
"A high-speed atomic force microscope for studying biological macromolecules." Proc. Natl. Acad. Sci. USA 98:12468–12472.

11. The following reference is directed to the state of the art in Surface Plasmon Resonance:

Jiří Homola, "Present and future of surface plasmon resonance biosensors," Anal Bioanal Chem (2003) 377 : 528–539, DOI 10.1007/s00216-003-2101-0

I declare that all statements made herein of my own knowledge are true and that all statements made on information and belief are believed to be true, and further that these statements were made with the knowledge that willful false statements and the like so made are punishable by fine or imprisonment, or both, under §1001 of Title 18 of the United States Code and that such willful false statements may jeopardize the validity of the application or any patent issuing thereon.

Date: 08-05-2011

Wayne D. Frasch, Ph.D.
Tempe, AZ

FEBS 26441 FEBS Letters 527 (2002) 147–152

Stepwise rotation of the γ-subunit of EF_0F_1-ATP synthase observed by intramolecular single-molecule fluorescence resonance energy transfer[1]

Michael Börsch[a,b,*], Manuel Diez[a], Boris Zimmermann[a], Rolf Reuter[a], Peter Gräber[a]

[a] *Institut für Physikalische Chemie, Albert-Ludwigs-Universität Freiburg, Albertstr. 23 a, 79104 Freiburg, Germany*
[b] *3. Physikalisches Institut, Universität Stuttgart, Pfaffenwaldring 57, 70550 Stuttgart, Germany*

Received 17 July 2002; accepted 1 August 2002

First published online 14 August 2002

Edited by Vladimir Skulachev

Abstract The EF_0F_1-ATP synthase mutants bQ64C and γT106C were labelled selectively with the fluorophores tetramethylrhodamine (TMR) at the b-subunit and with a cyanine (Cy5) at the γ-subunit. After reconstitution into liposomes, these double-labelled enzymes catalyzed ATP synthesis at a rate of 33 s^{-1}. Fluorescence of TMR and Cy5 was measured with a confocal set-up for single-molecule detection. Photon bursts were detected, when liposomes containing one enzyme traversed the confocal volume. Three states with different fluorescence resonance energy transfer (FRET) efficiencies were observed. In the presence of ATP, repeating sequences of those three FRET-states were identified, indicating stepwise rotation of the γ-subunit of EF_0F_1. **© 2002 Federation of European Biochemical Societies. Published by Elsevier Science B.V. All rights reserved.**

Key words: H^+-ATP synthase; EF_0F_1; Inter-subunit rotation; Single-molecule fluorescence resonance energy transfer

1. Introduction

Membrane-bound H^+-ATP synthases catalyze the formation of ATP from ADP and inorganic phosphate in mitochondria, chloroplasts and bacteria. Endergonic ATP synthesis is coupled to proton translocation across the membrane. The enzyme consists of two major parts. The hydrophobic membrane-integrated F_0 part is involved in proton transport across the membrane, whereas the hydrophilic F_1 part contains nucleotide and phosphate binding sites. In *Escherichia coli*, the F_1 part consists of five different subunits with the stoichiometry $\alpha_3\beta_3\gamma\delta\varepsilon$ and the F_0 part is built of three different subunits with a likely stoichiometry ab_2c_{10-14} [1]. The three catalytic nucleotide binding sites on the β-subunits undergo conformational changes [2,3], adopting in sequential order the 'open', 'tight' and 'loose' conformation during ATP-synthesis [4]. These changes are induced by 'docking–undocking' steps of the γ-subunit to the three different αβ-pairs, i.e. by a rotation of the γ-subunit (for reviews, see [4–6]).

ATP-induced rotation of the γ-subunit within the $\alpha_3\beta_3$ barrel has been deduced from ensemble measurements [7,8] and was convincingly visualized by a single-enzyme approach [9]. In these experiments, the $\alpha_3\beta_3\gamma$-fragment of the H^+-ATPase from *Bacillus* PS3 was attached with three His-tags onto the glass surface of a microscopic coverslip, and, as an indicator, a fluorescent μm-long actin filament was connected to the γ-subunit. The orientation of the actin filament with respect to the $\alpha_3\beta_3$ hexamer was monitored by videomicroscopy. At very low ATP concentrations, rotation occurred in discrete 120° steps consistent with sequential ATP hydrolysis at the three β-subunits [10]. Recently, substeps during ATP hydrolysis have been identified [11]. Rotation of the γ-subunit was shown by the fluorescent actin filament method with F_1 parts from chloroplasts and *E. coli* [6] and was used to demonstrate rotation of the ε-subunit and the c-ring in F_0F_1 [12,13]. According to these results, subunits $\gamma\varepsilon c_{10-14}$ ('rotor') rotate against subunits $\alpha_3\beta_3\delta ab_2$ ('stator') counter-clockwise during ATP hydrolysis, when viewed from the membrane to F_1. However, it was not possible to demonstrate with this method that proton transport is coupled with the movement of the rotor subunits.

To ensure coupling during ATP hydrolysis and to maintain full enzymatic activity for ATP synthesis, we incorporated the holoenzyme F_0F_1 into a lipid membrane and labelled specifically the γ-subunit and b-subunit with two different fluorophores chosen for efficient fluorescence resonance energy transfer (FRET). These indicator molecules were small enough to allow for an unconstrained subunit movement. Intramolecular subunit movement resulting in a change in the distances between the fluorophores were detected by changes in FRET efficiencies. After reconstitution of the labelled F_0F_1 into liposomes, ATP synthesis was observed by generating a pH difference and an additional electric potential difference across the membrane. Using confocal single-molecule fluorescence detection, we measured subunit movements during ATP hydrolysis by intramolecular FRET in fully functional single EF_0F_1 reconstituted in liposomes.

2. Materials and methods

The plasmid pRA114 carrying the γT106C mutation was constructed by Aggeler and Capaldi [14] and was expressed in strain RA1 [15]. EF_1 was isolated according to [16]. The γ-subunit of EF_1 was selectively labelled with carbocyanine dye Cy5®-maleimide in 50 mM MOPS/HCl (pH 7.0) as described previously [17,18]. Cy5-malei-

*Corresponding author. Fax: (49)-711-685 5281.
E-mail address: m.boersch@physik.uni-stuttgart.de (M. Börsch).

[1] This paper is dedicated to Prof. H.T. Witt on the occasion of his 80th birthday.

Abbreviations: FRET, fluorescence resonance energy transfer; AMPPNP, adenosine-5′-(β,γ-imido)triphosphate; Cy5, carbocyanine dye Cy5®; TMR, tetramethylrhodamine

0014-5793/02/$22.00 © 2002 Federation of European Biochemical Societies. Published by Elsevier Science B.V. All rights reserved.
PII: S0014-5793(02)03198-8

mide was kindly provided by E. Schweinberger and C.A.M. Seidel (MPI für Biophysikalische Chemie, Göttingen, Germany). EF_1 concentrations were determined by UV absorption using an extinction coefficient $\varepsilon = 191\,000\ M^{-1}\ cm^{-1}$ at 280 nm. For Cy5, an extinction coefficient of $250\,000\ M^{-1}\ cm^{-1}$ at 649 nm was used. Unbound dye was removed after 4 min by passing twice through Sephadex G50 centrifuge columns. Specificity of γ-subunit labelling was checked by fluorescence detection after SDS–PAGE. Approximately 65% of EF_1 was labelled with Cy5. EF_1-γT106C-Cy5 was stored at −80°.

In order to introduce a cysteine in the b-subunit, the new plasmid pRR76/bC21S/bQ64C was constructed from pRA100 [19] with pNOC/bC21S obtained from R. Fillingame [20]. The mutation bQ64C was introduced into pNOC by a two-stage PCR mutagenesis procedure [21] to yield pRR36. The fragment with the two mutations was ligated to pRA100. The resulting plasmid pRR76 was expressed in strain RA1 [15]. EF_0F_1 was isolated according to [22]. The b-subunits in this EF_0F_1 were labelled with tetramethylrhodamine (TMR)-maleimide (Molecular Probes) as described above. The degree of labelling was adjusted to approximately 20% to avoid labelling of both b-subunits at the same enzyme. EF_0F_1-bQ64C-TMR was reconstituted in liposomes [22] with a stoichiometry of one EF_0F_1 per liposome. The F_1 parts were removed [23] and the liposomes containing EF_0-bQ64C-TMR were reassembled with EF_1-γT106C-Cy5 to yield liposomes with the double-labelled enzyme EF_0-bQ64C-TMR-F_1-γT106C-Cy5 according to [24,25]. The efficiencies of removal of F_1 and reassembling with labelled F_1 were controlled by measuring ATP synthesis activities. The initial rate of ATP synthesis catalyzed by EF_0F_1 was measured after an acid–base transition at 23°C as described previously [22].

Single-molecule fluorescence measurements of EF_0F_1 in liposomes were performed with a confocal set-up of local design [25]. A frequency doubled Nd:YAG laser (532 nm, 50 mW, Coherent, Germany) was used for excitation. The laser beam was attenuated to 120 μW and focussed by a water immersion objective (UAPO 40×, N.A. 1.15, Olympus) into the buffer solution placed on a microscope slide. Fluorescence was measured in two spectral regions. Single photons were detected with avalanche photodiodes (SPCM-AQR-15, EG&G, Canada) after passing an interference filter HQ 575nm/65nm for TMR and a HQ 665nm LP for Cy5 (AHF, Germany). Photons in two channels were counted in parallel by a multichannel scaler (PMS 300, Becker & Hickl, Berlin, Germany). The actual confocal detection volume $V = 7.7$ fl was calculated from fluorescence correlation spectroscopy using rhodamine 6G according to [18]. All fluorescence measurements were performed in buffer A (50 mM HEPES/NaOH, 2.5 mM $MgCl_2$, 400 μM sodium ascorbate, pH 8.0). Fluorescent impurities of the buffer were removed by activated charcoal granula (Merck, Germany) with subsequent sterile filtration. ATP and adenosine-5′-(β,γ-imido)triphosphate (AMPPNP) were obtained from Böhringer (Mannheim, Germany). The concentration of proteoliposomes was adjusted such that only one liposome was detected in the confocal volume at any time.

3. Results

EF_0F_1 was labelled with two fluorophores. In order to observe inter-subunit movement in functionally intact EF_0F_1 by intramolecular FRET, it is necessary to label specifically one subunit of the 'stator' part and one of the 'rotor' part. For labelling of the b-subunit with the FRET donor TMR, a cysteine in the b-subunit at position 64 was introduced. For labelling of the γ-subunit with the FRET acceptor Cy5, we used the mutant EF_1-γT106C [14]. Selective labelling was achieved by the following procedure.

Step 1: Isolated EF_0F_1-bQ64C was labelled with TMR at a substoichiometric concentration. A ratio of 0.2 TMR per EF_0F_1 was chosen to avoid labelling of both b-subunits. EF_0F_1-bQ64C-TMR was reconstituted into liposomes with approximately one EF_0F_1 per liposome. The rate of ATP synthesis was measured after energization by $\Delta pH/\Delta\phi$ with a rate of 61 s^{-1}. This rate is comparable to that of wild-type EF_0F_1 [22]. Therefore, labelling of the b-subunit with TMR did not change ATP synthesis activity (see Table 1). Step 2: F_1 parts of this enzymes were removed and liposomes with incorporated EF_0-bQ64C-TMR were retained. EF_0-liposomes showed no ATP synthesis activity, neither with TMR-labelled EF_0 nor with unlabelled EF_0, indicating an efficient removal of the F_1 parts. Step 3: EF_1-γT106C was isolated and labelled with Cy5. Step 4: Finally, we incubated the EF_0-liposomes with the EF_1-γT106C-Cy5 (and in control experiments with unlabelled EF_1-γT106C). After removal of the non-assembled F_1 parts by ultracentrifugation, we obtained EF_0F_1 in liposomes, in which the b-subunit in the EF_0 part was specifically labelled with TMR and the γ-subunit in the F_1 part was specifically labelled with Cy5. The ATP synthesis rate of this double-labelled EF_0F_1 was 33 s^{-1}, which corresponds to 50% of the rate before removal of F_1. A similar result was obtained when unlabelled EF_1 was reassembled with EF_0. Addition of DCCD blocked almost completely ATP synthesis (Table 1).

Using double-labelled enzymes reconstituted in liposomes ('FRET-labelled EF_0F_1', EF_0-bQ64C-TMR-F_1-γT106C-Cy5), intramolecular FRET between TMR at the b-subunit and Cy5 at the γ-subunit was measured by a confocal set-up with two-channel detection. Photons were detected in the spectral range of 545–610 nm from TMR ('green channel') and at wave-

Table 1
Rates of ATP synthesis catalyzed by labelled EF_0F_1 in liposomes

Conditions	Rate (s^{-1})
b-mutant	
EF_0F_1-bQ64C	61 ± 3
b-mutant after removal of F_1	
EF_0-bQ64C	0
labelled b-mutant	
EF_0-bQ64C-TMR-F_1	61 ± 4
labelled b-mutant after removal of F_1	
EF_0-bQ64C-TMR	0
labelled b-mutant after removal of F_1 and reassembled with F_1	
EF_0-bQ64C-TMR-F_1	29 ± 4
b-mutant after removal of F_1 and reassembled with labelled F_1	
EF_0-bQ64C-F_1-γT106C-Cy5	32 ± 6
labelled b-mutant after removal of F_1 and reassembled with labelled F_1	
EF_0-bQ64C-TMR-F_1-γT106C-Cy5	33 ± 3
EF_0-bQ64C-TMR-F_1-γT106C-Cy5 in presence of 10μDCCD	4 ± 3

EF_0F_1 with mutations bQ64C and γT106C was reconstituted into liposomes and the rates of ATP synthesis were measured after energization by ΔpH and $\Delta\phi$. Given are the mean and standard deviations from six independent measurements.

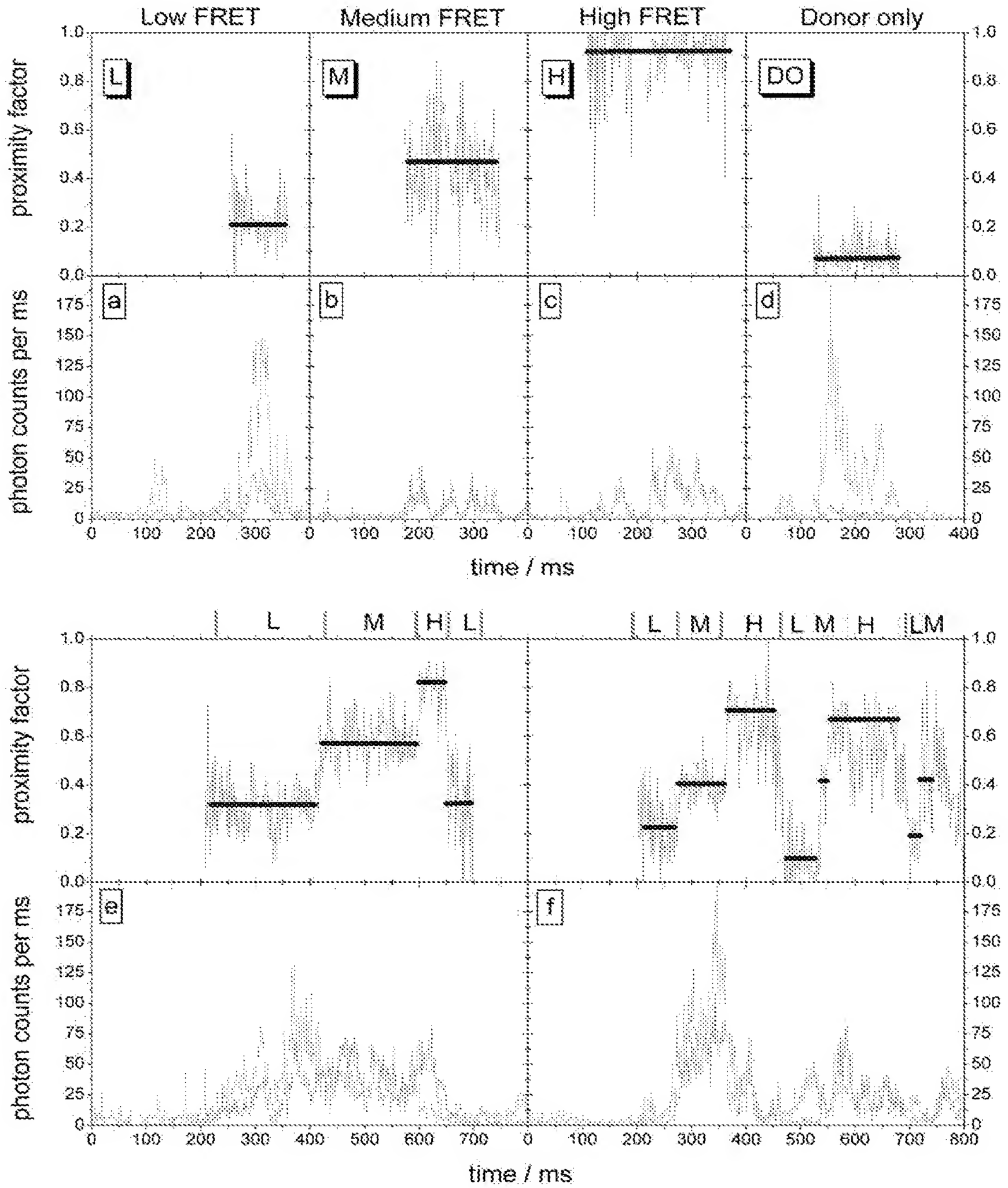

Fig. 1. Photon bursts and proximity factor traces of single FRET-labelled EF_0F_1 in liposomes. Single-molecule fluorescence of FRET-labelled EF_0F_1 reconstituted in liposomes is observed as photon bursts, when liposomes containing one FRET-labelled enzyme traverse the confocal detection volume. Green: time traces of TMR fluorescence intensities; red: simultaneous time trace of Cy5. The blue traces in the panels above are the calculated proximity factors. In the presence of AMPPNP, three states with different FRET efficiencies (a–c) are observed in which the proximity factor remains constant during the burst. d: Reconstituted EF_0-bQ64C-TMR-F_1 represent enzymes with FRET donor only. e,f: In the presence of ATP, fluctuations of the proximity factor corresponding to the three FRET states are detected within one burst. The sequence of states is indicated above the proximity factor trace.

lengths above 665 nm from Cy5 ('red channel'). The average background signal from buffer A containing 1 mM AMPPNP or 1 mM ATP was approximately 3 photons/ms in both channels. In the presence of FRET-labelled EF_0F_1-liposomes in solution, well-separated photon bursts with count rates up to 150 photons/ms were observed. This indicates a single liposome migrating through the detection volume. At the beginning of the time trace a in Fig. 1, both channels detect only background signal. At 255 ms, a liposome enters the detection volume and the TMR fluorescence intensity (green trace) increases to approximately 150 counts/ms. At 370 ms, the proteoliposome leaves the detection volume and and fluorescence decreases to background level. Simultaneously, an increase of Cy5 fluorescence with a count rate of 35 counts/ms is detected

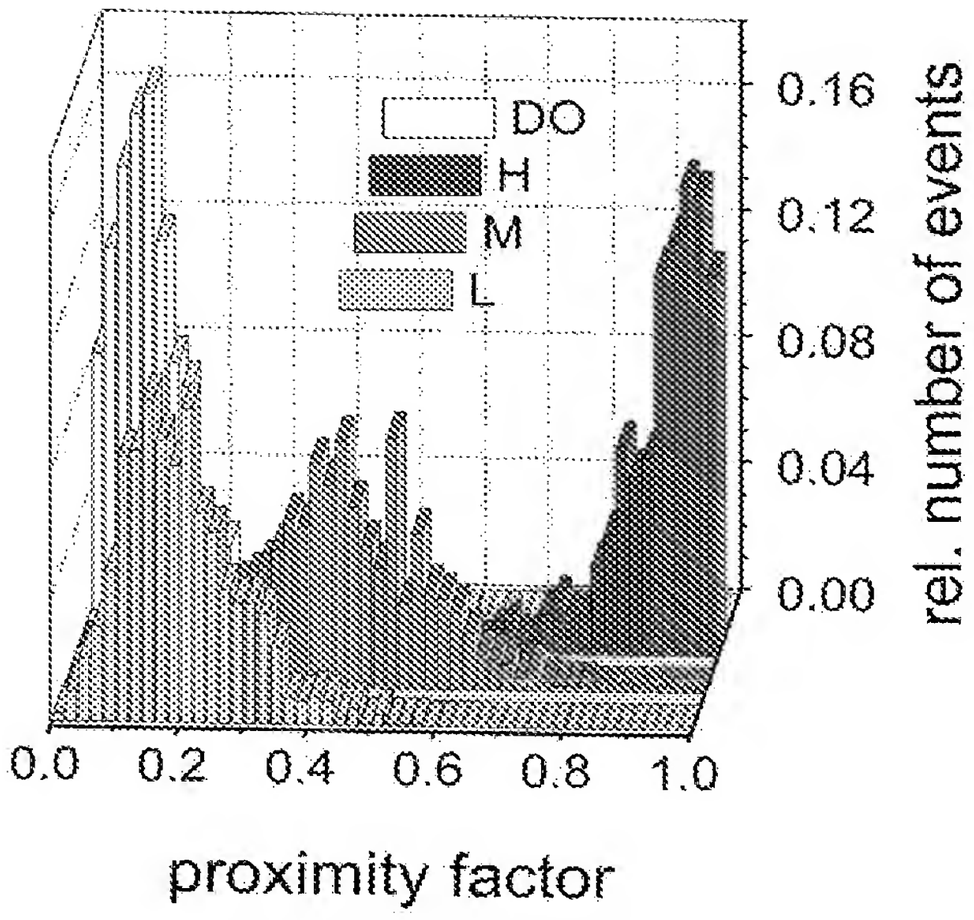

Fig. 2. Histogram of proximity factors from single FRET-labelled EF_0F_1 in the presence of 1 mM AMPPNP. L: low FRET efficiency state; M: medium FRET efficiency state; H: high FRET efficiency state; DO: 'donor only' state from TMR-labeled EF_0F_1 without FRET acceptor. The normalized distributions are calculated from 1 ms time intervals in 10 long-lasting photon bursts for each FRET state.

(red trace). Since Cy5 is not excited directly at the laser wavelength and power applied, this indicates inter-subunit FRET from TMR to Cy5.

There are two reasons for the fluctuations in fluorescence intensities. First, the proteoliposome moves through the focus driven by Brownian motion. Excitation power and fluorescence that is detected depend on the position of the enzyme within the confocal volume. Second, the efficiency of FRET changes with inter-subunit movement. FRET efficiency was calculated as the proximity factor P [26]. This factor is the ratio of the acceptor fluorescence intensity (I_A) divided by the sum of donor and acceptor intensities:

$$P = I_A/(I_D + I_A) \quad (1)$$

The blue trace in Fig. 1a shows the proximity factor for the event. Although there were large changes in the fluorescence intensities in both channels within the photon burst, the proximity factor remained nearly constant around $P = 0.2$. In the following, this state is called L ('low FRET state').

We calculated the proximity factors for different photon bursts and classified them into four FRET states: L ('low') with $P \approx 0.2$, M ('medium') with $P \approx 0.5$, H ('high') with $P \approx 0.8$ and DO ('donor only') with $P < 0.1$. Examples for the different states are shown in Fig. 1a–d. In FRET state M, fluorescence intensities of donor and acceptor are almost equal; in FRET state H, acceptor count rate is higher than donor count rate. In state DO, the acceptor fluorescence is near background. As a rare event, we also observed photobleaching of the acceptor fluorophore within the burst (data not shown) indicated by a spontaneous decrease of the acceptor count rate to background level and accompanied by a simultaneous rise of the donor count rate. Photobleaching of Cy5 resulted in state DO. The same fluorescence intensity ratio for the DO state with $P < 0.1$ was measured in control experiments using reconstituted EF_0-bQ64C-TMR-F_1, which contained only the donor fluorophore on the b-subunit. The DO state was observed in the FRET-labelled ATP synthase preparation, because only 65% of EF_1 contained Cy5 and, as a consequence, 35% of the reconstituted EF_0F_1 were lacking the acceptor label. Detection of some photons in the acceptor channel ('cross talk') is therefore due to the spectral properties of TMR. This cross talk leads to an 'apparent proximity factor' which does not reflect FRET. The states L, M, and H were attributed to different conformations of the H^+-ATP synthase. These are characterized according to the Förster theory of FRET [27] by different distances between the donor at the b-subunit and the acceptor at the γ-subunit. Therefore, FRET state L reflects a long distance, M a medium distance and H a short distance.

When single-enzyme fluorescence was measured in the presence of 1 mM ATP, well-separated photon bursts were observed. However, the time course within one burst was quite different. Fig. 1e,f show two examples during ATP hydrolysis. In contrast to the bursts in the presence of AMPPNP, there was a change in the green-to-red intensity ratio, which can be seen more clearly using the calculated proximity factor (blue trace). The proximity factors fluctuated within one photon burst. Three levels of the proximity factor could be distinguished (L, M and H), which were comparable in magnitude to the three different states observed in the presence of AMPPNP. During ATP hydrolysis, a definite order of proximity factor transitions was observed: from the low FRET (L) to the medium FRET (M) to the high FRET (H) and then again to the low FRET (L) state. In a few cases, we observed within this sequence L→M→H→L also 'backward steps' (see Fig. 1f, the high FRET state starting at 560 ms seems to oscillate between H and M states before reaching the L state at 700 ms) and in some photon bursts, the sequence

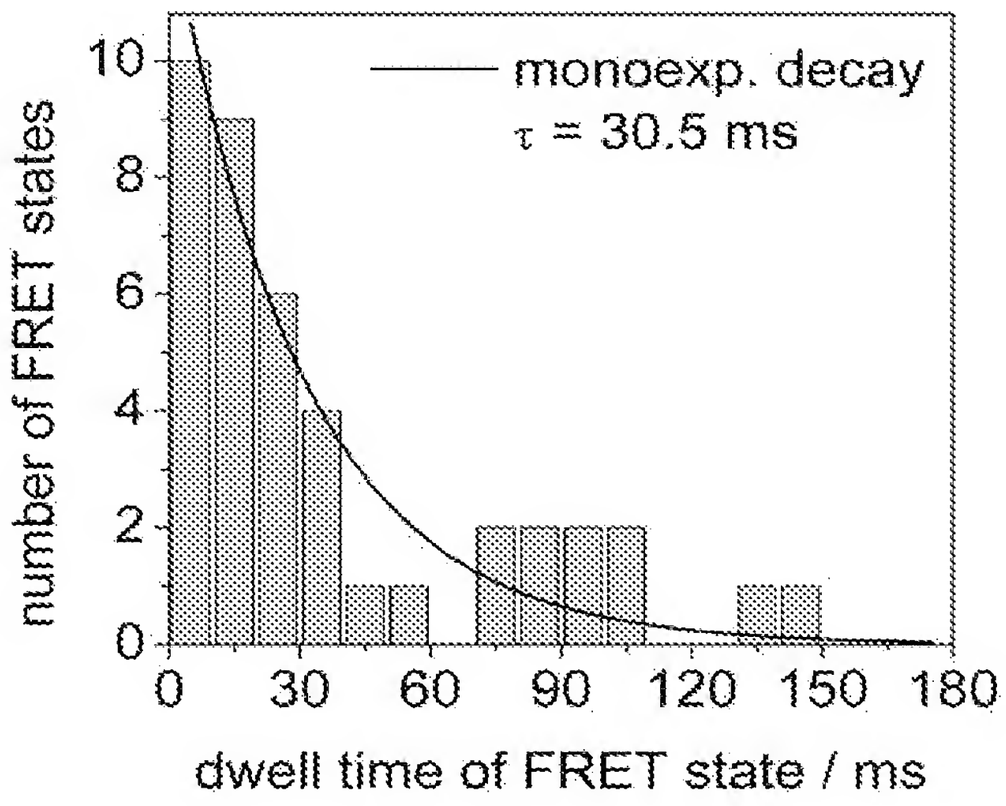

Fig. 3. Distribution of dwell times for the FRET states in presence of ATP. Dwell times of 40 FRET states were measured from photon bursts of FRET-labelled EF_0F_1 in liposomes, showing at least three distinct FRET states. First and last states of these bursts are omitted for the histogram, i.e. the states during entering and leaving the detection volume. The monoexponential decay fit yields a mean lifetime of 30 ms.

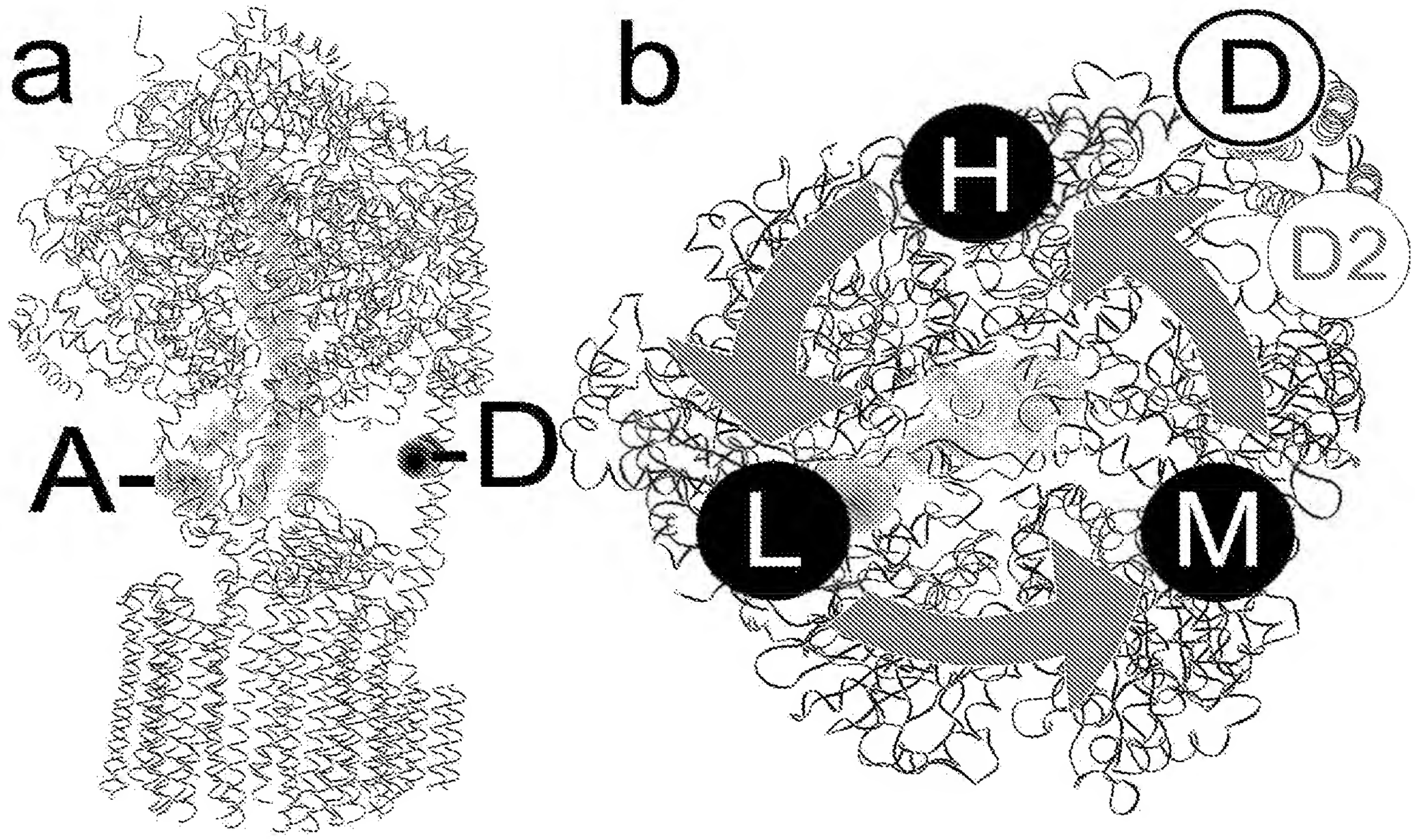

Fig. 4. Model of the FRET-label positions in EF_0F_1. Left: Side view of EF_0F_1. The homology model by S. Engelbrecht (http://131.173.26.96/se/se.html) was aligned with the structure of the γ- and ε-subunit [30]. Amino acid position of the FRET donor TMR at the b-subunit is indicated with 'D'; amino acid position of the FRET acceptor Cy5 at the γ-subunit is indicated with 'A'. Right: Cross section at the fluorophore level, viewed from the F_0 to the F_1 part. Position bQ64C is labelled 'D'; the distance between bQ64C and γT106C is labelled L (low FRET). Rotation of the γ-subunit by 120° steps results in two additional positions labelled M (medium FRET) and H (high FRET). The sequence $L \rightarrow M \rightarrow H \rightarrow L$ corresponds to counter-clockwise rotation of the γ-subunit during ATP hydrolysis.

was reversed ($L \rightarrow H \rightarrow M \rightarrow L$). In all cases the movements occurred stepwise within our experimental time resolution for defining a FRET state (approximately 5 ms).

To calculate a mean value for the proximity factor, we chose 10 photon bursts for each FRET state from the experiments with AMPPNP, in which the sum of donor and acceptor intensities was more than 20 counts/ms. The number of events as a function of the proximity factors is plotted in Fig. 2. The mean values of these distributions are $P = (0.18 \pm 0.1)$ for L, $P = (0.47 \pm 0.1)$ for M and $P = (0.8 \pm 0.1)$ for H. For DO, an apparent value of $P = (0.1 \pm 0.05)$ was obtained.

From the experiments during ATP hydrolysis, we selected 40 long-lasting photon bursts and measured the duration of the different FRET states. These dwell times were sorted into 10 ms intervals. The distribution (Fig. 3) was fitted by a monoexponential decay function which yielded a lifetime of 30 ms. This means that the average lifetime of the FRET states is 30 ms. If one ATP molecule is hydrolyzed during one FRET state, this corresponds to a rate of ATP hydrolysis of 33 s^{-1}, which agrees with the rate measured under comparable conditions in bulk experiments [28].

4. Discussion

H^+-ATP synthase from *E. coli* carrying TMR at position 64 of the b-subunit and Cy5 at position 106 of the γ-subunit catalyzed ATP synthesis, when the proteoliposomes were energized ($\Delta pH \approx 4$ plus $\Delta\phi$). Thus, the attachment of the two fluorophores did not disturb the conformational dynamics of the enzyme during proton transport-coupled ATP synthesis. By a single-molecule detection method, we measured the fluorescence of both fluorophores simultaneously, when liposomes containing one FRET labelled enzyme traversed the confocal volume. The intramolecular FRET efficiencies were determined by calculating proximity factor *P*. Three different FRET states characterized by proximity factors of around 0.2, 0.5, and 0.8 were observed, corresponding to three different distances of Cy5 at the γ-subunit relative to TMR at the b-subunit. In the presence of AMPPNP, these distances remained constant within the photon bursts, i.e. the enzymes were 'arrested' in one of the three different states. In the presence of ATP, the same three states were observed as characterized by their proximity factors. However, during ATP hydrolysis fluctuations between these three states occurred within one burst. The average lifetime of each FRET state was 30 ms. Since the time resolution is limited by the integration time of 1 ms used in these experiments, we are only able to estimate the upper limit for the transition time between the different states, which is less than 3 ms.

During ATP hydrolysis the distance between the fluorophores at the γ-subunit and the b-subunit remains constant within one conformational state, until a fast transition to the next state occurs. In this new state, the enzyme remains again for a time interval followed by a fast transition to the third

state. From this third state, the next transition leads to the first conformation again. Therefore, the distances between the γ-subunit and the b-subunit change in a cyclic manner. Based on the current knowledge of the structure of F_0F_1, we interpret these data in a molecular model (Fig. 4) which is based on homology modelling and alignment of structural information. This is shown in a side view in Fig. 4a and as a cross section at the fluorophore level (viewed from F_0 to the F_1 part). With b-subunits located at the interface of one αβ-pair, the distance between bQ64C and γT106C is 7.3 nm in the model. When we start at this position (L) and rotate the γ-subunit in steps of 120° counter-clockwise around an axis going through the center of F_1, the distances between bQ64C and γT106C are approximately 5 nm (M) and 2 nm (H). These distances closely match the values calculated from the proximity factors, if we assume $R_0 = 5.3$ nm [29] according to the Förster theory of FRET [27].

In some photon bursts, we observed a clockwise order of transitions. We attribute these events to enzymes in which the second b-subunit is labelled with TMR (position 'D2' in Fig. 4b). However, in most experiments, the sequence of FRET states was L → M → H → L. This implies that the sequence of states observed in the single-molecule FRET experiments is in accordance with a counter-clockwise rotation of the γ-subunit relative to the b-subunit during ATP hydrolysis. We conclude from this result that the γ-subunit rotates stepwise relative to the b-subunit in fully active EF_0F_1 in liposomes.

Acknowledgements: We thank C.A.M. Seidel and his group at the Max-Planck-Institut für Biophysikalische Chemie (Göttingen) for the supply of Cy5-maleimide and his help with the design of our confocal set-up for single-molecule detection, R.H. Fillingame for his help with the b-mutants and R.A. Capaldi and R. Aggeler for the gift of the γ-mutant.

References

[1] Weber, J. and Senior, A.E. (2002) Biochim. Biophys. Acta 1553, 188–211.
[2] Abrahams, J.P., Leslie, A.G., Lutter, R. and Walker, J.E. (1994) Nature 370, 621–628.
[3] Böckmann, R.A. and Grubmüller, H. (2002) Nat. Struct. Biol. 9, 198–202.
[4] Boyer, P.D. (1998) Biochim. Biophys. Acta 1365, 3–9.
[5] Capaldi, R.A. and Aggeler, R. (2002) Trends Biochem. Sci. 27, 154–160.
[6] Yoshida, M., Muneyuki, E. and Hisabori, T. (2001) Nat. Rev. Mol. Cell Biol. 2, 669–677.
[7] Duncan, T.M., Bulygin, V.V., Zhou, Y., Hutcheon, M.L. and Cross, R.L. (1995) Proc. Natl. Acad. Sci. USA 92, 10964–10968.
[8] Sabbert, D., Engelbrecht, S. and Junge, W. (1996) Nature 381, 623–625.
[9] Noji, H., Yasuda, R., Yoshida, M. and Kinosita, K.Jr. (1997) Nature 386, 299–302.
[10] Yasuda, R., Noji, H., Kinosita, K. and Yoshida, M. (1998) Cell 93, 1117–1124.
[11] Yasuda, R., Noji, H., Yoshida, M., Kinosita, K. and Itoh, H. (2001) Nature 410, 898–904.
[12] Sambongi, Y., Iko, Y., Tanabe, M., Omote, H., Iwamoto-Kihara, A., Ueda, I., Yanagida, T., Wada, Y. and Futai, M. (1999) Science 286, 1722–1724.
[13] Junge, W., Pänke, O., Cherepanov, D.A., Gumbiowski, K., Müller, M. and Engelbrecht, S. (2002) FEBS Lett. 504, 152–160.
[14] Aggeler, J.A. and Capaldi, R.A. (1992) J. Biol. Chem. 267, 21355–21359.
[15] Aggeler, R., Ogilvie, I. and Capaldi, R.A. (1997) J. Biol. Chem. 272, 19621–19624.
[16] Gogol, E.J., Luecken, U., Bork, T. and Capaldi, R.A. (1989) Biochemistry 28, 4709–4716.
[17] Turina, P. and Capaldi, R.A. (1994) J. Biol. Chem. 269, 13465–13471.
[18] Börsch, M., Turina, P., Eggeling, C., Fries, J.R., Seidel, C.A.M., Labahn, A. and Gräber, P. (1998) FEBS Lett. 437, 251–254.
[19] Aggeler, R., Chicas-Cruz, K., Cai, S.X., Keana, J.F.W. and Capaldi, R.A. (1995) J. Biol. Chem. 270, 9185–9191.
[20] Jones, P.C., Jiang, W. and Fillingame, R.H. (1998) J. Biol. Chem. 273, 17178–17185.
[21] Landt, O., Grunert, H.-P. and Hahn, U. (1990) Gene 96, 125–128.
[22] Fischer, S. and Gräber, P. (1999) FEBS Lett. 457, 327–332.
[23] Lötscher, H.R., deJong, C. and Capaldi, R.A. (1984) Biochemistry 23, 4128–4134.
[24] Perlin, D.S., Cox, D.N. and Senior, A.E. (1983) J. Biol. Chem. 258, 9793–9800.
[25] Börsch, M., Diez, M., Zimmermann, B., Reuter, R. and Gräber, P. (2002) in: Fluorescence Spectroscopy, Imaging and Probes – New Tools in Chemical, Physical and Life Sciences (Kraayenhof, R., Visser, A.J.W.G. and Gerritsen, H.C., Eds.), Springer Series on Fluorescence Methods and Applications, Vol. 2, pp. 197–207, Springer, Heidelberg.
[26] Deniz, A.A., Dahan, M., Grunwell, J.R., Ha, T., Faulhaber, A.E., Chemla, D.S., Weiss, S. and Schultz, P.G. (1999) Proc. Natl. Acad. Sci. USA 96, 3670–3675.
[27] Förster, Th. (1948) Ann. Phys. 2, 55–75.
[28] Fischer, S., Gräber, P. and Turina, P. (2000) J. Biol. Chem. 275, 30157–30162.
[29] Deniz, A.A., Laurence, T.A., Dahan, M., Chemla, D.S., Schultz, P.G. and Weiss, S. (2001) Ann. Rev. Phys. Chem. 52, 233–253.
[30] Rodgers, A. and Wilce, M. (2000) Nat. Struct. Biol. 7, 1051–1054.

FEBS 21006 FEBS Letters 437 (1998) 251–254

Conformational changes of the H^+-ATPase from *Escherichia coli* upon nucleotide binding detected by single molecule fluorescence

Michael Börsch[a,*], Paola Turina[b], Christian Eggeling[c], Joachim R. Fries[c], Claus A.M. Seidel[c], Andreas Labahn[a], Peter Gräber[a]

[a] *Institut für Physikalische Chemie, Universität Freiburg, Albertstr. 23a, D-79104 Freiburg, Germany*
[b] *Dipartimento di Biologia, Università degli Studi di Bologna, Via Irnerio 42, I-40126 Bologna, Italy*
[c] *MPI für Biophysikalische Chemie, Am Fassberg 11, D-37077 Göttingen, Germany*

Received 1 September 1998

Abstract Using a confocal fluorescence microscope with an avalanche photodiode as detector, we studied the fluorescence of the tetramethylrhodamine labeled F_1 part of the H^+-ATPase from *Escherichia coli*, EF_1, carrying the γT106-C mutation [Aggeler, J.A. and Capaldi, R.A. (1992) J. Biol. Chem. 267, 21355–21359] in aqueous solution upon excitation with a mode-locked argon ion laser at 528 nm. The diffusion of the labeled EF_1 through the confocal volume gives rise to photon bursts, which were analyzed with fluorescence correlation spectroscopy, resulting in a diffusion coefficient of 3.3×10^{-7} cm^2 s^{-1}. In the presence of nucleotides the diffusion coefficient increases by about 15%. This effect indicates a change of the shape and/or the volume of the enzyme upon binding of nucleotides, i.e. fluorescence correlation spectroscopy with single EF_1 molecules allows the detection of conformational changes.

1998 Federation of European Biochemical Societies.

Key words: H^+-ATPase; Conformational change; Fluorescence; Single molecule spectroscopy

1. Introduction

F_0F_1-ATP synthases occur in bacteria, mitochondria and chloroplasts [1]. These enzymes catalyze ATP synthesis coupled with a transmembrane proton flux. They have two large domains: a membrane integrated F_0 part, which is involved in proton transport, and a hydrophilic F_1 part, which contains the nucleotide binding sites. In *Escherichia coli*, the F_1 part contains five different subunits with the stoichiometry $\alpha_3\beta_3\gamma\delta\varepsilon$. Based on functional studies, it was suggested that the catalytic nucleotide binding sites on the β-subunits operate in a cyclic way, which is accomplished by subsequent 'docking-undocking' steps of the γ-subunit to the three αβ pairs. The nucleotide binding and dissociation steps at the F_1 part are coupled in the holoenzyme via long range conformational changes with proton binding, translocation and dissociation steps in the F_0 part (for review see [2]). In this work we investigated conformational changes of the F_1 part of the ATP synthase from *E. coli*, EF_1, which occur upon binding and dissociation of nucleotides. We labeled a cysteine in the γ-subunit of EF_1 with tetramethylrhodamine and measured the fluorescence of single molecules by confocal laser spectroscopy [3]. From an analysis of the fluorescence bursts using fluorescence correlation spectroscopy (FCS), the characteristic time of diffusion of the enzyme through the confocal volume can be derived. We found that the diffusion time changes upon nucleotide binding and conclude that this reflects structural changes in EF_1. A preliminary report of this work has been presented before [4].

*Corresponding author. Fax: (49) (761) 203-6189.
E-mail: boersch@ruf.uni-freiburg.de

Abbreviations: EF_1, hydrophilic F_1 part of the proton translocating H^+-ATPase from *Escherichia coli*; AMPPNP, β,γ-imidoadenosine-5′-triphosphate; TMRIA, tetramethylrhodamine-5-iodoacetamide; MOPS, 3-[*N*-morpholino] propanesulfonic acid; HEPES, *N*-[2-hydroxyethyl] piperazine *N*′-[2-ethanesulfonic acid]; TMR, tetramethylrhodamine; MCS, multichannel scaler; FCS, fluorescence correlation spectroscopy

2. Materials and methods

Strain pRA114/AN888, carrying the γT106-C mutation, is described in Aggeler and Capaldi [5] and was a gift from these authors. EF_1 was isolated from the mutant strain as described [6] except that the ion-exchange chromatography was performed on a HQ 20 FPLC column (PerSeptive). Isolated EF_1 was stored in liquid nitrogen until use.

The γ-subunit of EF_1 was selectively labeled with substoichiometric amounts of tetramethylrhodamine-5-iodoacetamide (TMRIA, Molecular Probes) in 50 mM MOPS/HCl (pH 7.0) with 10% glycerol as described [7]. EF_1 concentrations were determined by UV absorption using an extinction coefficient of 190 730 M^{-1} cm^{-1} at 280 nm as described [8]. Dye concentrations were determined using an extinction coefficient of 87 000 M^{-1} cm^{-1} at 543 nm. Unbound dye was removed after 4 min reaction time by passing twice through Sephadex G50 centrifuge columns. The labeling of the γ-subunit was specific as determined by the fluorescence of the gel after sodium dodecylsulfate polyacrylamide gel electrophoresis. The TMR labeled enzymes, TMR-EF_1, were stored at −80°C.

Fluorescence measurements were done in 50 mM HEPES/NaOH (pH 8.0) and 2.5 mM $MgCl_2$ (buffer B) after removing fluorescent impurities by activated charcoal granular (1.5 mm, Merck). TMR-EF_1 aliquots were diluted to final concentrations of 10^{-10} M. ATP and β,γ-imidoadenosine-5′-triphosphate (AMPPNP) stock solutions (10 mM) were prepared fresh in buffer B and were mixed with the diluted TMR-EF_1 solutions immediately before the fluorescence measurements. TMR-glutathione was prepared by mixing TMRIA with a 100-fold excess of the tripeptide glutathione (γ-Glu-Cys-Gly, Sigma) and diluted to a final dye concentration of 7×10^{-11} M for single molecule spectroscopy. Confocal fluorescence detection was performed with an active mode locked argon ion laser (excitation wavelength 528 nm, repetition rate 73 MHz) (Sabre, Coherent, Palo Alto, CA) using an epi-illuminated confocal fluorescence microscope (Fig. 1) similar to that described previously [9,10] with a beam-splitter at 530 nm, a 150 μm pinhole and a dichroic band-pass emission filter 582/50 nm (AF Analysentechnik, Tübingen, Germany). The expanded laser beam was attenuated to 530 μW and focused by a water immersion objective (UPLANAPO 60×, NA = 1.2, Olympus) to an excitation volume of a few femtoliters. The fluorescence signal was detected by a single photon counting avalanche photodiode (AQ 151, EG&G, Vaudreuil, Quebec, Canada). The multiplexed detector signal was registered in parallel by a multichannel scaler (MCS) using a PC-adapter counter (CIO-CTR05, Plug-in GmbH, Eichenau, Germany) and by a real-time correlator card (ALV-5000/E, ALV, Langen, Germany) for FCS. The laser focus and detection volume parameters (radial and axial $1/e^2$ radius $_0 = 0.65$ μm and $z_0 = 3.3$ μm, respectively) were determined from FCS measurements of rhodamine 6G

0014-5793/98/$19.00 © 1998 Federation of European Biochemical Societies. All rights reserved.
PII: S0014-5793(98)01247-2

in pure water with a characteristic diffusion time of $t_D = 0.38$ ms (see Table 1), assuming a translational diffusion coefficient of $D = 2.8 \times 10^{-6}$ cm^2 s^{-1} in water [11]. This corresponds to a detection volume of $V = {}^{1.5}{}_0{}^2 z_0 = 7.7$ fl and a focal area of $A = /2 {}_0{}^2 = 6.7 \times 10^{-9}$ cm^2 [12,13]. Thus, the excitation power of $P = 530$ μW is equivalent to a quasi-continuous focal irradiance of $I_0 = P/A = 8 \times 10^4$ W/cm^2 (see Fig. 1).

The samples were transferred to the microscope support by a microscope slide with a small depression and covered with a conventional cover glass. All measurements were performed at room temperature.

3. Results and discussion

Upon free diffusion in the solution, the TMR-labeled EF_1 enters the confocal detection volume, where the dye is excited by the pulsed laser light and due to the high laser repetition rate cycles continuously between the ground and excited states (see Fig. 1). Fluorescence photons are emitted as bursts when a single enzyme diffuses through the confocal volume. At the mean excitation irradiance of $I_0/2 = 4 \times 10^4$ W/cm^2, the mean number of photons emitted by a single TMR fluorophore in water is about 10^6 before photobleaching occurs [14]. Since the transit time of the labeled EF_1 is about 3 ms, the molecule can emit about 30 000 photons during this period [14]. Assuming a detection efficiency of about 3% [15], about 900 fluorescence photons should be detected from a single molecule transit. Furthermore, the arrangement of the avalanche photodiode with a 150 μm pinhole allows the selective detection

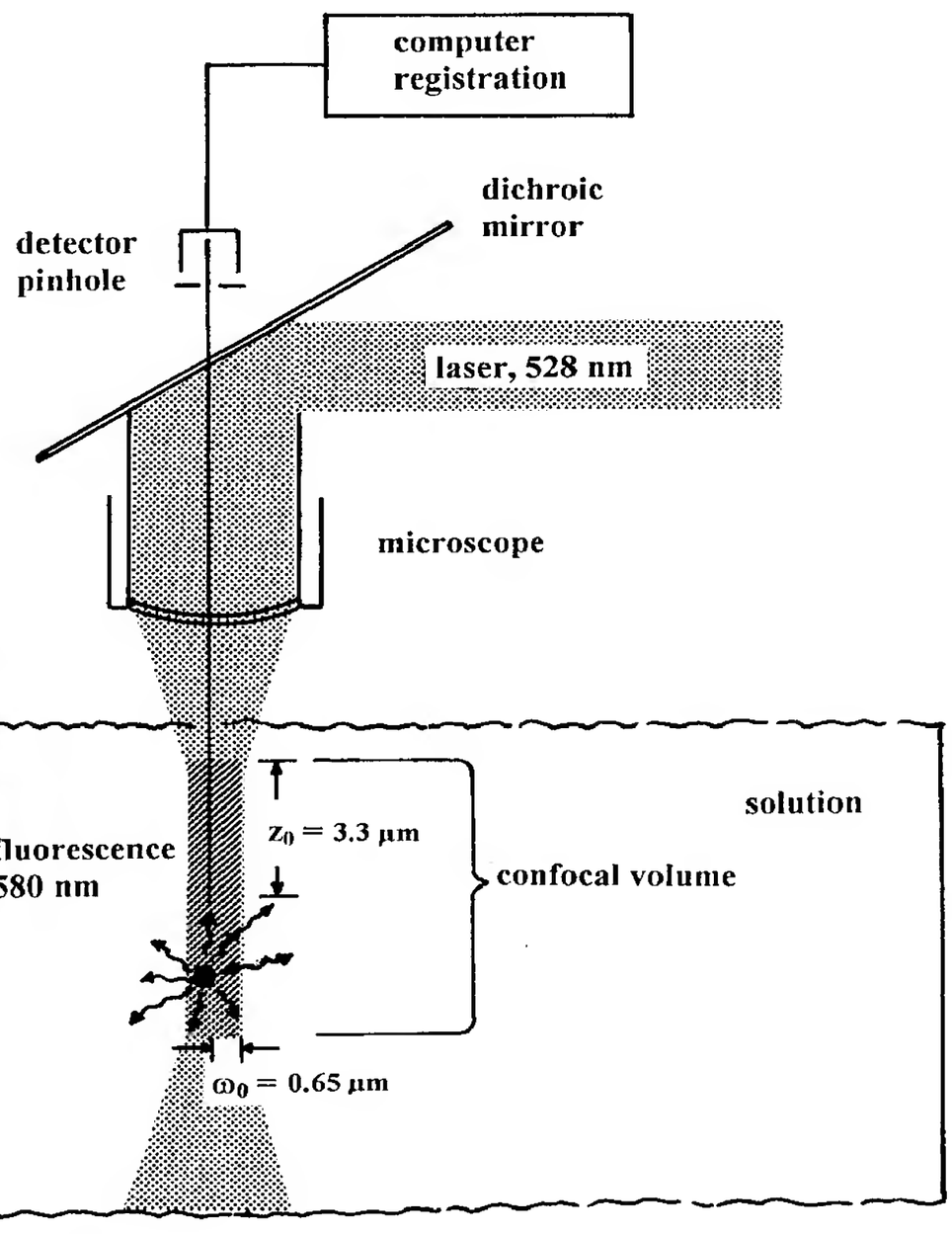

Fig. 1. Scheme of experimental setup for single molecule fluorescence detection. The pulsed laser beam (wavelength 528 nm) is focused through the microscope objective onto the sample. The fluorescence of the sample molecules entering the confocal detection volume is focused on a 150 μm pinhole and detected by a single photon counting avalanche photodiode.

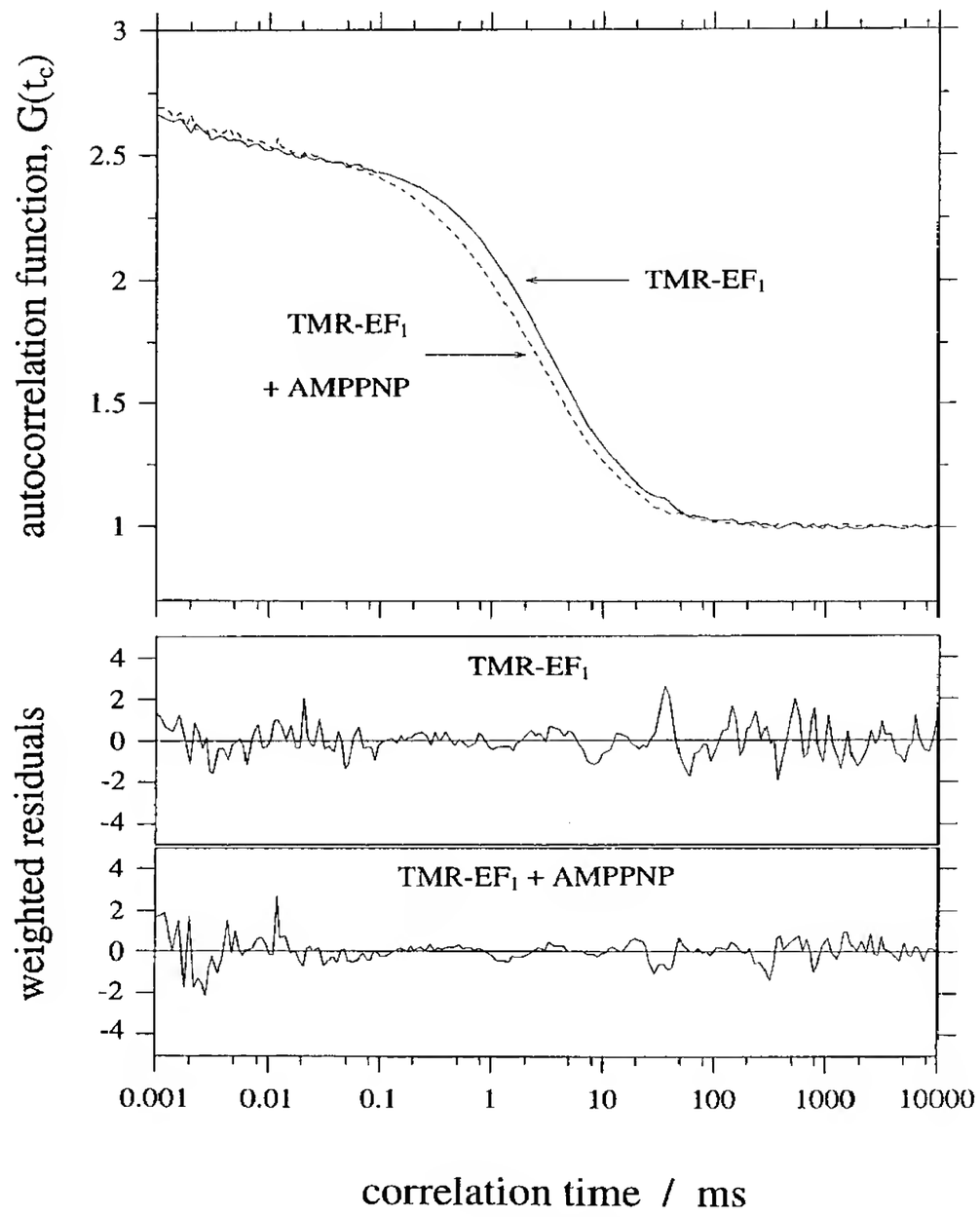

Fig. 2. Multichannel scaler trace of fluorescence signals from EF_1 labeled with tetramethylrhodamine. TMR-EF_1 was diluted in 50 mM HEPES/HCl (pH 8), 2.5 mM $MgCl_2$ to a concentration of 10^{-10} M. Data acquisition was performed at a speed of 1000 points per second (integration time 1 ms). The inset shows an expanded view of two fluorescence bursts.

of the fluorescence from the confocal volume with a strong suppression of background fluorescence from other parts of the solution (see Fig. 1).

Fig. 2 shows a MCS trace of TMR-EF_1 (10^{-10} M in buffer B) to monitor the fluorescence signals (bursts) arising from single TMR-EF_1 molecules diffusing through the confocal detection volume. The single bars of the MCS trace represent the number of fluorescence photons counted by the avalanche photodiode during an integration time of 1 ms. The trace shows burst rates of up to 220 kHz, while a background level of approximately 3 kHz is observed. This corresponds to a signal-to-noise ratio of 70. The background signal mainly results from scattered light and partially from background fluorescence of molecules outside the confocal detection volume. Due to the spatially dependent laser excitation irradiance and fluorescence collection efficiency of the open detection volume, the randomly diffusing molecules can either cross near the edges or traverse the center of the volume. Therefore, an inhomogeneous distribution of the number of detected fluorescence photons from a single molecule transit (burst size) is obtained [15]. This can be seen in Fig. 2, where events of different duration and with different count rates can be seen. The inset in Fig. 2 shows a magnification of a part of the MCS trace, showing a molecule diffusing through the center of the confocal detection volume (burst at 125 ms), and one diffusing through the edge (burst at 110 ms), where the excitation irradiance and, thus, the count rate is smaller.

Table 1
Results of the fluorescence correlation spectroscopy data analysis

Compound	t_T (μs)	T	t_D (ms)	t_A (ms)	A	N_F
Rhodamine 6G	2.1	0.13	0.38	none	none	5.10
TMR-glutathione	2.9	0.06	0.40	none	none	0.26
TMR-EF_1	5.7	0.10	3.2	0.16	0.03	0.60
TMR-EF_1+ATP	5.0	0.11	2.6	0.11	0.05	0.37
TMR-EF_1+AMPPNP	4.4	0.10	2.8	0.20	0.10	0.37

Parameters of a fit of the FCS data to Eq. 1: characteristic triplet correlation time, t_T; average fraction of molecules in the excited triplet state, T; characteristic time for translational diffusion, t_D; average number of fluorescing molecules in the confocal detection volume, N_F; characteristic correlation time of the 'dynamic quenched' state, t_A; and fraction of molecules in the 'dynamic quenched' state, A. The optical parameter ($_0/z_0$) was determined by fitting the FCS data of rhodamine 6G and fixed for all subsequent fits. All other parameters were allowed to vary freely. The estimated error for t_D is 7%.

FCS [12,13] was used to provide precise statistical data on the number of molecules in the detection volume and on the average diffusion time of the molecules through the detection volume. Analysis of the FCS data was performed with a least-squares fit algorithm using the following expression of the normalized autocorrelation function, $G(t_c)$, with the correlation time t_c.

$$G(t_c) = 1 + \frac{1}{N_F}\left(\frac{1}{1+t_c/t_D}\right)\left(\frac{1}{1+(\ _0/z_0)^2 t_c/t_D}\right)^{1/2}$$

$$\times(1-T+T\exp(-t_c/t_T)A + A\exp(-t_c/t_A)) \quad (1)$$

N_F is the average number of fluorescent molecules in the Gaussian detection volume with the $1/e^2$ radii, $_0$ and z_0, in radial and axial direction, respectively, $t_D = \ _0^2/4D$, the characteristic time for translational diffusion of the observed molecules with the diffusion coefficient, D, through the detection volume, A the average fraction of molecules within a so-called dynamic quenched state, t_A the characteristic correlation time of this quenched state and T the average fraction of molecules in the excited triplet state with a characteristic triplet correlation time, t_T [11].

Fig. 3 shows the measured autocorrelation curves of TMR-EF_1 in the absence of nucleotides and in the presence of AMPPNP together with the weighted residuals [16] of a fit of the data to Eq. 1, indicating a very precise description of the data by Eq. 1. The optical parameter ($_0/z_0$) was determined by fitting the rhodamine 6G FCS data and fixed for all subsequent fits. All other parameters were allowed to vary freely. The FCS data of pure rhodamine 6G and TMR-glutathione (data not shown) could be described properly by an autocorrelation function, $G(t_c)$, just using the diffusion and triplet terms of Eq. 1, i.e. the four parameters, N_F, t_D, T and t_T. In the case of TMR-EF_1 the addition of the so-called dynamic term, i.e. of the parameters A and t_A, is necessary. Obviously, this additional term, with parameters A and t_A, in Eq. 1 is only required for an optimal fit of the TMR-EF_1 data and, therefore, it reflects a property of the fluorophore in the protein environment. Table 1 shows the parameters of the proper fits of the FCS data from measurements of different samples to $G(t_c)$.

From the concentrations, c, of the different solutions and the size of the detection volume, $V = 7.7$ fl (see Section 2), an average number of molecules, $N = c \times V$, in this volume can be calculated: TMR-EF_1 solutions: $N = 0.5$, TMR-glutathione solution: $N = 0.32$, rhodamine 6G solution: $N = 4.6$. These estimations of N are in good agreement with the average

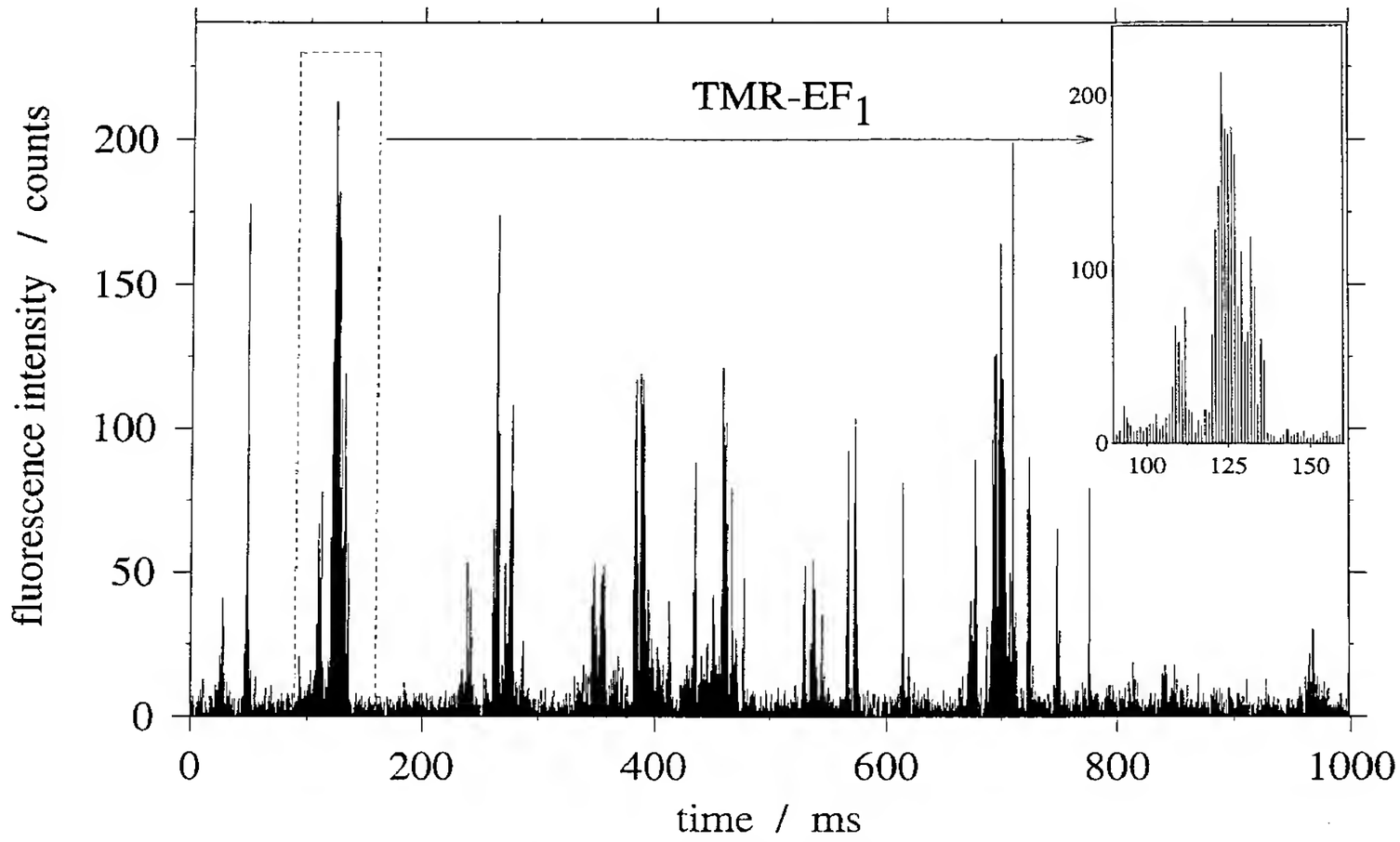

Fig. 3. Normalized fluorescence autocorrelation curves of TMR-EF_1. Solid line: TMR-EF_1 without added nucleotides. Dashed line: TMR-EF_1 in the presence of 1mM AMPPNP normalized to the curve without nucleotides. The weighted residuals [16] from the fit of the data to Eq. 1 are shown at the bottom. Fit parameters are summarized in Table 1.

number of fluorescent molecules, N_F, obtained from FCS (Table 1).

From Table 1 and Fig. 3 it becomes obvious that the addition of nucleotides (ATP or AMPPNP) to TMR-EF_1 results in a significant change of the characteristic diffusion time t_D. After addition of 1 mM ATP, t_D decreased by a factor of 0.81, while addition of 1 mM AMPPNP resulted in a decrease of t_D by a factor of 0.87. The same effects could also be observed in additional experiments where an enlarged confocal detection volume was employed. Using the relation $t_D = {}_0^2/4D$, between the known radial $1/e^2$ radius, ${}_0 = 0.65$ μm, and the characteristic translational diffusion time, t_D, the translational diffusion coefficient, D, of TMR-EF_1 can be calculated: D(TMR-EF_1) = 3.3×10^{-7} cm^2 s^{-1}, addition of 1 mM ATP: D(TMR-EF_1, ATP) = 4.1×10^{-7} cm^2 s^{-1}, and addition of 1 mM AMPPNP: D(TMR-EF_1, AMPPNP) = 3.8×10^{-7} cm^2 s^{-1}. It is obvious that the addition of the nucleotides increases the diffusion coefficient of TMR-EF_1, and that this effect is more enhanced with ATP.

The diffusion coefficient, D, is related to the frictional coefficient, f, via $D = kT/f$, where k is the Boltzmann constant and T the absolute temperature. At constant temperature and viscosity, the frictional coefficient, f, depends on the radius and the shape of the molecule [17]. We therefore conclude that binding of nucleotides (either ATP or AMPPNP) leads to a large conformational change in the F_1 part of the enzyme.

Similar large conformational changes in the F_1 part of H^+-ATPases were observed with completely different methods. Treatment of mitochondrial MF_1 with glycerol resulted in a release of the bound nucleotides and in a large decrease of the sedimentation coefficient, s, (from 11.9 S to 8.4 S) [18]. This large change was reversed when glycerol was removed.

Direct evidence for a large change of shape upon nucleotide binding comes from X-ray analysis. The X-ray structure of mitochondrial F_1 with the subunits $\alpha_3\beta_3\gamma\delta\varepsilon$ containing three AMPPNP, one ADP, and one ATP per enzyme has been determined [19]. Recently, the X-ray structure of the subcomplex $\alpha_3\beta_3$ from the bacillus PS 3 containing no bound nucleotides has been determined as well [20]. Although the molecular masses of the subunits α and β of PS 3 are similar to that of mitochondrial F_1 and the $\alpha_3\beta_3$ complex does not contain the γ-, δ-, and ε-subunits, it is much larger than the mitochondrial F_1. The main difference between the two structures seems to be that all three nucleotide binding pockets on the β-subunits are empty and in the open conformation in $\alpha_3\beta_3$, whereas in MF_1 only one β-subunit is in such a conformation. Presumably, the large difference between the two structures resulted at least partly from the different nucleotide occupancy of both enzymes. Supporting this conclusion, small-angle X-ray scattering data indicated a structural change of F_1 from PS 3 upon ADP binding which was modelled as a shrinkage of the six major subunits by 6% along their major axis [21].

Best fits to the FCS data of TMR labeled EF_1-ATPases were achieved only after introduction of a second bunching term (so-called dynamic quenched term). This term characterizes an equilibrium in the microsecond time range, which influences the fluorescence of the fluorophore. Most interestingly, addition of ATP or AMPPNP affected the 'dynamic' time, t_Λ, of TMR-EF_1 in opposite directions. With ATP the 'dynamic' time is shortened, indicating an acceleration of this process with respect to TMR-EF_1 without bound ATP. In contrast, with bound AMPPNP the 'dynamic' time is prolonged. Due to the small amplitudes of this effect, the quantification of these processes is currently difficult. However, it might be of special interest since AMPPNP binds tightly to the enzyme but, in contrast to ATP, is not hydrolyzed. Therefore, this 'dynamic' process might be associated with movements of the γ-subunit during catalysis.

The data in Table 1 show longer triplet correlation times and larger amplitudes of TMR-EF_1 compared to TMR-glutathione. This might be an indication that diffusion of oxygen to quench the triplet state of TMR is sterically hindered when the fluorophore is attached to the protein. These data indicate that single molecule fluorescence – either combined with polarized excitation and emission [22] or combined with fluorescence correlation spectroscopy analysis – can provide new information on conformational changes of the F_1 part upon nucleotide binding.

Acknowledgements: We thank Roderick A. Capaldi and Robert Aggeler for generous support and gift of the mutants making this work possible.

References

[1] Pedersen, P.C. and Carafoli, E. (1987) Trends Biochem. Sci. 12, 146–150.
[2] Boyer, P.D. (1997) Annu. Rev. Biochem. 66, 717–749.
[3] Keller, R.A., Ambrose, W.P., Goodwin, P.M., Jett, J.H., Martin, J.C. and Wu, M. (1996) Appl. Spectrosc. 50, 12A–32A.
[4] Börsch, M., Turina, P., Eggeling, C., Fries, J.R., Seidel, C.A.M., Labahn, A. and Gräber, P. (1998) Ital. Biochem. Soc. Trans. 11.
[5] Aggeler, J.A. and Capaldi, R.A. (1992) J. Biol. Chem. 267, 21355–21359.
[6] Gogol, E.J., Luecken, U., Bork, T. and Capaldi, R.A. (1989) Biochemistry 28, 4709–4716.
[7] Turina, P. and Capaldi, R.A. (1994) J. Biol. Chem. 269, 13465–13471.
[8] Gill, S.C. and von Hippel, P.H. (1989) Anal. Biochem. 182, 319–326.
[9] Zander, C., Sauer, M., Drexhage, K.H., Ko, D.-S., Schulz, A., Wolfrum, J., Brand, L., Eggeling, C. and Seidel, C.A.M. (1996) Appl. Phys. B 63, 517–523.
[10] Brand, L., Eggeling, C., Zander, C., Drexhage, K.H. and Seidel, C.A.M. (1997) J. Phys. Chem. A. 101, 4313–4321.
[11] Widengren, J., Mets, Ü. and Rigler, R. (1995) J. Phys. Chem. 99, 13368–13379.
[12] Elson, E.L. and Magde, D. (1974) Biopolymers 13, 1–27.
[13] Thompson, N.L. (1991) in: Topics in Fluorescence Spectroscopy, Volume 1: Techniques (Lakowicz, J.R., Ed.), pp. 337–378, Plenum Press, New York.
[14] Eggeling, C., Widengren, J., Rigler, R. and Seidel, C.A.M. (1998) Anal. Chem. 70, 2651–2659.
[15] Fries, J.R., Brand, L., Eggeling, C., Köllner, M. and Seidel, C.A.M. (1998) J. Phys. Chem. A (in press).
[16] Koppel, D.E. (1974) Phys. Rev. A 10, 1938–1946.
[17] Tanford, C. (1961) Physical Chemistry of Macromolecules, Wiley, Chichester.
[18] Garret, N.E. and Penefsky, H.S. (1975) J. Supramol. Struct. 3, 469–478.
[19] Abrahams, J.P., Leslie, A.G.W., Lutter, R. and Walker, J.E. (1994) Nature 370, 621–628.
[20] Shirakihara, Y., Leslie, A.G.W., Abrahams, J.P., Walker, J.E., Ueda, T., Sekimoto, Y., Kambara, M., Saika, K., Kagawa, Y. and Yoshida, M. (1997) Structure 5, 825–836.
[21] Furuno, T., Ikegami, A., Kihara, H., Yoshida, M. and Kagawa, Y. (1983) J. Mol. Biol. 170, 137–153.
[22] Häsler, K., Engelbrecht, S. and Junge, W. (1998) FEBS Lett. 426, 301–304.

Resolution of distinct rotational substeps by submillisecond kinetic analysis of F_1-ATPase

Ryohei Yasuda*†‖, Hiroyuki Noji*, Masasuke Yoshida‡*, Kazuhiko Kinosita Jr†* & Hiroyasu Itoh§*

** CREST 'Genetic Programming' Team 13, Teikyo University Biotechnology Center 3F, Nogawa 907, Miyamae-Ku, Kawasaki 216-0001, Japan*
† Department of Physics, Faculty of Science and Technology, Keio University, Yokohama 223-8522, Japan
‡ Chemical Resources Laboratory, Tokyo Institute of Technology, Yokohama 226-8503, Japan
§ Tsukuba Research Laboratory, Hamamatsu Photonics KK, Tokodai, Tsukuba 300-2635, Japan

The enzyme F_1-ATPase has been shown to be a rotary motor in which the central γ-subunit rotates inside the cylinder made of $\alpha_3\beta_3$ subunits. At low ATP concentrations, the motor rotates in discrete 120° steps, consistent with sequential ATP hydrolysis on the three β-subunits. The mechanism of stepping is unknown. Here we show by high-speed imaging that the 120° step consists of roughly 90° and 30° substeps, each taking only a fraction of a millisecond. ATP binding drives the 90° substep, and the 30° substep is probably driven by release of a hydrolysis product. The two substeps are separated by two reactions of about 1 ms, which together occupy most of the ATP hydrolysis cycle. This scheme probably applies to rotation at full speed (~130 revolutions per second at saturating ATP) down to occasional stepping at nanomolar ATP concentrations, and supports the binding-change model for ATP synthesis by reverse rotation of F_1-ATPase.

The ATP synthase is an enzyme ubiquitous in bacteria, plants and animals, which synthesizes ATP from ADP and inorganic phosphate using proton flow through a membrane[1–3]. F_1, a water-soluble portion of the ATP synthase, is the site of ATP synthesis, whereas protons flow through the membrane-embedded F_o portion. At least *in vitro*, F_1 can hydrolyse ATP to pump protons through the F_o portion in the reverse direction. Isolated F_1 only hydrolyses ATP, and is called F_1-ATPase. Its subunit composition is $\alpha_3\beta_3\gamma\delta\epsilon$.

The prevailing view is that ATP hydrolysis/synthesis in F_1 is coupled to proton flow in F_o through the rotation of a common shaft, of which the γ-subunit of F_1 is a part. This rotational coupling mechanism was initially proposed by Boyer[1–3], and by others[4–6]. Later, a crystal structure of F_1 showed that a rod-shaped γ-subunit is surrounded by a cylinder made of three α- and three β-subunits, arranged alternately[7] (Fig. 1a). An analogue of ATP, ADP and none were bound to the three β-subunits, indicating that sequential ATP hydrolysis on the three β-subunits would indeed induce rotation of the central, asymmetrical γ-subunit. Rotation of the γ-subunit in an isolated F_1 during ATP hydrolysis has been demonstrated experimentally by various methods[8–10].

We have visualized the rotation of the γ-subunit under an optical microscope by fixing F_1 on a surface and attaching an actin filament to the γ-subunit as a marker of its orientation[10]. At nanomolar ATP, the actin filament rotated in discrete 120° steps[11], consistent with the pseudo-three-fold symmetrical structure[7] of F_1. The rotation rate was close to one-third of the rate of ATP hydrolysis in solution, suggesting that one ATP molecule is consumed per 120° step[11]. At high ATP concentrations, however, the actin rotation was smooth rather than stepwise, and the rotation was much slower than ATP hydrolysis. Viscous friction imposed on the actin filament prevented fast rotation of F_1 and obscured the stepping behaviour. Here we have used a smaller marker, a colloidal gold bead of 40-nm diameter, for which the viscous friction is 10^{-3} to 10^{-4} times that for actin (Fig. 1b). In the resultant high-speed rotation, we were able to resolve substeps. In this study we investigate the magnitudes, speeds, and timings of the substeps, and we also look at: (1) the motor speeds at no load; (2) whether the motor uses different rotary mechanisms at low and high speeds; (3) which parts of hydrolysis reactions drive the substeps; and (4) what structural changes may underlie the substeps.

Full-speed rotation with 40-nm beads

Bead rotation was imaged by laser dark-field microscopy[12] (Fig. 1c),

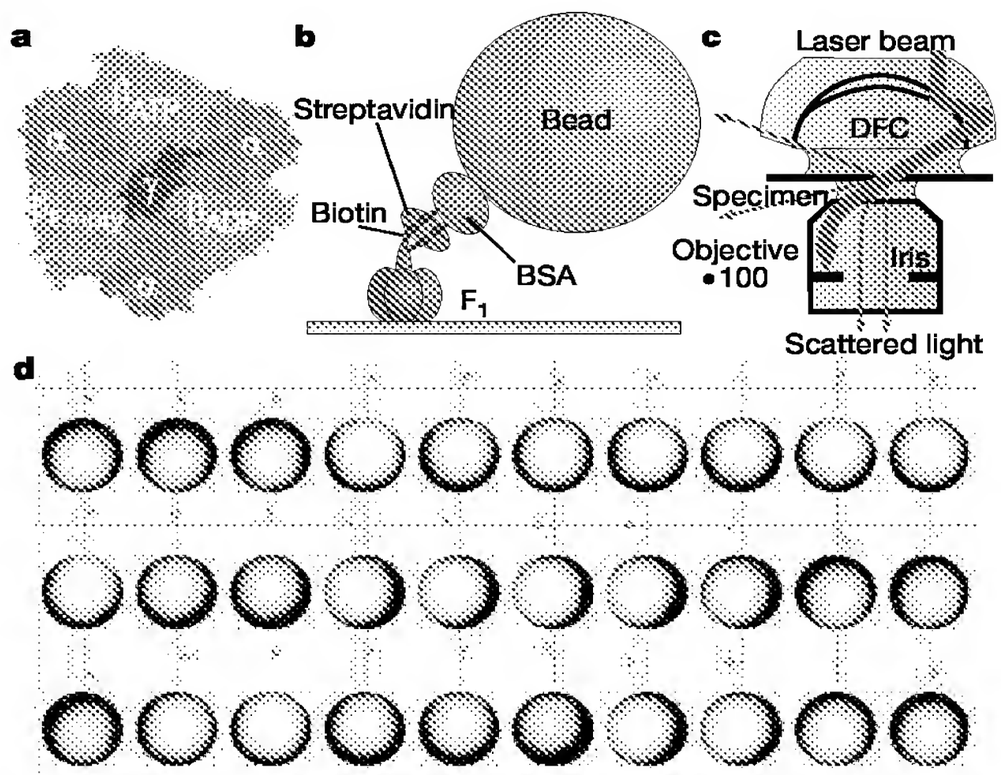

Figure 1 Observation of F_1 rotation. **a**, Atomic structure[7] of F_1-ATPase viewed from the F_o side (top in **b**). **b**, Side view of the observation system. The 40-nm bead gave a large enough optical signal that warranted a submillisecond resolution; but the bead was small enough not to impede the rotation. **c**, Laser dark-field microscopy for observation of gold beads. Only light scattered by the beads exited the objective and was detected. DFC, dark-field condenser. **d**, Sequential images of a rotating bead at 2 mM ATP. Images are trimmed in circles (diameter 370 nm) to aid identification of the bead position; centroid positions are shown above the images at ×3 magnification. The interval between images is 0.5 ms.

‖ Present address: Cold Spring Harbor Laboratory, 1 Bungtown Road, Cold Spring Harbor, New York 11724, USA.

© 2001 Macmillan Magazines Ltd

and recorded on a fast-framing charge-coupled-device (CCD) camera at speeds up to 8,000 frames per s. The 40-nm bead appeared as a spot of diffraction-limited size (~300 nm; Fig. 1d). When a bead is attached obliquely (Fig. 1b), rotation of the γ-subunit will result in a circular movement of the bead image. Some beads showed rotation (Fig. 1d; movies in Supplementary Information), and motions of these beads were analysed by calculating the centroid of the bead image[13]. The rotation diameter of bead centroid ranged between 25–55 nm. Diameters up to ~60 nm are possible for the height of F_1 of ~10 nm and the linker lengths of ~5 nm for streptavidin[14] and ~10 nm for BSA[15] (Fig. 1b). Rotation was stepwise at all ATP concentrations examined (see below).

To see whether the friction on the 40-nm bead impeded F_1 rotation, we varied the frictional load by attaching single or duplex polystyrene beads (108, 196 or 291 nm) to the γ-subunit. At both 2 mM and 2 μM ATP (Fig. 2; red and blue circles, respectively), time-averaged rotation rates showed saturation behaviour at small friction. Maximal rotation rate depended on ATP concentration [ATP], but increasing [ATP] beyond 2 mM did not accelerate rotation (see below). Thus, at 2 mM ATP, the 40-nm bead rotated at the full speed of the F_1 motor, which was 134 revolutions per second (r.p.s.) at 23 °C; the bead was not an impeding load for F_1. At saturating speeds, all beads rotated stepwise. On the load-dependent portions in Fig. 2, however, bead rotation was smooth, as was rotation of actin at these ATP concentrations[11]. The load dependence of actin rotation[11] (Fig. 2; triangles) is consistent with the bead assay.

One rotary mechanism at all speeds

The time-averaged rate of rotation showed simple Michaelis–Menten dependence on [ATP] (Fig. 3; the maximal rate at infinite [ATP], V_{max} = 129 r.p.s.; Michaelis constant, K_m = 15 μM), suggesting that one mechanism accounts for rotation in the nM–mM range. This idea is corroborated by observations[11,16,17] that the torque and its angle dependence, as well as mechanical work done in a 120° step, are independent of [ATP] over the nM–mM range. Also, the apparent rate of ATP binding, k_{on}^{ATP}, given by $3V_{max}/K_m$ of $(2.6 \pm 0.5) \times 10^7\ M^{-1}\ s^{-1}$ agrees with previous estimates based on the analysis of step intervals at nanomolar ATP[11,18].

As seen in Fig. 3, the rotation rate was close to one-third of the rate of ATP hydrolysis for bead-free F_1 in solution, supporting the contention that one ATP molecule is consumed per 120° rotation[11,16–18]. The hydrolysis rate, however, was lower, particularly around 50 μM. A probable cause is MgADP inhibition: F_1 is stochastically inactivated during ATP hydrolysis, when it binds MgADP tightly[17,19,20]. Although we started with nucleotide-free F_1, some inactivation may have proceeded during the mixing time of ~2 s. Indeed, the rate of inactivation increases with [ATP] and reaches ~0.3 s^{-1} at > 10 μM ATP[20], the position of the concavity in Fig. 3. Higher activity at still higher [ATP] is accounted for by binding of ATP to non-catalytic α-subunits, which tends to restore the hydrolysis activity[19]. Lauryldodecylamine oxide (LDAO), a suppressor of the MgADP inhibition[19], produced hydrolysis kinetics parallel to the rotation kinetics, although $V_{max}/3$ (82 s^{-1}) was only ~60% of V_{max} for rotation (Fig. 3).

The 120° step consists of 90° and 30° substeps

At 8,000 frames per s, steps were clearly resolved in the rotation of 40-nm beads, even at saturating ATP. At 2 mM ATP, only 120° steps were seen (Fig. 4a, b), whereas at 20 μM or 2 μM ATP, the 120° step was further split into roughly 90° and 30° substeps (Fig. 4c–f, where each panel shows a continuous record). We call the interval between a 30° substep and a 90° substep a '0° dwell' and the interval between 90° and 30° substeps a '90° dwell'. In Fig. 4c–f, 0° dwells fall on black horizontal lines that are separated from each other by 120°, and 90° dwells fall on grey lines that are 30° below the black lines. The 90° dwells were about a few ms in duration, on average, both at 2 and 20 μM ATP, whereas 0° dwells became longer at 2 μM. The implication is that F_1 waits for the arrival of ATP during the 0° dwell, which is terminated by a 90° substep induced by ATP binding. The subsequent 90° dwell is for a process or processes independent of [ATP]. This scheme predicts that, at [ATP] ~ K_m = 15 μM, 0° and 90° dwells have approximately equal lengths, as was observed

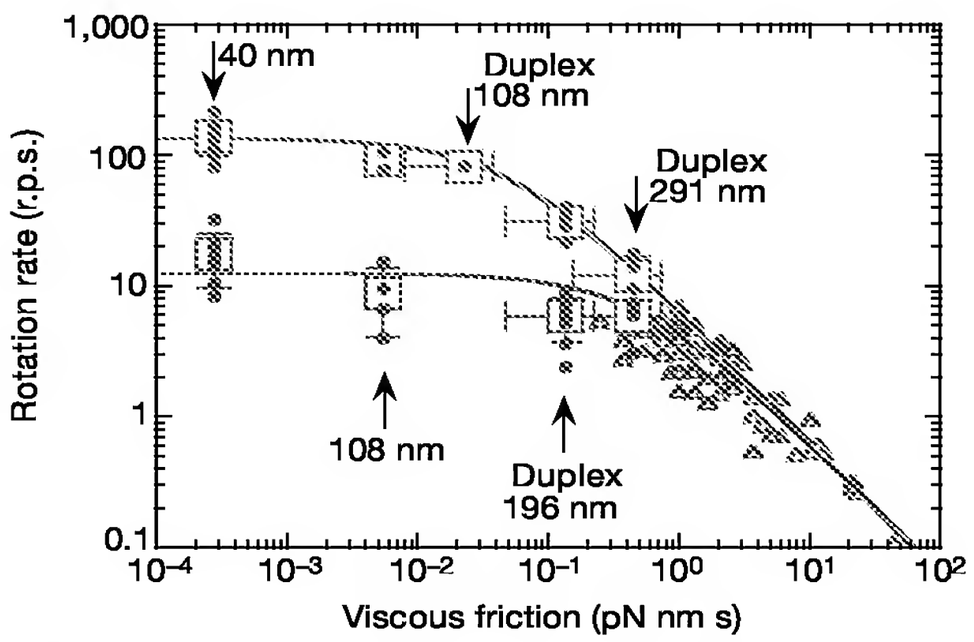

Figure 2 Relationship between rate of bead rotation and viscous friction on the bead. Circles, the average rate for a bead calculated over at least 20 consecutive revolutions; squares, the average over different beads (vertical error bars indicate s.d.). ATP at 2 mM and 2 μM is indicated by red and blue colours, respectively. The abscissa is the rotational frictional drag coefficient ξ calculated as in Methods. Possible range of ξ for each bead is shown by the size of the squares or associated horizontal error bars. For comparison, rotation rates for an actin filament attached to the γ-subunit[11] are also plotted (triangles). Lines show fits with the rate expected for a motor producing a constant torque[11]: $(1/V_{noload} + 2\pi\xi/N)^{-1}$ where N = 40 pN nm (assumed torque) and V_{noload} = 12.5 ± 1.0 r.p.s. for 2 μM ATP and 134 ± 3 r.p.s. for 2 mM ATP (s.e.m.).

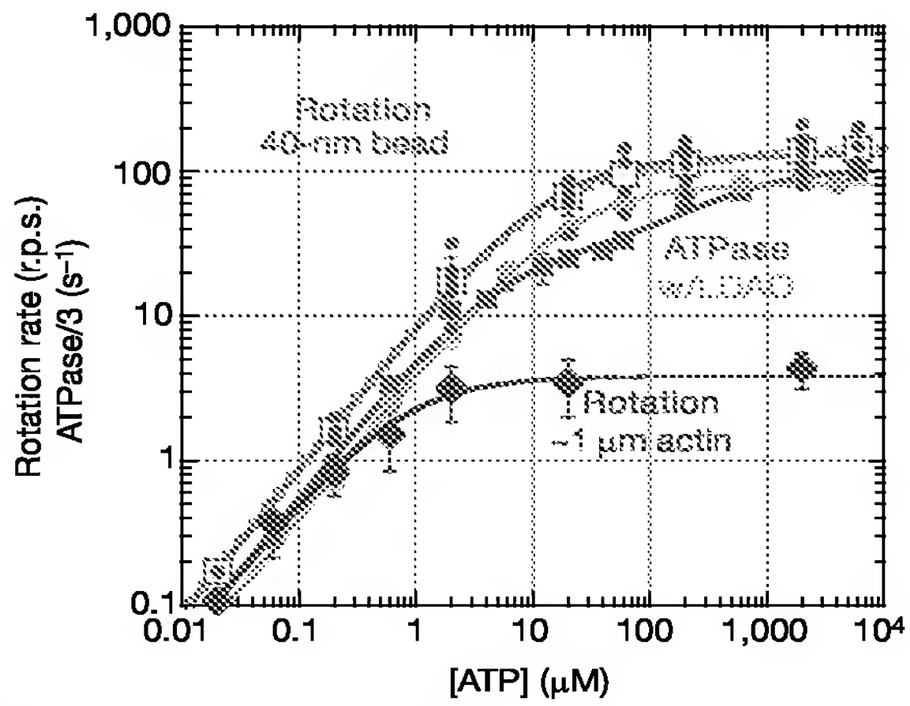

Figure 3 Comparison of rotation and hydrolysis rates. Red circles, time-averaged rotation rate for individual 40-nm beads. Red squares, rotation rate averaged over different beads. Dark green squares, one-third of the initial rate of ATP hydrolysis. Light green circles, one-third of the rate of ATP hydrolysis in the presence of LDAO. Blue diamonds, rotation rate for an actin filament attached to the γ-subunit[11]. Standard deviations greater than the symbol size are shown in bars ($n \geq 2$). Curves show fits with Michaelis–Menten kinetics, $V = V_{max}[ATP]/(K_m + [ATP])$, where V_{max} and K_m are 129 ± 9 r.p.s. and 15 ± 2 μM for bead rotation (red), 4.0 ± 0.3 r.p.s. and 0.7 ± 0.1 μM for actin rotation (blue), and 247 ± 9 s^{-1} and 19 ± 1 μM for hydrolysis in the presence of LDAO (light green). Fits with two K_m values, $V = (V_{max1}K_{m2}[ATP] + V_{max2}[ATP]^2)/([ATP]^2 + K_{m2}[ATP] + K_{m1}K_{m2})$, are also shown, where V_{max1} = 85 ± 9 s^{-1}, K_{m1} = 5.2 ± 0.7 μM, V_{max2} = 306 ± 22 s^{-1}, and K_{m2} = 393 ± 147 μM for hydrolysis without LDAO (dark green), and V_{max1} = 109 ± 30 r.p.s., K_{m1} = 12 ± 4 μM, V_{max2} = 149 ± 32 r.p.s., and K_{m2} = 682 ± 2768 μM for bead rotation (dashed pink). The latter does not show improvement over the simple fit in red. Values are means ± s.e.m.

© 2001 Macmillan Magazines Ltd

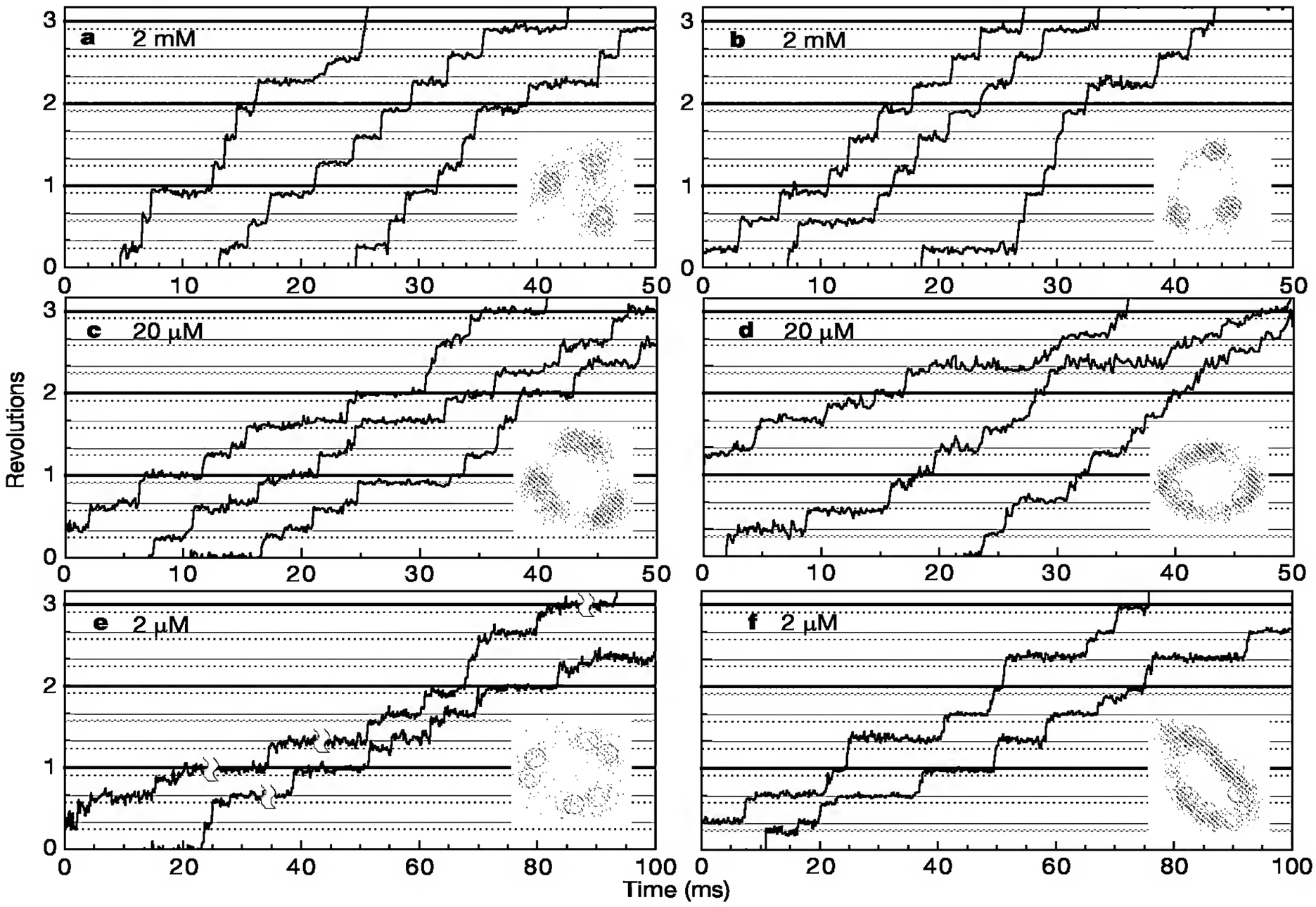

Figure 4 Unfiltered time courses of stepping rotation of 40-nm beads at varying [ATP]. **a**, **b**, 2 mM; **c**, **d**, 20 μM; **e**, **f**, 2 μM [ATP]. All curves in a panel are continuous; later curves are shifted, to save space. Grey horizontal lines are placed 30° below black lines. In **e**, some of the long dwells are cut short. Insets, positions of a bead within 0.25–0.5 ms before (red) and after (green) the main (90° or 120°) steps; runs lasting 0.5 s (2 mM) or 2 s (2 μM and 20 μM) were analysed. Circles indicate projection of ~0° and ~90° dwell points on an obliquely situated circular trajectory that best fit the data. Angles in the time courses and in Fig. 5 are those on the oblique circle.

at 20 μM ATP. At 2 mM ATP, the expected rate of ATP binding is $(2.6\times10^7\ M^{-1}s^{-1}\times2\ mM) \approx 5\times10^4\ s^{-1}$. Then, 0° dwells will be ~0.02 ms and will not be detected at the current resolution. The absence of substeps in Fig. 4a, b is thus explained. We place dwells in Fig. 4a, b on grey lines, because they must be 90° dwells according to this explanation (see also Fig. 7).

The 30° substeps were not always clear, but we could easily locate, in rotation records, steps that spanned most of a 120° interval (~90° or ~120° step). Positions of the bead centroid in 0.25–0.5-ms intervals before (red) and after (green) these main steps are shown in the insets of Fig. 4. At 2 μM and 20 μM ATP, red and green spots are separated by ~30°, showing the presence of substeps, whereas spots overlap with each other at 2 mM ATP. The traces are distorted, presumably because of oblique rotation on an obliquely situated F_1. Circles on each trace are the projection of three equally spaced pairs of dwell positions on a circular trajectory oblique to the surface. A search for the best fit with the observed traces show the separation between red and green circles to be 29° ± 7° (mean ± s.d.) for 13 runs at 2, 6 and 20 μM ATP; and 4° ± 3° for 7 runs at 2 and 6 mM.

Figure 5 shows histograms of angular positions. Separations of peaks at 20 μM ATP (crosses) averaged 35° ± 13° (mean ± s.d. for 15 peak pairs). Substeps are less obvious at 2 μM, but histograms for the 2-ms intervals before and after the main steps (green) show similar peak separations. Taking these and other experimental uncertainties into account, we estimate the substep sizes to be within 90° ± 10° and 30° ± 10°.

Steps are fast

Consecutive steps in a rotation record at 2 mM ATP are super-

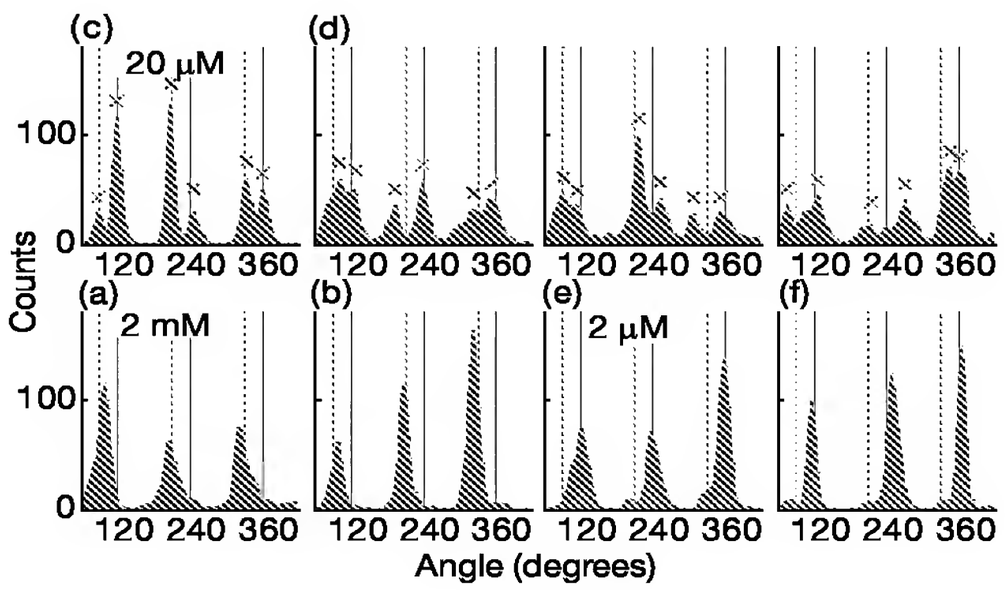

Figure 5 Histograms of angular positions over 0.5 s runs. Labels (a–f) are from records of which Fig. 4, **a**–**f** are a part. Each time course was passed through a five-point median filter, and its histogram was calculated with 2° bins. The histogram was then averaged over 10° intervals. Green parts (**e** and **f**) indicate 2 ms before and after main steps. Crosses indicate peaks identified by eye. To assess the baseline noise in raw data, we also constructed unfiltered, unaveraged histograms at 2 μM ATP with 2° bins (not shown). The histograms gave three peaks, of which the half width at 1/e height was estimated by fitting each peak with a gaussian curve; the half widths averaged 18° ± 7° (mean ± s.d. for 15 peaks).

© 2001 Macmillan Magazines Ltd

imposed in Fig. 6a. The average (thick cyan line) shows that a whole 120° step completes within 0.25 ms (two frames) at saturating ATP. This value is an upper boundary because faster transients are unresolved with the camera that we used. Thus, time for the mechanical stepping (the times needed to reorientate the γ-subunit through 90° and 30°) occupies < 10% of the ATPase cycle time. The 90° substeps at 2 μM ATP are also within 0.25 ms (Fig. 6b). Stepping is fast, the instantaneous speed being well above 1,000 r.p.s., whether [ATP] is above or below K_m for rotation.

Substeps of 90° by ATP binding and 30° by product release

Figure 6c shows averages of all steps observed at indicated [ATP]. Presence of distinct and fast ~90° substeps is clear at all [ATP] < 60 μM, although whether the remaining ~30° is also stepwise cannot be judged in this figure. Fit with grey lines indicates the substep size to be 90.2° ± 0.3°.

The averaging was made after steps other than the central one were eliminated from each step record, such that it started with a near −30° dwell and ended with a ~120° dwell. When the last dwell at 120° was too short to be distinguished, the previous dwell at ~90° was extended to the right edge of the figure (see Methods). Thus, the portion of the curves between −30° and 0° reflects the distribution of dwell times at 0° that were started at the end of a substep from −30° to 0°, and terminated by a central 90° substep. The dwell is [ATP]-dependent, and can be explained by termination by ATP binding at the rate $k_{on}^{ATP} = 3.0 \times 10^7\ M^{-1}\ s^{-1}$ estimated from Fig. 8 (Fig. 6c; grey lines). The kinetics above 90°, in contrast, is [ATP]-independent, except that the amplitude decreases with [ATP]. The decrease is accounted for by the fact that, at [ATP] > K_m, the dwell at ~120° becomes too short and is not represented in our averaging procedure. As shown (grey lines), the kinetics are in accord with the scheme in Fig. 7a where two ~1-ms reactions govern the dwell at ~90° (the two reactions are deduced from Fig. 8).

Our proposed scheme is summarized in Fig. 7a. ATP binding drives a 90° substep (A→B). Next are hydrolysis reactions that are mechanically silent (B, C). Eventually, the last hydrolysis product of the previously bound ATP (ADP, phosphate, or both) is released, accompanying a 30° substep (C→A′) and resetting the system to the initial A state except for the 120° rotation that has taken place. At high [ATP], another 90° substep occurs immediately, and thus the two substeps are not resolved (Fig. 7b)—this is why we propose that both of the hydrolysis products must have been released by the end of a 30° substep. At [ATP] ~ K_m, ATP binding and hydrolysis take similar time, and 90° and 30° substeps are equally spaced.

Two ~1-ms reactions before a next step

Figure 8a shows histograms of dwell times between two main steps (90° or 120°) that were easily discerned at all [ATP]. At [ATP] ≪ K_m (0.02 and 0.2 μM), the histograms were fitted with a single exponential (pink lines) with a rate proportional to [ATP] (Fig. 8b; open cirlces), indicating that ATP binding alone sets the pace of rotation at these [ATP]. At 2 μM ATP, the histogram starts at the origin at zero dwell and shows a distinct peak, indicating the appearance of another rate-limiting reaction. Between 2 and 60 μM, the histograms are explained, roughly, by the ATP-binding reaction and an ATP-independent, ~0.5-ms^{-1} reaction (Fig. 8b). At [ATP] >> K_m = 15 μM, the histograms still show a distinct peak, indicating the presence of at least two reactions. A fit with two rate constants indicated both to be ~1 ms (Fig. 8b; filled black circles), which, taken together, can account for the 0.5-ms^{-1} reaction at intermediate [ATP]. Thus, at least three rate constants, two for the ~1-ms reactions and one for ATP binding, are required to describe the rotation kinetics at all [ATP]. Global fit to all histograms (green lines) showed k_{on}^{ATP} to be $(3.0 \pm 0.1) \times 10^7\ M^{-1}\ s^{-1}$ (consistent with the estimate from Fig. 3 (above) and previous values in actin[11] and single-fluorophore[18] assays), and the other two rates to be 1.64 ± 0.06 ms^{-1} and 0.71 ± 0.02 ms^{-1}. Of the latter two reactions, we cannot discriminate which is first, and the two rates do not differ significantly (see also Fig. 8b).

Thus we propose in Fig. 7a that two ~1-ms dwells separate the 90° and 30° substeps. A simple explanation is that the first dwell is terminated by release of a hydrolysis product (phosphate or ADP) and the second by release of the other product. Alternatively, the first reaction may be splitting of ATP to ADP and phosphate, and the second reaction the release of the two. Either interpretation is

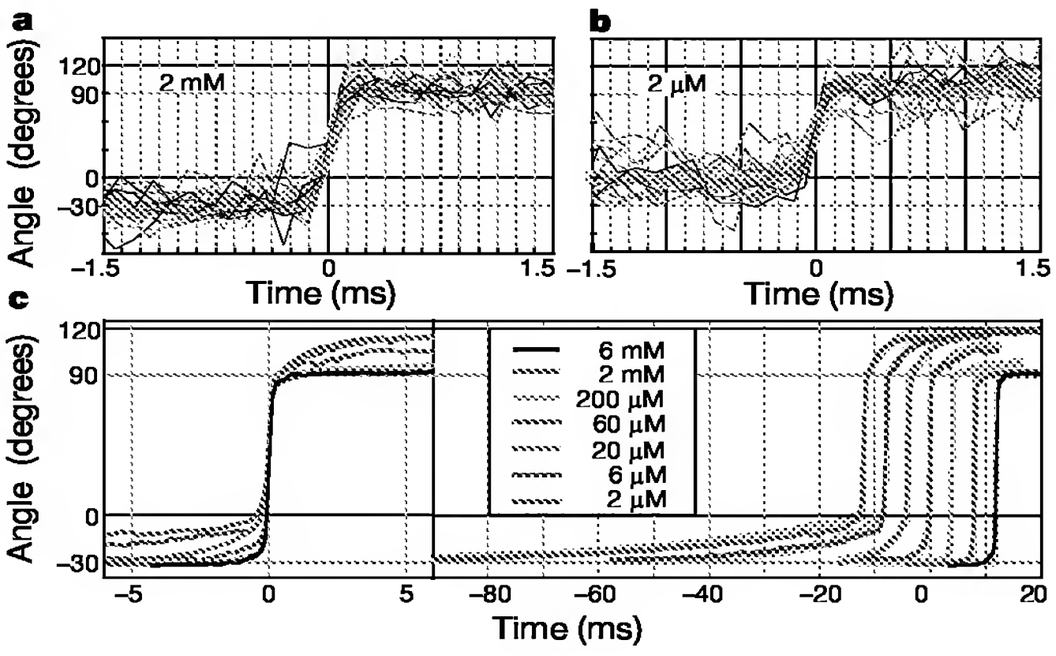

Figure 6 Kinetics of substeps. **a**, **b**, Eighteen consecutive steps and their average (thick cyan line) in a rotation record at 2 mM (**a**) or 2 μM (**b**) ATP (see Methods for the averaging procedure). **c**, Steps in several runs at indicated [ATP], averaged as in **a** and **b**. The averaging procedure retained all dwells at ~0° position in the ordinate, but some dwells at ~120° were converted to a horizontal line at ~90° position when the substep from 90° to 120° was contiguous (within 0.25 ms) with the next substep from 120° to 210°. This is why the curves at high [ATP] do not rise much beyond the 90° line. The curves are reproduced on the right; superimposed grey lines represent fits with theoretical curves based on the scheme in Fig. 7a (see Methods). The best fit was obtained with the size of the 30° substep, $A_{30°}$, of 29.8° ± 0.3° (mean ± s.e.m.).

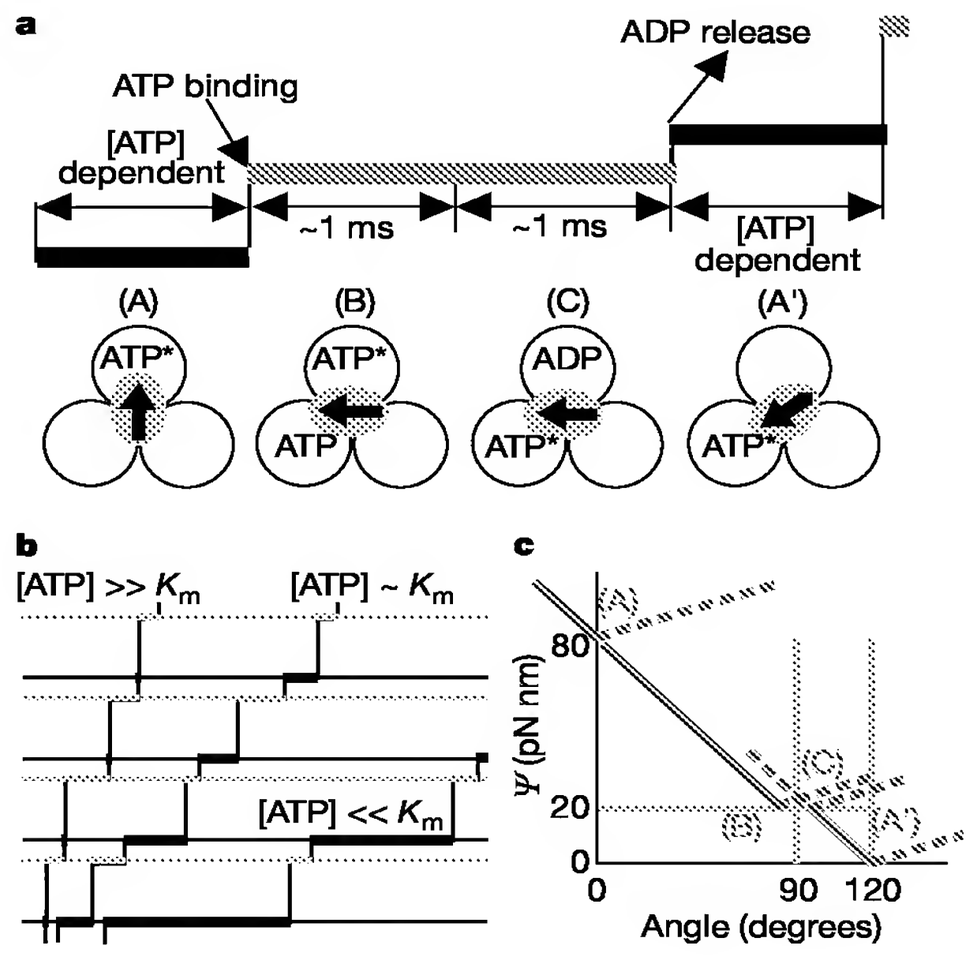

Figure 7 Proposed mechanism for F_1 rotation. **a**, Rotation scheme. ATP with asterisk represents ATP or ADP + phosphate; ADP (alone) may be phosphate or ADP + phosphate. **b**, Stepping time courses expected from **a**. **c**, Highly schematic diagram for the potential energy Ψ for γ-subunit rotation. Each coloured line shows Ψ in one of the four states in **a**. The orientation of the γ-subunit in state A (in **a**) is taken as 0°.

© 2001 Macmillan Magazines Ltd

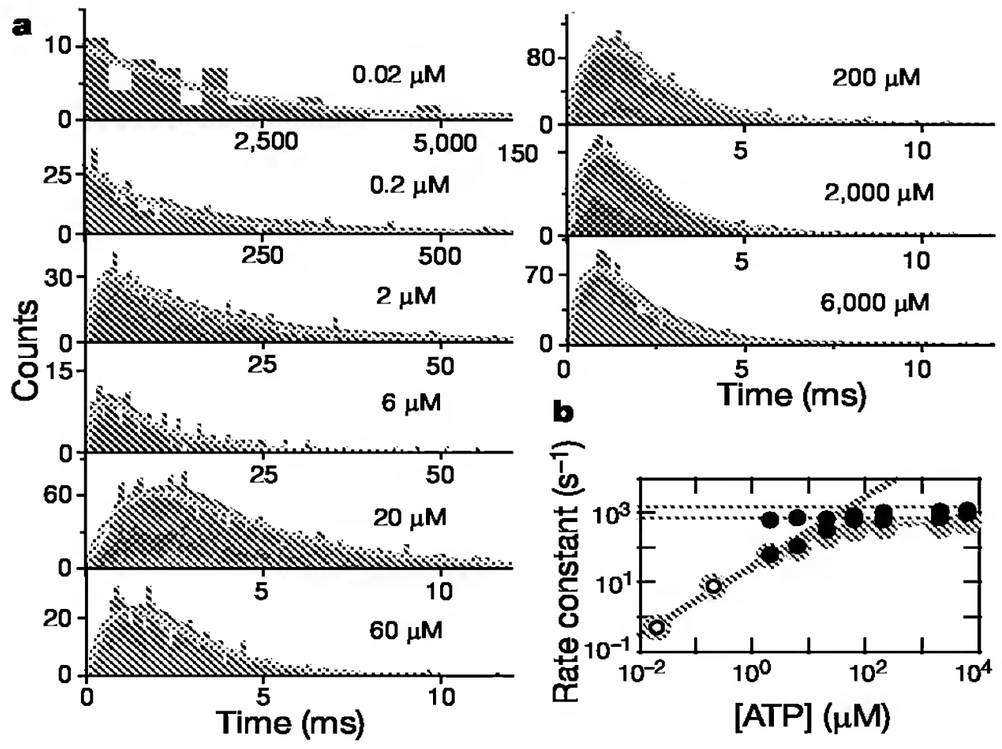

Figure 8 Dwells between main steps. **a**, Histograms of dwell times between two main (90° or 120°) steps at various [ATP]. Total counts in each histogram are 60, 463, 1,145, 2,862, 631, 2,384, 3,262 and 1,457 in the order of 0.02–6,000 μM. Histograms for individual runs are distinguished by colours; they are added to constitute a whole histogram. Pink lines at 0.02 and 0.2 μM ATP are single-exponential fits, constant·exp(–kt), with k shown in open circles in **b**. Pink lines at other [ATP] are fits with two rate constants, constant·[exp(–$k_a t$) – exp(–$k_b t$)], with k_a and k_b shown (filled black circles in **b**). Green lines show the result of a global fit to the individual histograms (n = 38; equal weight for each count) with sequential reactions (Fig. 7a) starting with ATP binding at the rate k_{on}^{ATP}[ATP] and two ATP-independent reactions with rates k_1 and k_2: $k_{on}^{ATP} = (3.0 \pm 0.1) \times 10^7\ M^{-1}\ s^{-1}$, $k_1 = 1.64 \pm 0.06\ ms^{-1}$, and $k_2 = 0.71 \pm 0.02\ ms^{-1}$ (s.e.m.). **b**, ATP dependence of the rate constants. Blue circles show the total rate, k or $k_a k_b/(k_a + k_b)$ for the individual fits. Green lines show the rate constants obtained in the global analysis, and the total rate, $[k_1^{-1} + k_2^{-1} + (k_{on}^{ATP}[ATP])^{-1}]^{-1}$, is shown by the blue line.

consistent with the biochemical evidence that the releases of ADP and phosphate occur at similar rates[21].

Discussion

In our rotation scheme (Fig. 7a) one or two of the three catalytic sites are filled at any time with ATP or its product(s) of hydrolysis. This is the so-called bi-site mechanism[2,3,17], which is the norm at least at submicromolar [ATP]. Previously we have demonstrated rotation at [ATP] as low as 20 nM, indicating that bi-site hydrolysis accompanies rotation[11] and that bi-site is the fundamental mode of rotation[17]. Present results suggest bi-site to be the norm also at physiological (mM) [ATP]. Alternation between two-filled and three-filled states (the tri-site mechanism) has been proposed for hydrolysis at high [ATP], from non-Michaelis–Menten kinetics[22,23] as in Fig. 3, and from quenching of tryptophan fluorescence in the active sites[24]. These results indicating the tri-site mechanism may have been influenced by the MgADP inhibition[25]. In contrast, ATP synthesis by ATP synthase is insensitive to the inhibition and seems to proceed by a bi-site mechanism[26]. Our rotation assay focuses only on active F_1, and is unaffected by the inhibition. The rotation rate was higher than one-third of the hydrolysis rate at all [ATP] (Fig. 3), implying that part of F_1 in solution was not fully active already at several seconds after exposure to ATP. We do not necessarily deny possible occupancy of three sites, but we claim that filling all sites does not significantly accelerate, nor add power to, rotation.

Presence of the substeps indicates the appearance of two metastable structures during rotation, in which the equilibrium positions of the γ-subunit differ by ~90° (Fig. 7a: A versus B or C). If our bi-site interpretation is correct, the crystal structure in Fig. 1a probably corresponds to the two-nucleotide structure B (or C). The other central structure with one nucleotide (A) is yet to be solved. A structure[27] reported recently indicates that the protruding portion of the γ-subunit, where the bead was attached, is torsionally flexible, therefore it is possible that the substeps revealed here might be an artefact: intrinsic steps of the γ-subunit are always 120°, whereas the bead is somehow obstructed at 90° and lags behind for a few ms. We dismiss this possibility because (1) the bead rotated over 120° within 0.25 ms at 2 mM ATP; (2) the dwell time at 90° was independent of the radius of bead rotation, which presumably reflects differences in bead attachment; and (3) larger beads did not show any sign of obstruction.

In Fig. 7a, binding of ATP drives the 90° substep. By reciprocity, the affinity of the β-subunit for ATP, on the left of the arrow on the central γ-subunit, must increase as the γ-subunit rotates[6,16,17,28]. Likewise, because release of ADP (or phosphate, or both) drives the 30° substep, the affinity of the β-subunit for ADP, on the right of the arrow, must decrease as the γ-subunit rotates over the last 30°. The magnitude of these affinity changes can be estimated as below. We have shown that, at least under a high load, F_1 does 80–90 pN nm of mechanical work per 120° step[11] and that the torque it produces is nearly independent of the rotation angle[16,17] (the potential energy Ψ for γ-subunit rotation is linearly downhill). Rotation of 291-nm beads gave similar results (R.Y., unpublished observations). These results, combined with Fig. 7a, suggest the diagram in Fig. 7c for Ψ: in state A in Fig. 7a, Ψ_A is minimal at 0°; ATP binding produces state B where Ψ_B is linearly downhill toward its minimum at ~90°; Ψ_C is also minimal at ~90°; product release recovers state A′ where $\Psi_{A'}$ is again linearly downhill toward 120°. Solid lines have the constant slope of 80 pN nm of work per 120° as indicated by experiment, whereas dashed lines are drawn arbitrarily to provide minima at experimental positions. Affinity for ATP is proportional to $\exp[(\Psi_A - \Psi_B)/k_BT]$, where k_BT ~4.1 pN nm is the thermal energy at room temperature[6,28]. Thus, rotation from 0° to 90° accompanies an increase in the affinity of more than $\exp[(60\ pN\ nm)/k_BT] \sim 2 \times 10^6$. The affinity for ADP, $\propto \exp[(\Psi_{A'} - \Psi_C)/k_BT]$, decreases more than $\exp[(20\ pN\ nm)/k_BT] \sim 10^2$.

These affinity changes account for ATP synthesis by forced clockwise rotation of the γ-subunit. Starting from state A′ in Fig. 7a, the affinity for ADP of the empty β-subunit on the right of the arrow increases as the γ-subunit rotates clockwise, and this β-subunit will pick up ADP from the medium. Further rotation decreases the affinity for ATP of the β-subunit carrying the previously synthesized ATP (on the left of the arrow), and this ATP will eventually be released. In this simple scheme, it is the central, asymmetrical γ-subunit that dictates which of the three β-subunits should change its affinity, and to what extent. A corollary of the 'γ-dictator model' is that tri-site operation may take place during hydrolysis if ADP release is somehow slowed down, for example by partial inhibition. After a 90° substep, the γ-subunit is already pointing close to the next β-subunit and signals this β-subunit to bind ATP. ATP binding may therefore occur without waiting for the 30° substep accompanying ADP release; however, this would be an inefficient tri-site mechanism with no additional power and speed, as we claim above.

Synthesis (or hydrolysis) of ATP on a β-subunit does not require much energy, because ATP and ADP + phosphate are in equilibrium on the β-subunit[21,26]. This is in accord with our observation that the hydrolysis reaction, which we presume to occur during the two ~1-ms reactions, is mechanically silent. The principal function of hydrolysis is to allow the release of bound ATP by converting it to products, thereby resetting the machine for the next round of stepping. Complete mechanical silence, however, is unfavourable for efficient ATP synthesis, because clockwise rotation should release ATP, not ADP + phosphate. Indeed, it has been indicated that the equilibrium shifts toward ATP during synthesis[26]. One such mechanism (a switch-less model for F_1 motor[16,17]) is suggested in Fig. 7c, where the minimum in Ψ_C (after hydrolysis) is placed slightly to the right of the minimum in Ψ_B (before hydrolysis). Such a slight shift would be undetectable at the present resolution.

© 2001 Macmillan Magazines Ltd

Our work is essentially a consolidation and embodiment of the binding-change model[1–3]. Similar to F_1-ATPase, myosin hosts ATP and its hydrolysis product at near equilibrium[29,30]. This may be the general tactics adopted by many ATP-dependent molecular machines. If so, much of the free-energy drop accompanying ATP hydrolysis occurs in the ATP-binding step[17,29,30]. ATP binding may be the principal source of power in these molecular machines. Indeed, ATP binding induces large conformational changes in molecules such as myosin[31], kinesin[32,33] and chaperonin[34]. □

Methods

Proteins

A mutant (α-C193S, β-His_{10} at amino terminus, γ-S107C, γ-I210C) $\alpha_3\beta_3\gamma$ subcomplex (referred to here as F_1) derived from a thermophilic *Bacillus* PS3 was biotinylated at two cysteines (γ-107C and γ-210C) by incubation with fourfold molar excess of 6-*N*′-[2-(*N*-maleimido)ethyl]-*N*-piperazinylamidohexyl-D-biotinamide for 1 h at 23 °C. Unbound biotin was removed with PD10 (Amersham Pharmacia). Two biotin moieties per protein were found in an assay using 4-hydroxyazobenzene-2-carboxylic acid[35]. Eight molar excess of streptavidin (Pierce) was added to the biotinylated F_1 and purified on Superdex-200HR (Amersham Pharmacia).

Beads

Colloidal gold (diameter 40 nm; British BioCell International) was coated with biotinylated BSA by incubating 0.2% colloidal gold in 2 mM potassium phosphate pH 7.0 with 0.4 mg ml^{-1} BSA and 0.2 mg ml^{-1} sulphosuccinimidyl-*N*-[*N*′-(D-biotinyl)-6-aminohexanoyl]-6′-aminohexanoate (biotin-$(AC_5)_2$ sulpho-OSu; Dojin) for 1 h at 23 °C. We stored modified gold particles in a solution containing 2 mM potassium phosphate and 0.05% polyethylene glycol. Polystyrene beads were biotinylated as follows: 2.7% amino beads (108 nm; Polyscience) in 20 mM potassium phosphate pH 7.0 was incubated with 1 mg ml^{-1} of biotin-$(AC_5)_2$ sulpho-OSu for 1 h at 23 °C. We incubated 2.5% of carboxy beads (196 or 291 nm; Bangs) in 20 mM potassium phosphate with 3.6 mM 5-(((*N*-(biotinoyl)amino)hexanoyl)amino)pentylamine trifluoroacetate salt (Molecular Probes), 1% 1-ethyl-3-(3-dimethylaminopropyl)-carbodiimide hydrochloride and 1% *N*-hydroxysulphosuccinimide for 1 h at 23 °C.

Rate of ATP hydrolysis

Nucleotide-depleted F_1 was prepared[18], and its ATPase activity was determined at 23 °C with an ATP-regenerating system[18,36] containing 1 mM phosphoenolpyruvate, 200 μg ml^{-1} pyruvate kinase, 100 μg ml^{-1} lactate dehydrogenase, 0.15 mM NADH, and indicated MgATP in buffer A (50 mM KCl, 2 mM $MgCl_2$, 10 mM 3-[*N*-morpholino]propanesulfonic acid-KOH, pH 7.0). The initial hydrolysis rate was determined from the slope of absorbance decrease at 340 nm; the average slope was estimated for the period of 2–5 s (2 mM–12 μM ATP), 2–7 s (6–2 μM) or 2–12 s (0.2–0.06 μM) after the start of the reaction. In the presence of LDAO, hydrolysis kinetics showed a lag, and thus the rate was estimated at steady state during 400–500 s (2 mM–60 μM), 1,000–1,500 s (20–6 μM) or 4,500-5,000 s (2–0.6 μM).

Microscopy

Beads of 196 nm and 291 nm were observed with transmitted light on an Olympus IX-70 microscope. We observed 40-nm and 108-nm beads with laser dark-field microscopy[12] (Fig. 1c). A laser beam (532 nm, diameter 3 mm, 200 mW; Millenia II, Spectra Physics) was introduced into a dark-field condenser (numerical aperture, NA 1.2–1.4; Olympus) to illuminate the specimen obliquely. Light scattered by beads was collected with a ×100 objective (NA1.35; Olympus) with its iris diaphragm set to NA ~1.1 to block the direct ray. The field of view was ~50 μm. To confirm that we observed single 40-nm beads and not their aggregates, we measured the intensity of beads with regular dark-field microscopy with a halogen lamp, which provided homogeneous illumination. The intensity distribution had a single, large peak and a second small peak at four times the intensity of the first peak. Because an object smaller than the wavelength scatters light in proportion to the square of its volume[37], these peaks should correspond to single and duplex beads. Most beads were thus single. Twenty-fold reduction in the laser intensity did not affect the rotation speed, indicating that heating by the laser was insignificant.

Bead rotation assay

A flow cell was made of two KOH-cleaned coverslips separated by two spacers with 50 μm thickness[11]. Mixture of 0.1–1 nM beads and F_1 at 10–100 times the bead concentration in buffer B (buffer A plus 5 mg ml^{-1} BSA) was applied to the flow cell. Unbound beads were washed out with buffer B, and then buffer B plus MgATP (Mg^{2+} 2 mM in excess), 0.1 mg ml^{-1} creatine kinase, and 1 mM creatine phosphate was infused. Bead images were recorded as an eight-bit AVI file with a fast framing CCD camera (HiD-Cam, Nac) at 8,000 frames per s at [ATP] ≥ 2 μM; 125 frames per s at 0.2 μM; and 60 frames s^{-1} at 0.02 μM. The temperature was 23 °C. From each unmodified image, the bead centroid was calculated as $\Sigma x_i(I_i - I_{th})/\Sigma(I_i - I_{th})$, where x_i (or y_i) is the pixel coordinate, I_i the pixel intensity, I_{th} a threshold value, and the summation was for $I_I \geq I_{th}$.

The rotational frictional drag coefficient ξ for the beads was calculated as follows: for a single bead of radius a rotating in water with viscosity η (= 10^{-9} pN nm^{-2} s), minimal ξ is given by $8\pi\eta a^3$ when the rotation axis is at the bead centre, and maximal ξ by $8\pi\eta a^3 + 6\pi\eta a^3 = 14\pi\eta a^3$ when the axis is at a bead edge; for a bead duplex, minimal ξ is given by $2\times 8\pi\eta a^3 = 16\pi\eta a^3$ for a vertical duplex rotating around its centre, whereas maximal ξ is $2\times 8\pi\eta a^3 + 6\pi\eta a^3 + 6\pi\eta a\,(3a)^2 = 76\pi\eta a^3$ for a horizontal duplex rotating around an edge.

Analysis of substep kinetics

We superimposed and averaged time courses of individual steps as in Fig. 6a, b. First, we identified all main (90° or 120°) steps in a continuous run by eye. Then, individual steps were aligned on the time axis by positioning the midpoint of each step at time 0 (to within ± one frame). Vertical alignment was made by shift, by multiples of 120°. Next, steps other than the central one were eliminated from individual step records: the part earlier than 0.25 ms after the preceding 90° substep (or 120° step when substeps were contiguous) was replaced with a horizontal line at the angle at the 0.25-ms point (for example, a red line in Fig. 6a), and the part later than 0.25 ms before the following 90° substep (or 120° step) was replaced with the angle at that point (Fig. 6a; red line). Finally, we averaged all step records (Fig. 6a, b; thick cyan lines).

Step records averaged over several runs (Fig. 6c; coloured lines) were fitted with theoretical kinetics (Fig. 6c; grey lines) on the basis of the scheme in Fig. 7a; rate constants in the scheme were fixed to the values determined in Fig. 8. For the [ATP]-dependent kinetics for the rise from −30° to 0°, the grey lines show $A_{30°}\cdot\exp(k_{on}^{ATP}[ATP]t) - A_{30°}$, where $A_{30°}$ is the size of the 30° substep, $k_{on}^{ATP} = 3.0\times 10^7$ M^{-1} s^{-1}, and t (< 0) is time from the central 90° substep. For the rise from 90° to 120°, two reactions with rates $k_1 = 1.64$ ms^{-1} and $k_2 = 0.71$ ms^{-1} are assumed, giving $A_{30°}\cdot B\cdot\{1 - [k_2\exp(-k_1 t) - k_1\exp(-k_2 t)]/(k_2 - k_1)\} + (120° - A_{30°})$ where $B = \exp(-k_{on}^{ATP}[ATP]\cdot 0.25\ ms)$ accounts for the loss of some of the 30° substeps in the averaging process . Global fit to all experimental curves (allowing a vertical shift for each curve) yielded $A_{30°} = 29.8 \pm 0.3°$.

Received 4 October 2000; accepted 26 February 2001.

1. Boyer, P. D. & Kohlbrenner, W. in *Energy Coupling in Photosynthesis* (eds Selman, B. R. & Selman-Reimer, S.) 231–240 (Elsevier, Amsterdam, 1981).
2. Boyer, P. D. The binding change mechanism for ATP synthase—some probabilities and possibilities. *Biochim. Biophys. Acta* **1140,** 215–250 (1993).
3. Boyer, P. D. Catalytic site forms and controls in ATP synthase catalysis. *Biochim. Biophys. Acta* **1458,** 252–262 (2000).
4. Cox, G. B., Jans, D. A., Fimmel, A. L., Gibson, F. & Hatch, L. The mechanism of ATP synthase. Conformational change by rotation of the b-subunit. *Biochim. Biophys. Acta* **768,** 201–208 (1984).
5. Mitchell, P. Molecular mechanics of protonmotive F_oF_1 ATPases. Rolling well and turnstile hypothesis. *FEBS Lett.* **182,** 1–7 (1985).
6. Oosawa, F. & Hayashi, S. The loose coupling mechanism in molecular machines of living cells. *Adv. Biophys.* **22,** 151–183 (1986).
7. Abrahams, J. P., Leslie, A. G. W., Lutter, R. & Walker, J. E. Structure at 2.8 Å resolution of F_1-ATPase from bovine heart mitochondria. *Nature* **370,** 621–628 (1994).
8. Duncan, T. M., Bulygin, V. V., Zhou, Y., Hutcheon, M. L. & Cross, R. Rotation of subunits during catalysis by *Escherichia coli* F_1-ATPase. *Proc. Natl Acad. Sci. USA* **92,** 10964–10968 (1995).
9. Sabbert, D., Engelbrecht, S. & Junge, W. Intersubunit rotation in active F-ATPase. *Nature* **381,** 623–625 (1996).
10. Noji, H., Yasuda, R., Yoshida, M. & Kinosita, K. Jr Direct observation of the rotation of F_1-ATPase. *Nature* **386,** 299–302 (1997).
11. Yasuda, R., Noji, H., Kinosita, K. Jr & Yoshida, M. F_1-ATPase is a highly efficient molecular motor that rotates with discrete 120° steps. *Cell* **93,** 1117–1124 (1998).
12. Kudo, S., Magariyama, Y. & Aizawa, S. Abrupt changes in flagellar rotation observed by laser dark-field microscopy. *Nature* **346,** 677–680 (1990).
13. Miyata, H. *et al.* Stepwise motion of an actin filament over a small number of heavy meromyosin molecules is revealed in an *in vitro* motility assay. *J. Biochem. (Tokyo)* **115,** 644–647 (1994).
14. Weber, P. C., Ohlendorf, D. H., Wendoloski, J. J. & Salemme, F. R. Structural origins of high-affinity biotin binding to streptavidin. *Science* **243,** 85–88 (1989).
15. He, X. M. & Carter, D. C. Atomic structure and chemistry of human serum albumin. *Nature* **358,** 209–215 (1992).
16. Kinosita, K. Jr, Yasuda, R. & Noji, H. F_1-ATPase: a highly efficient rotary ATP machine. *Essays Biochem.* **35,** 3–18 (2000).
17. Kinosita, K. Jr, Yasuda, R., Noji, H. & Adachi, K. A rotary molecular motor that can work at near 100% efficiency. *Phil. Trans. R. Soc. Lond. B* **355,** 473–489 (2000).
18. Adachi, K. *et al.* Stepping rotation of F_1-ATPase visualized through angle-resolved single-fluorophore imaging. *Proc. Natl Acad. Sci. USA* **97,** 7243–7247 (2000).
19. Jault, J.-M. *et al.* The $\alpha_3\beta_3\gamma$ complex of the F_1-ATPase from the thermophilic *Bacillus* PS3 containing the $\alpha D_{261}N$ substitution fails to dissociate inhibitory Mg ADP from a catalytic site when ATP binds to noncatalytic sites. *Biochemistry* **34,** 16412–16418 (1995).
20. Matsui, T. *et al.* Catalytic activity of the $\alpha_3\beta_3\gamma$ complex of F_1-ATPase without noncatalytic nucleotide binding site. *J. Biol. Chem.* **272,** 8215–8221 (1997).
21. Cunningham, D. & Cross, R. L. Catalytic site occupancy during ATP hydrolysis by MF_1-ATPase. Evidence for alternating high affinity sites during steady-state turnover. *J. Biol. Chem.* **263,** 18850–18565 (1988).
22. Gresser, M. J., Myers, J. A. & Boyer, P. D. Catalytic site cooperativity of beef heart mitochondrial F_1 adenosine triphosphatase. Correlations of initial velocity, bound intermediate, and oxygen exchange measurements with an alternating three-site model. *J. Biol. Chem.* **257,** 12030–12038 (1982).
23. Jault, J.-M. *et al.* The $\alpha_3\beta_3\gamma$ subcomplex of the F_1-ATPase from the thermophilic *Bacillus* PS3 with the βT165S substitution does not entrap inhibitory MgADP in a catalytic site during turnover. *J. Biol. Chem.* **271,** 28818–28824 (1996).
24. Weber, J., Wilke-Mounts, S., Lee, R. S., Grell, E. & Senior, A. E. Specific placement of tryptophan in the catalytic sites of *Escherichia coli* F_1-ATPase provides a direct probe of nucleotide binding: maximal ATP hydrolysis occurs with three sites occupied. *J. Biol. Chem.* **268,** 20126–20133 (1993).
25. Milgrom, Y. M., Murataliev, M. B. & Boyer, P. D. Bi-site activation occurs with the native and nucleotide-depleted mitochondrial F_1-ATPase. *Biochem. J.* **330,** 1037–1043 (1998).

© 2001 Macmillan Magazines Ltd

26. Zhou, J.-M. & Boyer, P. D. Evidence that energization of the chloroplast ATP synthase favors ATP formation at the tight binding catalytic site and increases the affinity for ADP at another catalytic site. *J. Biol. Chem.* **268,** 1531–1538 (1993).
27. Gibbons, C., Montgomery, M. G., Leslie, A. G. W. & Walker, J. E. The structure of the central stalk in bovine F_1-ATPase at 2.4 Å resolution. *Nature Struct. Biol.* **7,** 1055–1061 (2000).
28. Wang, H. & Oster, G. Energy transduction in the F_1 motor of ATP synthase. *Nature* **396,** 279–282 (1998).
29. Wolcott, R. G. & Boyer, P. D. The reversal of the myosin and actomyosin ATPase reactions and the free energy of ATP binding to myosin. *Biochem. Biophys. Res. Commun.* **57,** 709–716 (1974).
30. Mannherz, H. G., Schenck, H. & Goody, R. S. Synthesis of ATP from ADP and inorganic phosphate at the myosin-subfragment 1 active site. *Eur. J. Biochem.* **48,** 287–295 (1974).
31. Houdusse, A., Szent-Györgyi, A. G. & Cohen, C. Three conformational states of scallop myosin S1. *Proc. Natl Acad. Sci. USA* **97,** 11238–11243 (2000).
32. Rice, S. *et al.* A structural change in the kinesin motor protein that drives motility. *Nature* **402,** 778–784 (1999).
33. Schnitzer, M. J., Visscher, K. & Block, S. M. Force production by single kinesin motors. *Nature Cell Biol.* **2,** 718–723 (2000).
34. Sigler, P. B. *et al.* Structure and function in GroEL-mediated protein folding. *Annu. Rev. Biochem.* **67,** 581–608 (1998).
35. Kunioka, Y. & Ando, T. Innocuous labeling of the subfragment-2 region of skeletal muscle heavy meromyosin with a fluorescent polyacrylamide nanobead and visualization of individual heavy meromyosin molecules. *J. Biochem. (Tokyo)* **119,** 1024–1032 (1996).
36. Kato, Y., Sasayama, T., Muneyuki, E. & Yoshida, M. Analysis of time-dependent change of *Escherichia coli* F_1-ATPase activity and its relationship with apparent negative cooperativity. *Biochim. Biophys. Acta* **1231,** 275–281 (1995).
37. Born, M. & Wolf, E. *Principles of Optics* 7th edn. (Cambridge Univ. Press, Cambridge, 1999).

Supplementary information is available on *Nature's* World-Wide Web site (http://www.nature.com).

Acknowledgements

We thank T. Ariga for sample preparation; A. Kusumi for colloidal gold; T. Hisabori, E. Muneyuki, T. Nishizaka, K. Adachi, C. Gosse, M. Y. Ali, S. Ishiwata and G. W. Feigenson for critical discussions; and H. Umezawa for laboratory management. This work was supported in part by Grants-in-Aid from the Ministry of Education, Science, Sports and Culture of Japan.

Correspondence and requests for materials should be addressed to K.K.

© 2001 Macmillan Magazines Ltd

FEBS 20125 FEBS Letters 426 (1998) 301–304

Three-stepped rotation of subunits γ and ε in single molecules of F-ATPase as revealed by polarized, confocal fluorometry

Katrin Häsler, Siegfried Engelbrecht, Wolfgang Junge*

Div. of Biophysics, Dept. Biology/Chemistry, Universität Osnabrück, D-49069 Osnabrück, Germany

Received 17 March 1998

Abstract The proton translocating ATP synthase is conceived as a rotatory molecular engine. ATP hydrolysis by its headpiece, CF_1, drives the rotation of subunit γ relative to the hexagonally arranged large subunits, $(\alpha\beta)_3$. We investigated transition states of the rotatory drive by polarized confocal fluorometry (POCOF) as applied to single molecules of engineered, immobilized and load-free spinach-CF_1. We found that the hydrolysis of ATP caused the stepped and sequential progression of subunit γ through three discrete angular positions, with the transition states of γ being too shortlived for detection. We also observed the stepped motion of ε, whereas δ was immobile as $(\alpha\beta)_3$.

1998 Federation of European Biochemical Societies.

Key words: ATP synthase; Single molecule; Rotation; Molecular motor

1. Introduction

The proton translocating ATP synthase is conceived as a rotatory molecular engine [1–3]. In the isolated headpiece, F_1, and under conditions of ATP hydrolysis the rotation of subunit γ relative to the hexagonally arranged large subunits, $(\alpha\beta)_3$, has been established experimentally by chemical cross-linking [4], by polarized absorption recovery after photobleaching [5] and by video-microfluorometry [6]. In contrast to the first technique, the latter two are time-resolving (see [3] for a review) with the following virtues and drawbacks: The about 2 μm long fluorescent actin filament in [6] allows the direct observation in the microscope of the *unidirectional* rotation of subunit γ in single molecules of F_1. Because the filament represents a heavy viscous load on subunit γ the maximum torque of this motor has been revealed, but finer motional details were damped out. The photoselection technique in [5], on the other hand, operates with a single dye molecule on subunit γ, i.e. at a negligible load, but the ensemble averaging hinders a rigorous discrimination between random and unidirectional rotation in some special cases. We treated this difficulty by developing a theory of molecular stepping motors [7] that has led to the proposal that the data in [5,8] might indicate a three-stepped rotation of subunit γ. In the present article we describe a new technique, polarized confocal fluorometry (POCOF), that overcomes the remaining ambiguity by combining the benefit of single-molecule spectroscopy with the one of a low load on the enzyme. Within noise limits it revealed a three-stepped rotation of subunit γ and a first assessment of the residence times of subunit γ in the three metastable and the more transient interstitial angular positions (transition states).

2. Materials and methods

A photon-counting fluorescence microscope, the ConfoCor (Carl Zeiss Jena/Evotec, Hamburg, Germany), was used to investigate transients of the angular position of the fluorescent probe on a single molecule of immobilized F_1. The instrument counts fluorescence quanta emitted by single molecules contained in a very small volume element ($<10^{-15}$ l) as defined by the focus of a laser beam (diameter 0.5 μm). Fig. 1B schematically illustrates the focus of the ConfoCor with a γ-labelled molecule of F_1 immobilized at the glass/water interface of a chamber slide.

The headpiece of the ATP synthase from spinach, CF_1 (for chloroplast F_1), was covalently and specifically labelled by a fluorescent probe, a maleimide derivative of tetramethylrhodamine, TMR. The target cysteine residue was located either on subunit γ, ε or δ. The particular residue on γ (C322) was intrinsic [9,10] whereas the residues on ε (S85C) and δ (S10C) were engineered [11,12]. In the latter two cases the engineered subunits were first labelled and then reassociated with unlabelled $CF_1(-\delta, \varepsilon)$. The labelling did not impair the ATPase activity of solubilized CF_1. Labelled and solubilized CF_1 was immobilized by adsorption at the water/glass interface of a chamber slide. Fig. 1A shows the respective positions of the label in a current structural model of CF_1. Fig. 2 shows the selective modifications of the subunits as detected by the fluorescence of the bound dye.

2.1. Preparation of CF_1 and labelling

CF_1 lacking subunits δ and ε ($CF_1(-\delta, \varepsilon)$) was prepared by anion exchange rechromatography [13] of CF_1 prepared from EDTA extracts of spinach chloroplasts [14]. The specific activity of the enzyme was 23 U/mg (measured in 50 mM Tris/HCl, pH 7.8, 5 mM ATP, 2 mM $MgCl_2$, 20% (v/v) methanol, 10 mM Na_2SO_3, 5 min, room temperature). $CF_1(-\delta, \varepsilon)$ was specifically labelled at γ-Cys-322 by treatment at room temperature for 10 min at pH 7.0 (25 mM MOPS/NaOH) with 20 μM tetramethylrhodamine-5-maleimide (TMR-5-M, Molecular Probes, Eugene, OR, USA). The reaction was terminated by addition of 1 mM *N*-acetyl-cysteine. Free dye was separated from labelled protein by gelfiltration (Pharmacia NAP5/25 mM Tris/HCl, pH 7.8). Recombinant subunits δ (S10C) and ε (C6S, S85C) were over-expressed in *E. coli* [15] and purified by anion exchange and hydrophobic interaction chromatography (δ) [11] or cation exchange chromatography (ε) [12]. Both proteins were labelled with tetramethylrhodamine-5-maleimide similarly as $CF_1(-\delta, \varepsilon)$ but at 200 μM TMR and overnight. $CF_1(-\delta, \varepsilon)$ was substituted with either δ or ε or both subunits by addition of molar amounts of δ and a 6-fold molar excess of ε. In the latter case care was taken to keep the total amount of urea below 800 mM (ε was dissolved in 8 M urea). All samples ($CF_1(-\delta, \varepsilon)$+TMR-γ, $CF_1(-\delta, \varepsilon)$+TMR-δ, $CF_1(-\delta, \varepsilon)$+TMR-ε) were gelfiltrated through Pharmacia Superose-12 immediately prior to measurements in the ConfoCor. The column was cleaned by 6 M guanidinium-HCl weekly. Samples (100 μl), irrespective of the content of small subunits, eluted at $V_c = 9.6$ ml. The specific Mg-ATPase activities remained unchanged upon labelling of either subunit γ or after substitution with TMR-δ or TMR-ε. Ca-ATPase activity was decreased from 20 U/mg to 4 U/mg upon substitution with TMR-ε as expected.

2.2. The immobilization of labelled CF_1

The immobilization of labelled CF_1 by adsorption to the glass-

*Corresponding author. Fax: +49 (541) 969 1221.
E-mail: junge@uni-osnabrueck.de

0014-5793/98/$19.00 © 1998 Federation of European Biochemical Societies. All rights reserved.
PII S0014-5793(98)00358-5

buffer interface was monitored by fluorescence autocorrelation spectroscopy, FCS, with the exciting light beam of the ConfoCor focussed into the solution, about 200 μm above the surface of the chamber slide. The concentration was determined by fluorescence autocorrelation analysis using the algorithms, hard- and software by Evotec (Hamburg, Germany). For immobilization of CF_1 a droplet containing 30 μl of 5 nM CF_1 lacking subunits δ and ε and labelled with TMR-5-M within subunit γ ($CF_1(-\delta, \varepsilon)$+TMR-γ) in the presence of a 100-fold excess of unlabelled enzyme was deposited on the chamber slide. It contained 25 mM Tris/HCl, pH 7.8 and either 1 mM Mg-ADP in case of the inhibited enzyme or 20% (v/v) methanol for successive measurements under hydrolyzing conditions. After about 1 min the solution was removed from the slide, exchanged by the respective enzyme-free buffers and left to settle for another 10 min. After this procedure, there were no free CF_1 molecules detectable in the focus spot at about 200 μm depth in the buffer, indicating that the immobilization of the enzyme by adsorption to the glass/water interface was complete.

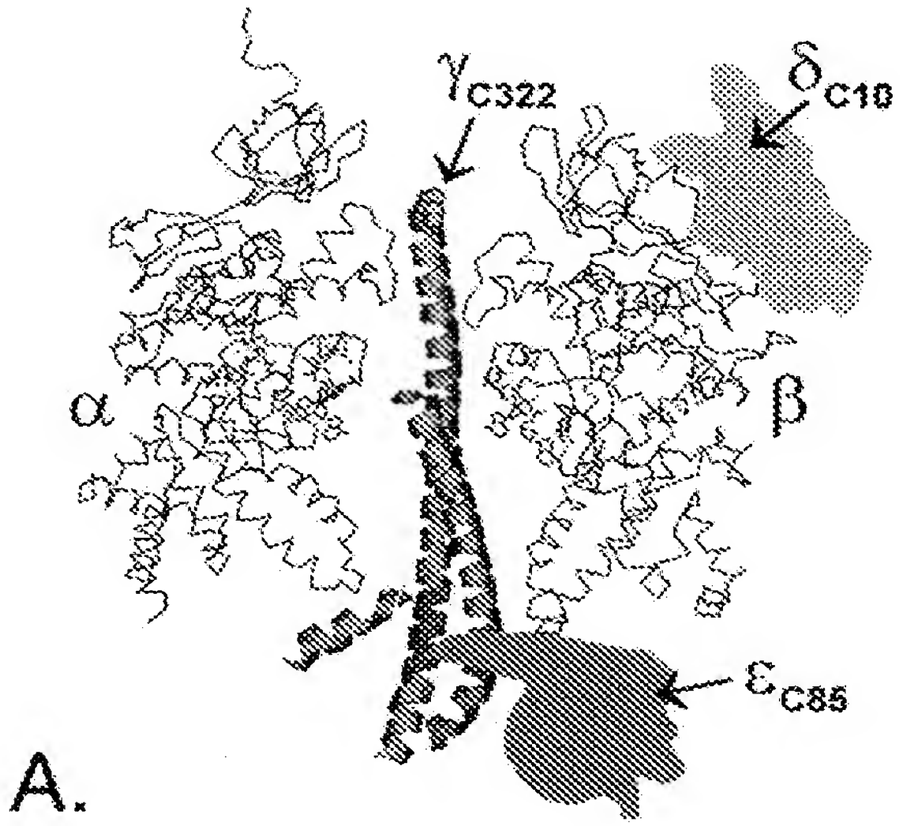

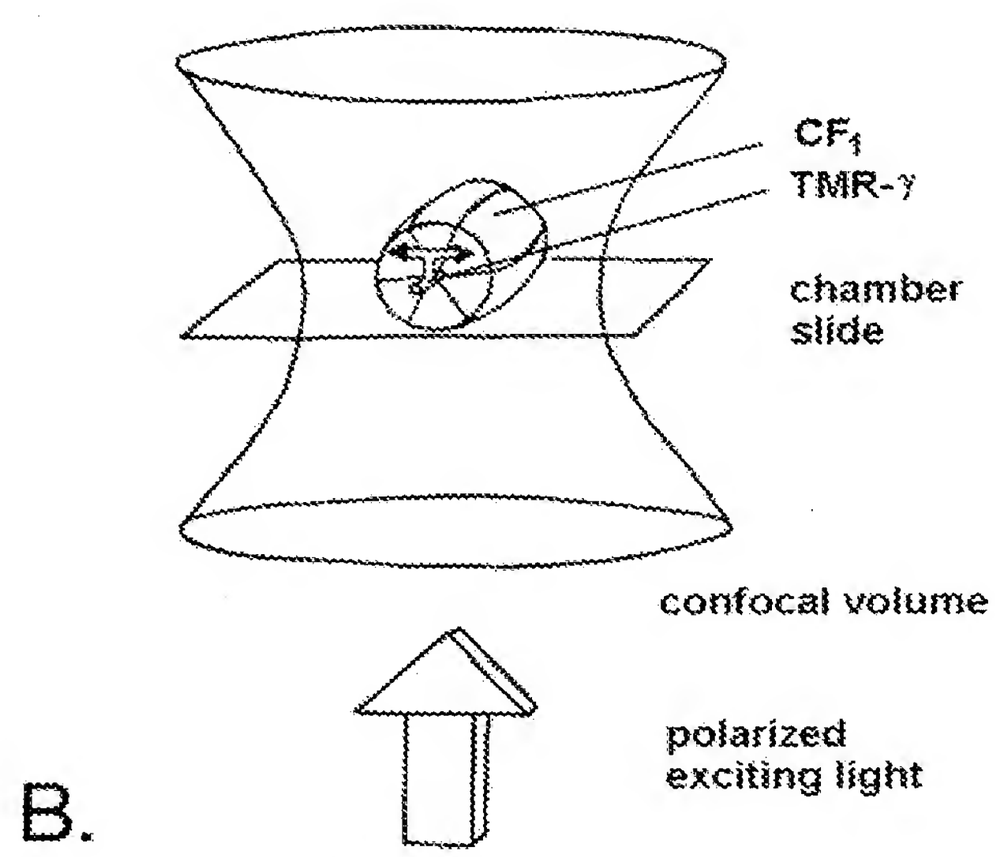

Fig. 1. A: A current *model* of CF_1 [21]. The arrows indicate the respective cysteine residues in subunits γ, δ, and ε that were modified with TMR-5-M. B: The focal volume in polarized confocal fluorometry. The barrel on the surface of the chamber slide denotes immobilized and γ-labelled F_1 (not drawn to scale). The arrow denotes the exciting laser beam and its plane the E-vector of the light.

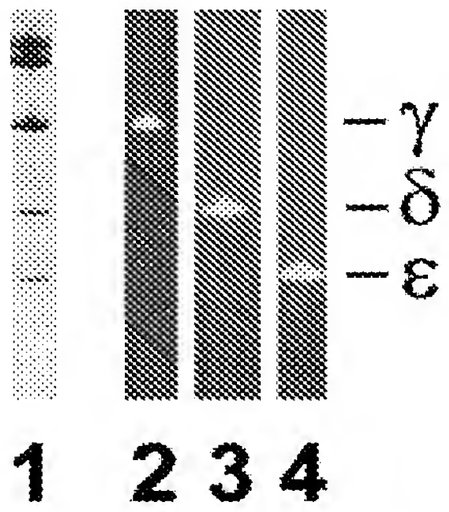

Fig. 2. SDS-gel of CF_1 demonstrating by fluorescence the specific labelling of subunits γ and δ and ε, respectively.

2.3. Intersubunit rotation

Intersubunit rotation was detected with the exciting light beam directly focussed onto the surface of the chamber slide. TMR was excited by continuous linearly polarized focussed argon ion laser, 514 nm (10 mW). Because of the linear polarization of the exciting light, the count rate varied as a function of the orientation of the dye relative to the polarization vector of the beam. This holds true even though the bound dye molecule carries out rapid rotational diffusion (in nano- to microseconds) around its bond axis relative to the protein. This motion diminishes the polarization anisotropy only gradually as demonstrated elsewhere [8].

3. Results and discussion

In a first set of experiments the laser focus was positioned into a droplet containing solubilized CF_1 which was deposited on a chamber slide. The concentration of labelled CF_1 was determined by the ConfoCor operating in the FCS mode (fluorescence correlation spectroscopy) [16]. To avoid too tight a packing of labelled molecules at the interface, we used a 100-fold dilution of labelled in unlabelled CF_1 molecules in the starting solution. The specific Mg-ATPase activity of *immobilized* CF_1 was decreased 10-fold in comparison with the one of the solubilized enzyme.

After 10 min of incubation the laser focus was readjusted to hit immobilized CF_1 at the glass/water interface. The ConfoCor was then used in a new mode, coined POCOF. The principle of POCOF, which stands for polarized confocal fluorometry, is illustrated in Fig. 1B. When the laser beam impinges on the immobilized enzyme molecule in the double-conical focal volume, the angular position of the transition moment of the probe (shown as a double arrow) relative to the linear polarization (flat arrow) of the laser beam determines the probability of excitation ($\cos^2(\alpha)$ law) and thereby the rate of emission of fluorescence quanta. This is why the rotation of the label is expected to cause transients of the fluorescence count rate. Such transients were recorded over an illumination interval of about 5 s. Within this period of time the dye molecule in the focus was irreversibly bleached. The laser beam was then shut off, the focus was horizontally shifted (typically by about 10 μm), and the shutter was reopened for a recording at another spot containing another molecule of labelled CF_1 with a 'fresh' dye molecule. The light stability of rhodamines, the favored dyes in such studies, is of the order of 10^5–10^6 absorbed quanta [17].

3.1. Transients with γ-labelled CF_1

Transients with γ-labelled CF_1 are depicted in Fig. 3. Fig. 3A shows the typical result when the hydrolysis activity was

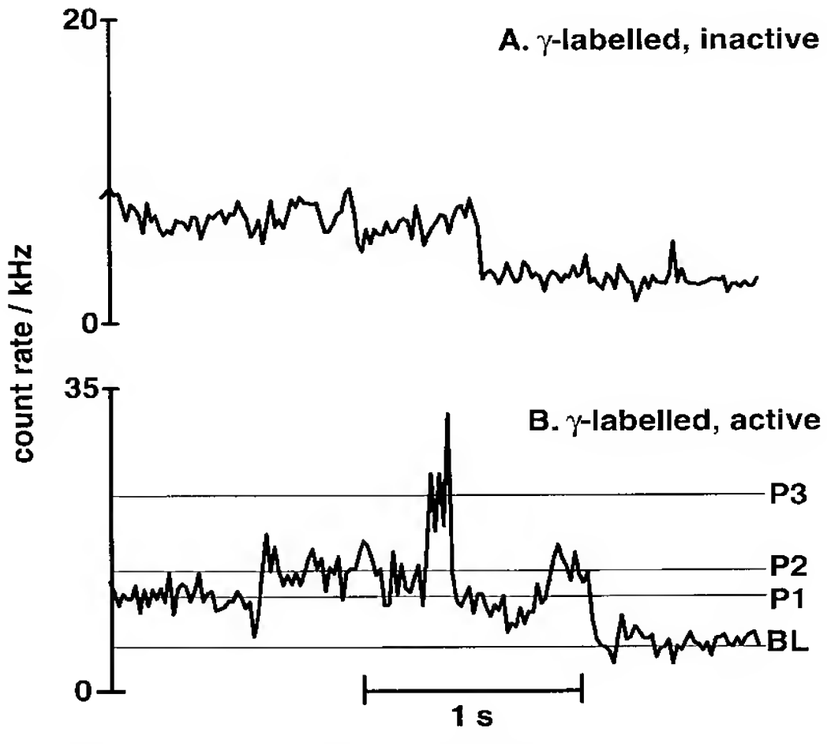

Fig. 3. Transients of fluorescence upon excitation with linearly, polarized light of a single, γ-labelled and immobilized molecule of $CF_1(-\delta, \varepsilon)$. A shows a typical transient under inhibition of the enzyme by ADP. B shows active CF_1 in the presence of ATP: after adsorption of the enzyme to the chamber slide and a 10 min incubation period in the presence of 50 μl 25 mM Tris/HCl, pH 7.8 and 20% (v/v) methanol, 450 μl reaction mixture for ATP hydrolysis (50 mM Tris/HCl, pH 7.8, 5 mM ATP, 2 mM $MgCl_2$, 20% (v/v) methanol, 10 mM Na_2SO_3) were added to the sample. Note the three distinct levels (P1 to P3) of the count rate of fluorescence (as implied by the three thin lines) which indicate three discrete angular positions of the labelled γ relative to $(\alpha\beta)_3$ during the catalytic cycle. The final level, BL, results from the bleaching of the molecule in the very focus.

blocked by the presence of ADP. At zero time, when the photoshutter was opened, the count rate started at a level of 5 kHz. It continued at this level over about 1.5 s, to suddenly break-down to a background level of about 2 kHz. From there on the count rate continuously decayed over more than 10 s. We attributed the count rate of 3 kHz over a background of 2 kHz to a particular single molecule of CF_1 in the very focus and the sudden break-down to the irreversible bleaching of the covalently attached TMR molecule (see [17] for a study on the light stability of TMR). The slower and gradual bleaching of the background level was attributed to molecules in a more unfavorable position at the fringes of the focal volume. The constancy of the count rate until the sudden bleaching occurred, demonstrated that subunit γ was not rotating under these conditions. This interpretation was corroborated by two observations: (1) When the same focal spot was reilluminated after a period of darkness, the high count rate was never revived. (2) When the microscope table was laterally moved to bring a 'fresh' molecule into focus, high count rates with a sudden break-down were observed again. This pattern of a high count rate to start with and a sudden drop to a lower level was observed in over 200 shots with γ-labelled CF_1. Under the same conditions we never observed a sudden rise of the count rate. The only other behavior was a background rate right from the beginning because there was no favorably oriented, labelled enzyme in the focus.

Fig. 3B documents the completely different behavior when γ-labelled CF_1 was hydrolyzing ATP. The count rate started at a low level, P1, to suddenly raise to a higher level, P2, and by another jump to P3, then dropping down to P1, and further up to P2, again. Then the level dropped to a basal level, BL. The latter was attributed to the background after the bleaching of the particular dye molecule in the very focus. We interpreted this behavior as indicating the stepwise progression of subunit γ through three discrete angular positions, P1, P2, and P3. A stepped motion of subunit γ in the presence of ATP was observed in more than 200 experiments, a clearly three-stepped one only in three. This is not astounding in terms of the angular resolution and the noise limits. It is noteworthy that e.g. two angular positions that are symmetrically placed to the interface are indistinguishable by their resulting count rates. This will be discussed elsewhere. The noise level was strictly proportional to the square root of the counts per time channel. Attributable to quantum or shot noise it was not to be lessened, because of the limited light stability of the dye.

The time base was digitized at intervals of 10 ms. At this time resolution the transients were instantaneous. The number of three steps conformed with the expectation based on (a) the number of three reactive sites on the hexagon formed by the large subunits of CF_1 [1,18], and (b) the interpretation of our previous experiments with a large ensemble of labelled CF_1 [5] in the light of a theory of molecular stepper motors [7]. It is an important new result that the angular positions of the transitions between two sites were so shortlived. Within stochastic limits, the average persistence on levels P1, P2, and P3 was much longer than the transit time between them. It was compatible with the observed average turnover time of 85 ms for ATP hydrolysis by immobilized CF_1.

3.2. Transients of CF_1 labelled at subunits δ and ε

Transients of CF_1 labelled at subunits δ and ε are shown in Fig. 4A and B, respectively. In both cases the enzyme was hydrolyzing ATP. With the label on subunit δ we consistently (200 cases) observed a behavior with a high count rate at the beginning and a sudden drop to a bleached level that was

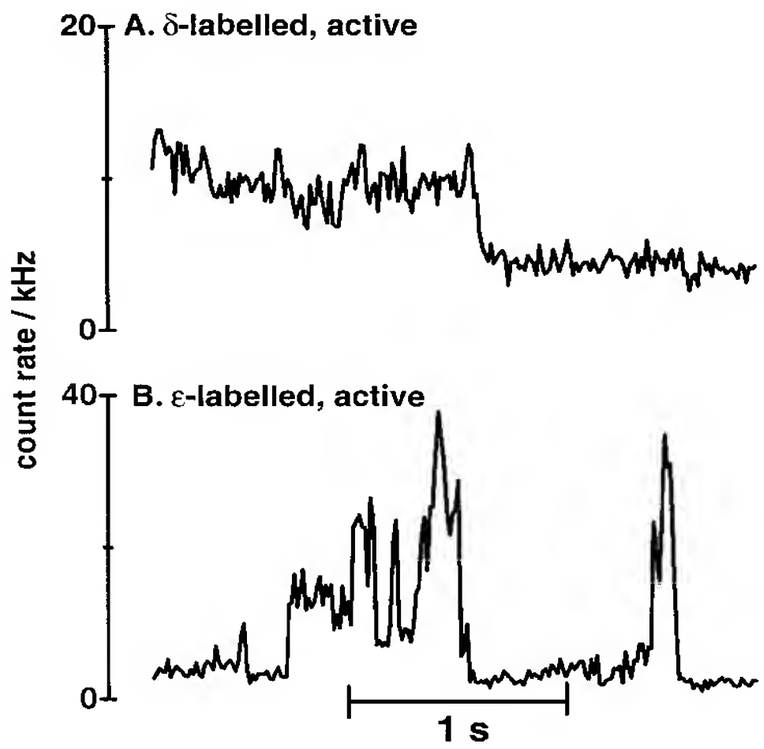

Fig. 4. Transients of fluorescence upon excitation of a single immobilized molecule of CF_1 with linearly, polarized light under ATP hydrolysis (ATP but no ADP added). TMR was covalently attached to either subunit δ (A), or ε (B). All other conditions were as described in Fig. 3. Note that the signal with TMR-labelled ε displays the same major characteristic of the signal recorded with active CF_1 which was labelled in γ. The signal with TMR-labelled δ resembles the signal obtained with γ-labelled but ADP-inhibited CF_1 (cf. Fig. 3A).

attributable to a non-rotating element (see also Fig. 3A). Contrastingly there were uprising count rates when the label was attached to subunit ε. Subunit ε did not reveal the regularity of stepping through three positions as subunit γ. Although the stochastic character of the stepped rotation hampers a direct comparison of the rotations of ε and γ, these data demonstrate that ε belongs to the rotor (with γ) and δ to the stator of the enzyme (with $(\alpha\beta)_3$) (see [21] for an up-to-date structural model). The same assignment has been inferred from the different effects on the ATPase activity of crosslinking of δ with $(\alpha\beta)_3$ [11] and of ε with γ [12,19], respectively.

Which reaction provides the major driving force for a rotational step is a key question to understand the driving mechanism. The hydrolysis of ATP is expected to proceed in the following sequence: binding of ATP, its sequestration ('tight binding'), the hydrolysis of sequestered ATP, and the release of ADP and P_i. Since our experiments were carried out under ATP saturation, the binding of ATP was not rate-limiting and certainly not responsible for the sudden steps. The hydrolysis of ATP by CF_1 is generally conceived as the inversion of ATP synthesis by F_OF_1, and the release of tightly bound ATP as the major energy requiring step [20]. When F_1 operates in the reverse direction the sequestration of (loosely) bound ATP may be the major driving step. It is conceivable that it pulls the DELSEED 'lever' at the 'loose' binding site (see [1]) inwardly towards the crank of subunit γ to click it round to the next angular position.

Acknowledgements: We gratefully acknowledge the technical assistance of Martina Roelevink. This work was supported by a grant of the Deutsche Forschungsgemeinschaft (SFB 171-B3), the Land Niedersachsen and the Fonds der Chemischen Industrie.

References

[1] Abrahams, J.P., Leslie, A.G.W., Lutter, R. and Walker, J.E. (1994) Nature 370, 621–628.
[2] Boyer, P.D. (1997) Annu. Rev. Biochem. 66, 717–749.
[3] Junge, W., Lill, H. and Engelbrecht, S. (1997) TIBS 22, 123–456.
[4] Duncan, T.M., Bulygin, V.V., Zhou, Y., Hutcheon, L.L. and Cross, R.L. (1995) Proc. Natl. Acad. Sci. USA 92, 10964–10968.
[5] Sabbert, D., Elgelbrecht, S. and Junge, W. (1996) Nature 381, 623–626.
[6] Noji, H., Yasuda, R., Yoshida, M. and Kinosita, K. (1997) Nature 386, 299–302.
[7] Sabbert, D. and Junge, W. (1997) Proc. Natl. Acad. Sci. USA 94, 2312–2317.
[8] Sabbert, D., Engelbrecht, S. and Junge, W. (1997) Proc. Natl. Acad. Sci. USA 94, 4401–4405.
[9] Moroney, J.V., Fullmer, C.S. and McCarty, R.E. (1984) J. Biol. Chem. 259, 7281–7285.
[10] Miki, J., Maeda, M., Mukohata, Y. and Futai, M. (1988) FEBS Lett. 232, 221–226.
[11] Lill, H., Hensel, F., Junge, W. and Engelbrecht, S. (1996) J. Biol. Chem. 271, 32737–32742.
[12] Schulenberg, B., Wellmer, F., Junge, W. and Engelbrecht, S. (1997) Eur. J. Biochem. 249, 134–141.
[13] Engelbrecht, S., Schürmann, K. and Junge, W. (1989) Eur. J. Biochem. 179, 117–122.
[14] Engelbrecht, S., Lill, H. and Junge, W. (1986) Eur. J. Biochem. 160, 635–643.
[15] Steinemann, D., Lill, H., Junge, W. and Engelbrecht, S. (1994) Biochim. Biophys. Acta 1187, 354–359.
[16] Elson, E. and Magde, D. (1974) Biopolymers 13, 1–27.
[17] Wennmalm, S., Edman, L. and Rigler, R. (1997) Proc. Natl. Acad. Sci. USA 94, 10641–10646.
[18] Weber, J., Wilke-Mounts, S. and Senior, A.E. (1994) J. Biol. Chem. 269, 20462–20467.
[19] Aggeler, R., Ogilvie, I. and Capaldi, R.A. (1997) J. Biol. Chem. 272, 16621–16656.
[20] Penefsky, H.S. (1985) J. Biol. Chem. 260, 13735–13741.
[21] Engelbrecht, S. and Junge, W. (1997) FEBS Lett. 414, 123–456.

Photochemistry and Photobiology, 2003, 77(4): 362–369

Single-molecule Fluorescence Lifetime and Anisotropy Measurements of the Red Fluorescent Protein, DsRed, in Solution¶

Benjamin Bowen[1] and Neal Woodbury*[2]

[1]Department of Chemical and Materials Engineering, Arizona State University, Tempe, AZ and
[2]Department of Chemistry and Biochemistry, Arizona State University, Tempe, AZ

Received 8 October 2002; accepted 12 January 2003

ABSTRACT

Fluorescence lifetime and anisotropy measurements were made on the red fluorescent protein (DsRed) from tropical coral of the *Discosoma* genus, both at single-molecule and bulk concentrations. As expected from previous work, the fluorescence lifetime of DsRed in solution is dependent on laser power, decreasing from an average fluorescence lifetime in the beam of about 3.3 ns at low power (3.5 ns if one extrapolates to zero power) to about 2.1 ns at 28 kW/cm^2. At the single-molecule level, exciting with 532 nm, 10 ps laser pulses at 80 MHz repetition rate, DsRed particles entering the laser beam initially have a lifetime of about 3.6 ns and convert to a form having a lifetime of about 3.0 ns with a quantum yield of photoconversion on the order of 10^{-3} (calculated in terms of photons per DsRed tetramer). The particles then undergo additional photoconversion with a quantum yield of roughly 10^{-5}, generating a form with an average lifetime of 1.6 ns. These results may be explained by rapid photoconversion of one DsRed monomer in a tetramer, which acts as an energy transfer sink, resulting in a lower quantum yield for photoconversion of subsequent monomers. Multiparameter correlation and selective averaging can be used to identify DsRed in a mixture of fluorophores, in part exploiting the fact that fluorescent lifetime of DsRed changes as a function of excitation intensity.

INTRODUCTION

Intrinsically fluorescent proteins such as those derived from green fluorescent protein (GFP) have been widely used as intracellular probes (1). The widespread use of GFP is attributed to its visible excitation and emission bands, mutability to create color-shifted variants and the ease with which GFP can be fused to other proteins and expressed in a variety of genetic backgrounds. More recently, another intrinsically fluorescent protein, red fluorescent protein (DsRed) from tropical coral of the *Discosoma* genus, has been discovered and represents an alternative to GFP (2–4). Like some GFP variants, DsRed has a high quantum yield of fluorescence (0.7) and a high extinction coefficient (75 000 M^{-1} cm^{-1}). In addition, the emission from DsRed is substantially redshifted, and it is more resistant to photobleaching than known GFP variants (5,6). The low rate of photobleaching and redshifted emission should facilitate single-molecule measurements to be made in living cells because this allows longer signal averaging while using excitation and detection conditions that give rise to less autofluorescence.

Widespread use of DsRed as a fluorescent reporter has prompted investigation into the biochemical and photophysical properties of the protein. It has been shown that DsRed forms a stable tetramer at nanomolar concentrations (5–8). The absorbance spectrum peaks at 558 nm and the fluorescence spectrum at 583 nm (5). The fluorescence lifetime of the native complex has been measured as 3.6 ns (6). Interestingly, on continued illumination, photoconversion occurs from this spectral form to redshifted form emitting at 595 nm and with a variable fluorescence decay time between 1.5 and 2.7 ns (9). The chemical nature of this photoconverted form is not known. Recent single-molecule measurements have been performed that follow the time course of the photochemical conversion process, in terms of both the shift in the emission spectrum and of the fluorescence lifetime. In some cases, the process appears to occur in steps, possibly because of successive conversion of the monomers within the tetramer (9).

Another interesting aspect of DsRed photochemistry is that the anisotropy in bulk solution has been shown to be about 0.23, independent of the solvent viscosity (6,10). From the crystal structure of the DsRed tetramer, the alignment of the chromophores indicates that energy transfer may occur on time scales roughly an order of magnitude faster than the excited state lifetime (10). Rapid energy transfer would depolarize the fluorescence, resulting in a low anisotropy for DsRed tetramers, although the rotation time in solution of the complex is much longer than the fluorescence lifetime (6). Thus, energy transfer between monomers in the tetramer is apparently an important aspect of DsRed photophysics.

In the measurements that follow, the photophysical and photochemical properties of DsRed are further investigated. Most of the measurements described are single-molecule fluorescence studies. Unlike previous single-molecule work on DsRed, these measurements are performed on molecules free in solution, thus avoiding potential surface effects. To obtain a reasonable signal-to-noise ratio during the brief transit of the molecules through the

¶Posted on the website on 1 February 2003.
*To whom correspondence should be addressed at: Department of Chemistry and Biochemistry, Arizona State University, Tempe, AZ 85287, USA. Fax: 480-965-2747; e-mail: nwoodbury@asu.edu
Abbreviations: DsRed, red fluorescent protein; GFP, green fluorescent protein; IPD, inverse photon density; MLE, maximum-likelihood estimator; R-6G, rhodamine-6G; TCSPC, time-correlated single-photon counting.
© 2003 American Society for Photobiology 0031-8655/01 $5.00+0.00

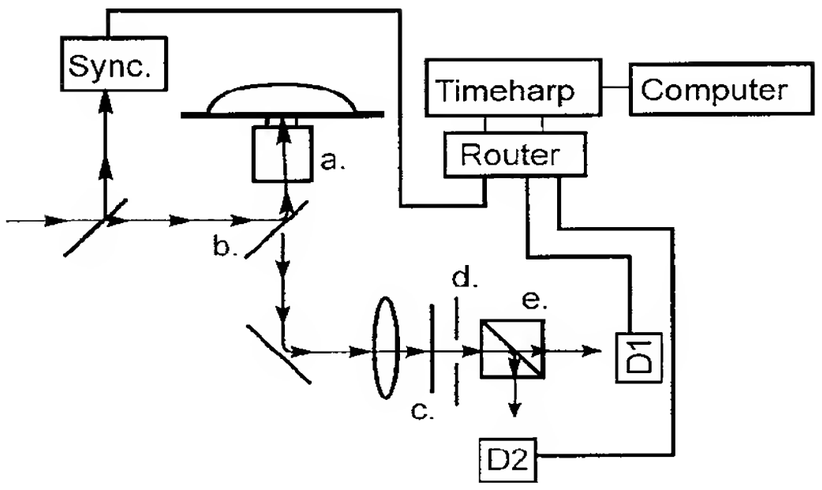

Figure 1. Schematic of the microscope showing the microscope objective (a), dichroic mirror (b), emission filter (c), pinhole (d) and broadband polarizing beam splitter (e). The synchronization detector and electronics (Sync.) are used to generate a synchronization signal for the time-correlated photon-counting board (Timeharp). The router multiplexes the input signals from different detectors (D1 and D2) so that they are stored in different time ranges (time relative to the synchronization pulse in nanoseconds).

laser beam, selective averaging methods are used, which allow one to correlate processes such as photoconversion with time spent in the beam and fluorescence lifetime while maintaining knowledge of the distributions of the parameters involved. Finally, the ability to distinguish between DsRed and other fluorophores in a mixture using the property of photoconversion as a distinguishing characteristic for DsRed is explored.

MATERIALS AND METHODS

Instrumentation. Single-molecule spectroscopy was performed using a home-built, confocal microscope system and a high-frequency, mode-locked laser as the excitation source to facilitate time-correlated measurements of fluorescence lifetime. A schematic of this system is shown in Fig. 1. The excitation laser was a frequency-doubled, pulse-compressed, mode-locked Nd:YAG laser (532 nm, 10 ps pulse duration) with a repetition rate of 82 MHz. All fitting of fluorescence decays was performed by convolution of a single-exponential decay with the instrument response function of the system. The 82 MHz repetition rate gives a small degree of "wrap-around" fluorescence, but the contribution of photons that are detected more than 12 ns after the excitation pulse does not change the fluorescence lifetime of the samples studied in this work. The error in lifetime calculations is primarily due to the poor signal-to-noise ratio inherent in single-molecule fluorescence measurements. To ensure proper beam quality and polarization, the laser light was passed through a single-mode, polarization-preserving glass fiber (F-SPA; Newport, Irvine, CA) and a polarizing beam splitter (05BC15PH.3; Newport). The laser light was delivered to an inverted, confocal microscope and reflected up toward the microscope objective with a dichroic mirror (Q570LP; Omega Optical, Brattleboro, VT). The sample, a 50 microliter droplet, was spread onto a glass coverslip (22 × 50 mm, no. 1.5; VWR, West Chester, PA). The same objective (100× PlanApo 1.4NA; Olympus, Tokyo, Japan) used to focus the laser also collected the fluorescence. The collected fluorescence passed through the dichroic mirror and was focused onto a 100 μm diameter pinhole (910-PH100; Newport). The fluorescence was then split by a polarizing beam splitter (05FC16PB.3; Newport), sending photons polarized parallel to the laser to one detector (SPCM-AQR-12; Perkin–Elmer, Fremont, CA) and photons polarized perpendicular to the laser to a second detector. To reduce Raleigh and Raman scattering, the fluorescence was passed through a custom emission filter (Omega Optical). The filter specifically blocks 532 nm light and the water Raman scattering from 532 nm light.

The signal from the detectors and a synchronization signal from each laser pulse were sent into a multiplexer (router), which was designed and built locally. The multiplexer sends a start signal and a stop signal into a Timeharp time-correlated single–photon counting (TCSPC) card (Picoquant, Berlin, Germany). The multiplexer separates the signals from the two detectors in regions of time defined by the repetition rate of the laser such that signal of each detector occupies a different 12 ns region of time recorded by the Timeharp.

Sample preparation. Single colonies of DH5α *Escherichia coli* cells expressing DsRed from the plasmid pDSRED (Clontech, Palo Alto, CA) were used to inoculate twenty 3 mL tubes of L-Broth media (by weight: 1% bactotryptone and 1% NaCl and 0.5% Bacto yeast extract) and were grown for 48 h at 37°C with shaking. Eighteen of the 20 tubes turned red due to DsRed expression and subsequent assembly and chromophore formation. The media from these tubes, 54 mL in total, were spun in an SA 600 rotor (Sorvall) at 8000 rpm for 8 min at 20°C. The cells were washed with buffer (10 m*M* Tris–HCl, pH 7.4, 100 m*M* NaCl, 1 m*M* $MgCl_2$, 10 m*M* dithiothreitol), respun and suspended in 10 mL of the same buffer. The cells were then broken by passing them through a French pressure cell at pressures greater than 20 000 psi. The effluent from the pressure cell was spun at 8000 rpm for 8 min in SA 600 rotor. The supernatant was collected and respun at 15 000 rpm for 15 min in SA 600 rotor, and the supernatant of this spin was collected. To remove permanent aggregates, the product was filtered twice using a 100 kDa, nominal molecular weight cutoff membrane filter (Centricon) spun at 2500 rpm in SA 600 rotor for 30 min. Aliquots of this sample were stored at −80°C until use. The sample was diluted for single-molecule measurements in 10 m*M* Tris, 1 m*M* ethylenediaminetetra-acetic acid buffer to approximately 0.1 n*M*. Higher concentrations were used for measuring bulk properties of the protein.

Note that in these samples, most of the DsRed do not pass through the 100 kDa cutoff membrane, as would be expected for tetramer DsRed complexes. This filtration was performed to remove the very large complexes from the mixture (anything significantly larger than a tetramer is very unlikely to pass through), although both the single-molecule (analyzed in terms of fluorescence correlation spectroscopy and diffusion times) and dynamic light scattering measurements indicate that larger complexes reform dynamically after filtration (data not shown).

RESULTS

The power dependence of the ensemble-averaged fluorescence lifetime

For measuring ensemble-averaged fluorescence lifetime as a function of laser intensity, 200 n*M* DsRed was used. The isotropic lifetime of the excited state, as measured by TCSPC and fit with single-exponential least squares curve fitting, is strongly dependent on the intensity of the 532 nm excitation light, changing from 3.3 ns at the lowest power measured to about 2.1 ns at 28 kW/cm^2 (Fig. 2). The focal path has a diameter of 0.8 μm; consequently, very high light intensities are achieved with relatively low laser powers. Extrapolating to zero power gives a lifetime of 3.5 ns, in good agreement with the previously measured value of 3.6 ns at low power (6). The steady-state anisotropy for the ensemble-averaged measurements remained 0.22, independent of laser intensity (data not shown).

Distinguishing between single-particle fluorescence and background using multiparameter measurements

The remaining measurements were performed at the single-molecule (single-particle) level. A technical issue in single-molecule spectroscopy is distinguishing between photons generated by fluorescence from individual particles in the beam and those from other sources. This is perhaps most critical in experiments such as these, where diffusion of particles in and out of the beam plays a major role in the dynamics. Typically, the average amount of fluorescence that can be detected from a single dye molecule when it diffuses through the probe volume under saturating excitation, using the instrument described here, is between 30 and 50 photons, although this depends on the fluorescence yield as well as on the dark-state lifetime and yield. In addition to the fluorescence from single particles, there are background signals from Raman scattering by the solvent and electronic noise in the detection electronics.

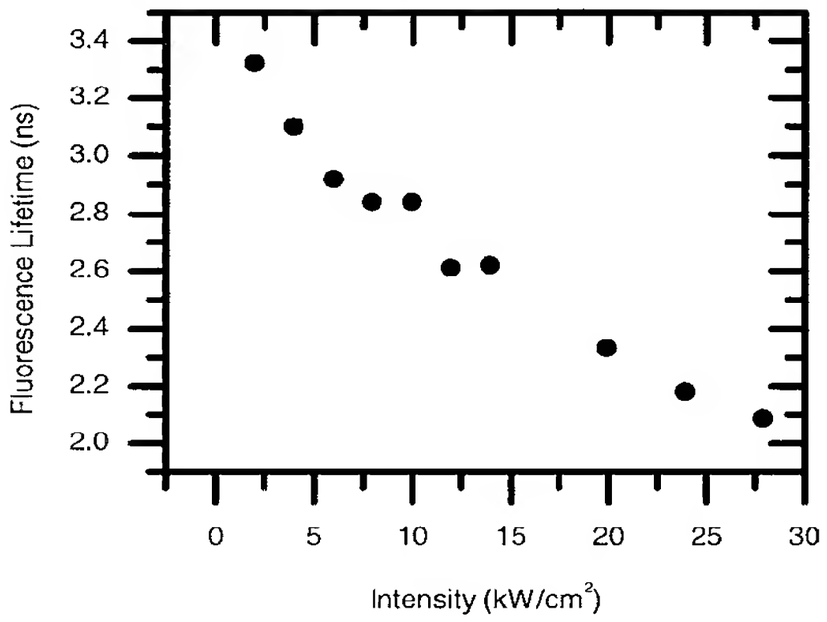

Figure 2. The fluorescence lifetime measured in bulk samples depends on the intensity of light used for excitation. Fluorescence lifetimes were measured as described in the text for 70 n*M* DsRed on the same microscope described for the single-molecule work.

The multidimensional nature of the data collection procedure used in this work makes it possible to resolve the single-molecule or single-particle fluorescence from the background signal most of the time by sorting the photons or photon bursts based on their measured characteristics. In these measurements, three types of information were recorded for each photon: the time of arrival in the lab frame, the time of arrival relative to the excitation laser pulse (*i.e.* the lifetime of the excited state that gave rise to the photon) and the polarization of the photon.

The most obvious discriminating characteristic between background fluorescence and fluorescence from a single fluorophore in the probe volume is the number of photons detected within a certain amount of time (in the lab time frame). This can be characterized by the average elapsed time between photons (the inverse photon density [IPD]). Photons making up the background signal will have more time between them than photons making up the single-molecule events. Consequently, the IPD for photons in the background will be larger than for photons that derive from single-molecule events.

The IPD for each detected photon was calculated by determining the average difference between the arrival time of a given photon and the arrival times of the nine photons closest to it in time. For the level of background and burst sizes in these data, 10 photons were sufficient to give a sharp change in density when a molecule was in the beam and were large enough so that background photons did not give a density high enough to be considered a single-molecule burst.

$$\mathrm{IPD} = \left(\sum_{i=1}^{10} |T_i - T_0| \right) / 10 \qquad (1)$$

where T_0 is the arrival time of the photon under consideration, and T_i is the arrival time of the nine closest photons in time.

The distribution of IPD is given in Fig. 3e. There are two clear populations of photons defined by this distribution. Most of the photons observed have a high inverse density (a long time between photons) on the order of 0.5 ms. A smaller population of photons has a low inverse density (a short time between photons), mostly less than 100 μs. By determining the average values of other measurable parameters for photons as a function of IPD, it is possible to tell which IPD region contains the single-molecule fluorescence signals

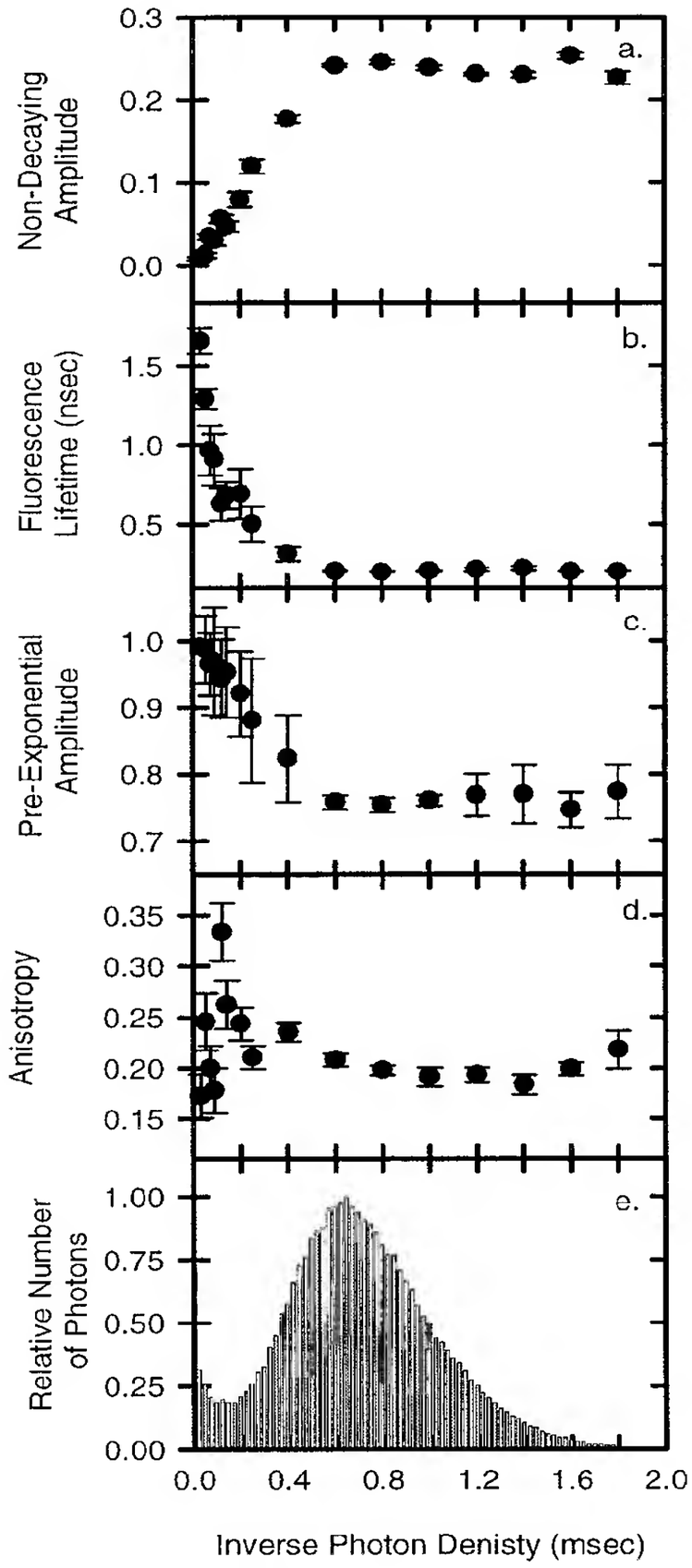

Figure 3. Selectively averaged fluorescence parameters are shown as a function of the IPD (all photons within a narrow IPD range are used to determine each parameter shown in panels a–d). The IPD is the average amount of time elapsed between detected photons. An IPD of greater than 0.1 ms was used as the threshold for single-molecule events in later analyses. As a function of the IPD, the amount of uncorrelated signal (the constant term in a fit of the fluorescence decay) (a), exponential fluorescence decay lifetime (b), pre-exponential amplitude of fluorescence decay component from the fit (c), anisotropy (d) and relative number of photons detected (e) are shown.

of interest and in this way reject most of the background signal. To do this, the value of a particular parameter is determined for all photons having a particular range of IPD values. The fluorescence anisotropy, R, is calculated according to the equation

$$R = (GI_{\parallel} - I_{\perp})/(GI_{\parallel} + 2I_{\perp}) \qquad (2)$$

where G is a correction factor for balancing the parallel and perpendicular channel detection efficiencies, $I_{\parallel}$ is the number of photons having a polarity parallel to the laser and $I_{\perp}$ is the number of photons having a polarity perpendicular to the laser. The result is shown in Fig. 3d.

It is also possible to measure the arrival time of each photon relative to the mode-locked laser pulse and for a particular IPD range and to determine the average lifetime of the excited state that gives rise to those photons. Figure 3a,c shows the nondecaying amplitude, lifetime and pre-exponential amplitude of a least squares curve fit of the isotropic fluorescence decay (that is, the sum of the parallel and twice the perpendicular components of the fluorescence decay) to the equation

$$F(t) = Ae^{-t/\tau} + B \quad (3)$$

where F(t) is the number of detected photons at time t measured relative to the laser pulse, A is the pre-exponential amplitude, τ is the decay time constant and B is the constant (nondecaying) term accounting, in these data, for photons not correlated with the laser pulse.

Photons due to Raman scattering should have a high fluorescence anisotropy and arrive within the laser pulse. Background signals caused by electronic noise are not temporally correlated with the laser pulse and should have a zero anisotropy. Looking first at the fluorescence lifetime as a function of IPD (Fig. 3b), it is clear that the dominant fluorescence lifetime becomes very short for the photons in the main (near 0.6 ms) region of the inverse photon distribution. This is consistent with a fast component in this part of the IPD curve that arises from Raman scattering. The same region of the curve also shows a large amplitude for the constant term in the fit of the isotropic fluorescence decay (Fig. 3a). This is consistent with a fraction of the photons with this inverse density arising from electronic noise that is not correlated with the mode-locked laser pulse. Thus, in the broad region of high IPD centered around 0.6 ms, there appears to be a mixture of photons due to Raman scattering and electronic noise. For this reason, the average anisotropy value observed for this part of the distribution is intermediate between the high value expected for scattering and the zero value expected for signal due to uncorrelated electronic noise.

The photons with inverse densities of less than 100 μs have much longer fluorescence lifetimes on average (Fig. 3b), as would be expected for the DsRed particles (9). In addition, the value of the constant term in the fluorescence decay fit is almost zero (very little uncorrelated electronic noise at this IPD). The anisotropy for IPD values less than 100 μs varies around 0.2. Although this is not very different from the anisotropy of the noise, it is also about what is expected for the anisotropy of DsRed (6,10). Although fluorescence correlation spectroscopy results obtained from this sample can be explained in terms of a single size of diffusing particles (data not shown), the variation in anisotropy between 0 and 300 μs IPD may be due to heterogeneity in DsRed particle size and composition. Generally, the greater the number of energetically equivalent DsRed molecules in the aggregate the lower the fluorescence anisotropy is likely to be because the energy will equilibrate between many different monomers with different transition dipole orientations. Larger aggregates, or aggregates that lack a monomer that has undergone photoconversion to a short fluorescence lifetime form, would be likely to give more photons per unit time and thus lower IPD. Thus, one might predict that within the low-IPD population, the lowest IPD should be associated with the lowest anisotropies.

By analyzing the IPD as a function of the other measured parameters as described above, it is possible to discriminate between the single-particle fluorescence signals and much of the background noise using an IPD threshold. An IPD threshold of 0.1 ms was used in all the studies reported here. The low–inverse-density photons thus selected are then reassembled into discrete single-molecule events. This is performed by chronologically scanning the remaining photons in the data set and considering any photon with no photon before it for at least 2 ms to be the start of an event and any photon with no photon for at least 2 ms after it to be the end of an event. All single-particle bursts identified in this way that contained at least 40 photons were included in the analyses described below. The use of these parameters for single-molecule event identification is not new (11); however, they have not been applied to the analysis of DsRed.

Monitoring the photochemical conversion of DsRed at the single-molecule level in solution

Previous work has shown that as DsRed is exposed to light, it undergoes a photochemical conversion (9,10,12). To follow this process in single molecules in solution, photons in the bursts were binned according to the time that elapsed from the initiation of the single-particle fluorescence burst. Then, the photons from all events with a particular bin time were averaged together, giving a representation of the fluorescence as a function of time after a single particle entered the beam. This is similar to performing an average measurement in a bulk experiment as a function of time after the onset of illumination, except that the experiment can be performed continuously without having to synchronize the opening of the shutter with the data collection, and the distributions of the measured parameters and their average are available. Figure 4 shows the result of such an experiment and analysis monitoring the average fluorescence lifetime as a function of time in the beam. These data were collected at a series of different laser intensities from 4 to 40 kW/cm^2 (using a 80 MHz mode-locked, doubled Nd:YAG laser at 532 nm for excitation). At the lowest power (bottom panel, Fig. 4), the lifetime is initially near 3.6 ns, as has been measured at low laser power in bulk solution. This rapidly decreases to about 3.0 ns over a few hundred microseconds. At higher powers (middle and upper panels, Fig. 4), the lifetime is shorter to begin with and then drops with time. At the highest power, the fluorescence lifetime is initially about 2.2 ns and decreases with time to about 1.6 ns. The drop in fluorescent lifetime of DsRed as a function of time in the beam is consistent with previous single-molecule measurements performed on immobilized samples and thus likely represents the photoconversion process (9).

Detecting DsRed particles in a mixture using selective averaging and multiparameter correlation

One long-range goal of this work is to be able to better follow DsRed in complex mixtures, such as cells. As shown above, selective averaging of collected photons can be used to distinguish between signal and background or to correlate one parameter, such as fluorescence lifetime, with another, such as time spent in the beam, in order to determine the time dependence of photochemistry. To explore the uses of selective averaging and multiparameter correlation in order to distinguish DsRed from other fluorescent molecules, mixtures of DsRed and rhodamine-6G (R-6G) dye molecules, both of which at low power have similar fluorescence lifetimes, were used as a model system.

To selectively average fluorescent burst parameters and to perform multiparameter correlations, it is necessary to determine the values of these parameters for individual fluorescent bursts.

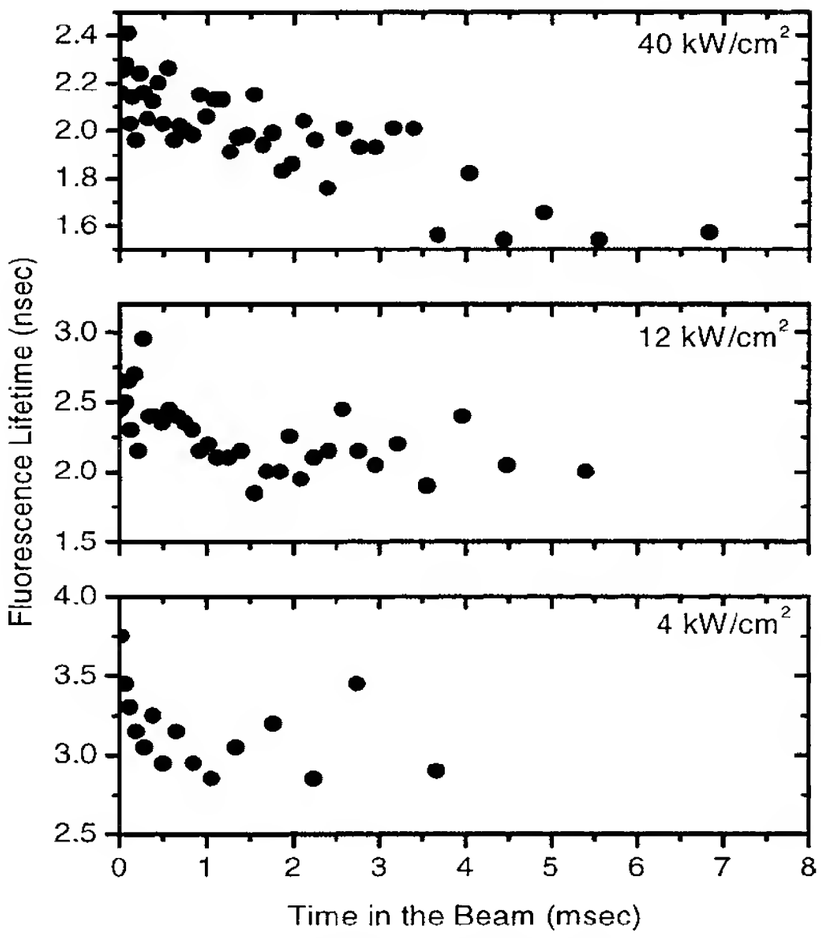

Figure 4. Photons from individual single-particle bursts are collected into groups as a function of time relative to the start of the event. For each group of 1000 photons (the first 1000, second 1000, *etc.*), the fluorescence decay lifetime is calculated (y-axis) and plotted as a function of the average arrival time of the photons in that group relative to the point the DsRed particle entered the beam (x-axis). At different excitation intensities, the rate of photoconversion varies. While in the beam, the particles convert into a form having a shorter lifetime. For each plot, the excitation intensity used is shown in the top right corner of the panel.

The estimation of single-molecule fluorescence lifetimes of individual bursts was performed using the maximum-likelihood estimator (MLE) optimization technique. MLE is an exceptionally good, curve-fitting technique for analyzing small numbers of photons (13). The lifetimes are calculated from the isotropic decay (calculated as the sum of the time-correlated photons in the vertically polarized channel plus twice the photons in the horizontally polarized channel) to avoid polarization distortion of the decay times. The steady-state anisotropy is calculated for each burst according to Eq. 3. The transit time through the beam for a particular single-particle event is the difference in arrival times between the last and the first photon in a burst. The average IPD is the arithmetic average of the IPD for the individual photons in the burst.

Figure 5 shows the results of a selective averaging experiment in which the average values of the anisotropy, burst duration and IPD (milliseconds between photons) are shown for all bursts with a particular fluorescence lifetime (panels a–c). Figure 5d shows a simple histogram of the numbers of bursts with different fluorescence lifetimes. For the data shown here, a high excitation power was used that had the effect of shifting the average fluorescence lifetime of the DsRed bursts to shorter times, whereas having no effect on the R-6G lifetime. Two peaks in the lifetime histogram are observed, near 2 and 4 ns. Looking at the selectively averaged parameters (Fig. 5a–c), the one most obviously correlated with the two lifetime populations is the anisotropy. R-6G has an anisotropy near zero, whereas, as discussed above, the anisotropy of the DsRed on average is near 0.23 (6,10).

Direct correlation between the lifetime and anisotropy information for individual bursts allows yet better separation of the

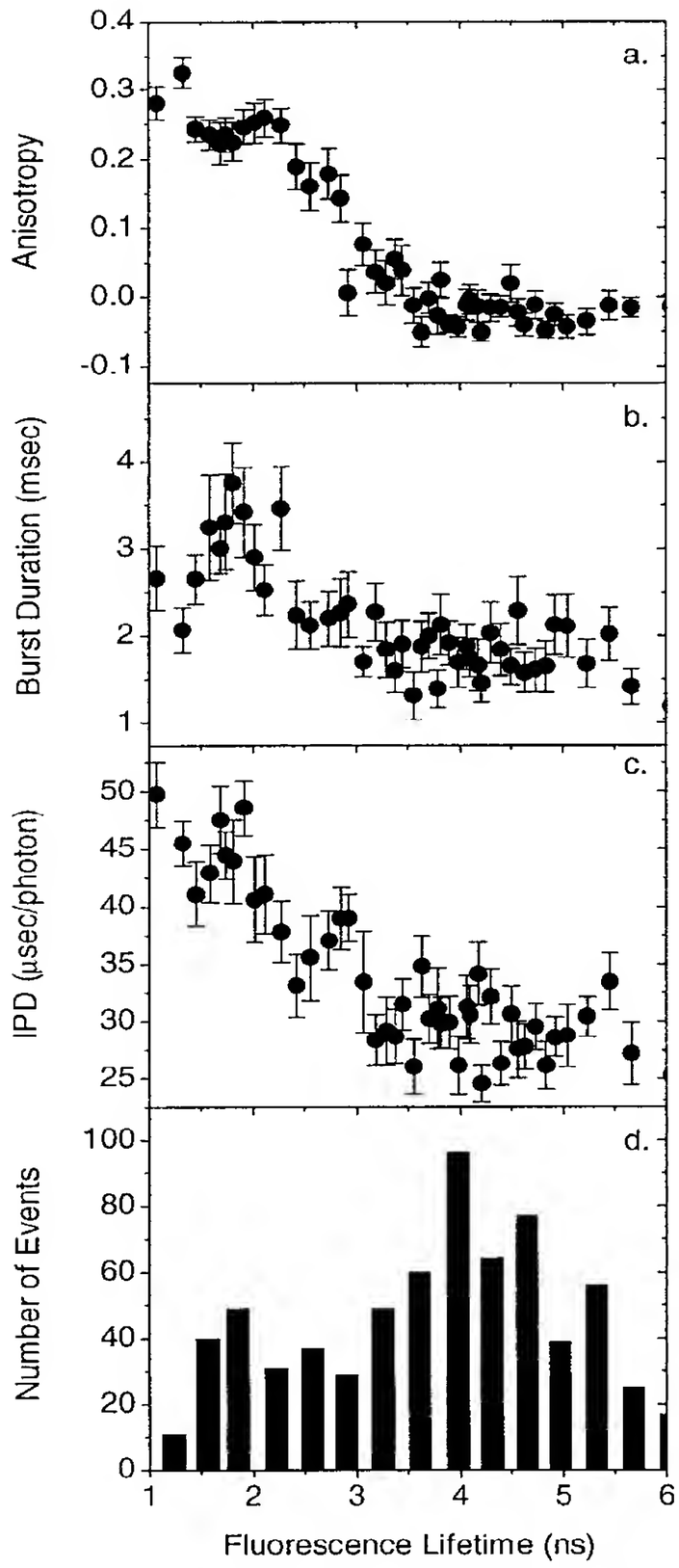

Figure 5. The average anisotropy (a), burst duration (b) and IPD (c) are shown as a function of fluorescence decay lifetime for a mixture of DsRed particles and R-6G. The value of each average parameter was determined by summing the photons from all events having the fluorescence decay lifetime shown on the x-axis. Also shown is the number of events recorded as a function of fluorescence lifetime (d).

two populations of fluorophores in the mixture. In Fig. 6, the anisotropy and the fluorescence lifetime of each burst are used to generate a two-dimensional contour plot, with the height of the contour representing the number of bursts with a particular lifetime and anisotropy. The first two panels show the result of separate two-dimensional correlations between anisotropy and lifetime for DsRed and R-6G. The final panel shows the mixture. When both parameters are simultaneously taken into account, the bursts can be cleanly separated into the two populations with almost no overlap.

DISCUSSION

Applying selective averaging to single-molecule spectroscopy

In general, there are at least two ways to use information from single-molecule fluorescence studies. Perhaps, the most obvious is

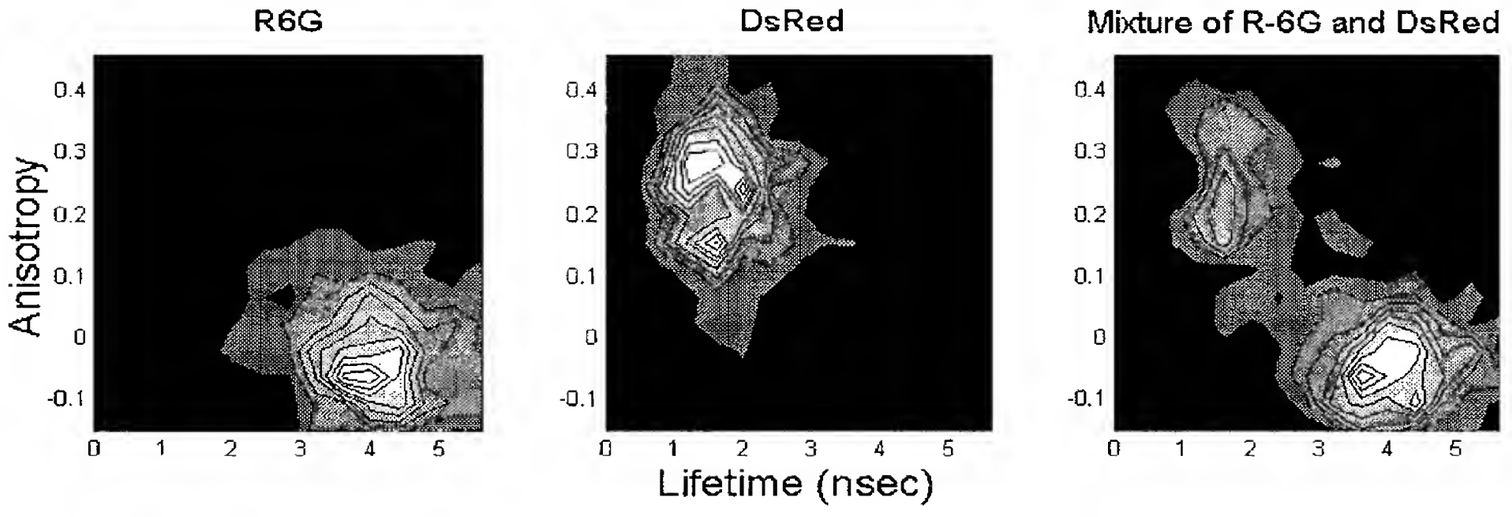

Figure 6. Multiparameter contour plots of the number of events with a particular anisotropy and fluorescence lifetime for R-6G, DsRed and a mixture of the two. The two-component histograms allow better resolution of the components in the mixture.

to follow the dynamics of individual molecules for periods of time, studying dynamics directly. Examples include the movement of molecular motors or following the individual steps of a multistep reaction such as RNA polymerization or protein folding (14–18). Although very powerful, such methods are limited at the single-molecule level in terms of signal to noise, time resolution (it is difficult to collect more than about 100 photons/ms from a single molecule) and usually involve subjective decisions about the molecules that should be used to make mechanistic conclusions.

There is another broad set of analytical methods that can be applied to single-molecule data. This includes various forms of single-molecule correlation techniques and other selective averaging techniques. These types of analyses take advantage of the fact that when fluorescence data are collected at the single-molecule level, it is left to the investigator to decide what parameters to average or correlate and what parameters to consider independently for each molecule in the population. For example, one can determine the average anisotropy of all the bursts that have a particular fluorescence lifetime or determine the fluorescence amplitude as a function of time for only those bursts that have a certain anisotropy. Single-molecule fluorescence correlation spectroscopy is another common example of this type of approach. Such analyses reveal correlations between observable parameters that are lost in an ensemble average. Although any averaging results in some loss of information, selective averaging can play a very important role in error reduction, particularly in cases where the amount of signal from each individual molecule is low or where one wants to look for mechanistically important trends that apply to a subpopulation of molecules or states of molecules in a mixture.

Selective averaging and multiparameter correlation techniques have been used in several different ways in this work. First, selective averaging of certain fluorescent properties (lifetime, anisotropy, *etc.*) was performed as a function of IPD. In this way, it was possible to objectively determine which photon densities corresponded to single-particle fluorescence signals versus background scattering and electronic noise (see Results). Photons were then selected for further analysis based on this criterion. The second example involved generating the time dependence of the photoconversion process using events that occurred at random intervals due to diffusion through the laser beam. By determining when each burst initiates and thus when each molecule enters the excitation volume, it is possible to line up all the events in time and look for the time-dependent processes that occur on average. The final example involved correlating multiple parameters from individual bursts with one another to determine the average properties of the individual subpopulations within a mixture, in this case a mixture of DsRed and the dye, R-6G. The results from the second and third examples will be discussed in more detail below.

Photoconversion of DsRed particles in solution

The fluorescence lifetime of DsRed in solution depends on the laser power used for excitation (Fig. 2). One might think that this could be because of energy transfer and singlet–singlet annihilation among closely spaced DsRed monomers (rapid energy transfer presumably accounts for the low anisotropy of the DsRed tetramer [6]), but previous work has shown that preillumination of DsRed samples also results in shorter fluorescence lifetimes (9). This clearly indicates that photoconversion of DsRed between two or more forms is involved, as concluded by others. Past measurements have shown that extended irradiation of DsRed results in an apparently irreversible conversion of the 583 nm fluorescing form with a 3.6 ns fluorescence decay time to a form that fluoresces with a peak at 594 nm and has a rather heterogeneous fluorescence decay time between about 1.5 and 2.7 ns (9). The heterogeneity of the final state has been shown by single-molecule spectroscopy. Immobilized DsRed particles that were followed individually during the photoconversion process arrived at different final fluorescent lifetimes (final in the sense that they preceded photobleaching of the particle) and sometimes showed intermediate lifetime steps during the photoconversion process (9).

Evidence for a multistep photoconversion process is also given in Fig. 4. In this case, the DsRed sample was free in solution. This has the disadvantage that it is more difficult to follow the dynamics of individual molecules because of rapid diffusion but the advantage that it avoids effect due to the interaction of the DsRed with a surface, which could itself generate lifetime heterogeneity. In addition, solution measurements provide a simple means of studying microsecond to millisecond photodynamics. For the data shown in Fig. 4, fluorescence was recorded as a function of time after particles entered the beam and monitored for as long as they remained in the beam (typically hundreds of microseconds to milliseconds). Under high levels of illumination (about 40 kW/cm^2, Fig. 4, top panel), one can see that within the time resolution of the measurement, photoconversion of the 3.6 ns, native DsRed molecule to a form with a lifetime of about 2.2 ns had already taken place (the earliest lifetimes measured were roughly 2.2 ns). Subsequently, a much slower photoconversion takes place over at least 5 ms, resulting in a 1.6 ns form. Thus, there are clearly at least two processes at work here. A higher-yield photoconversion step that results in an intermediate-lifetime species and then a lower-yield photoconversion resulting in an additional lifetime decrease. The initial photoconversion process can be seen more clearly at

low power. Using 4 kW/cm^2 (Fig. 4, bottom panel), one sees that the lifetime of DsRed starts at essentially the low-power fluorescence lifetime value (nearly 3.6 ns) and then decreases on a time scale of roughly a few hundred microseconds to about 3.0 ns.

It is possible to estimate the quantum yields of the fast and slow photoconversion steps from the data presented here. From the extinction coefficient of DsRed (75 000 M^{-1} cm^{-1} at 560 nm or about 38 000 M^{-1} cm^{-1} at 532 nm), one can calculate an absorbance cross section at 532 nm of about 1.4×10^{-16} cm^2 for a monomer or 5.7×10^{-16} cm^2 for a tetramer. If we take the initial photoconversion time at 4 kW/cm^2 intensity to be about 300 μs (Fig. 4, bottom panel), then this implies that about 6.8×10^{-16} J of light is absorbed by a tetramer during the initial photoconversion period, which corresponds to about 1.8×10^3 photons at 532 nm absorbed during this time. Thus, the quantum yield of the initial photoconversion in a tetramer is on the order of 10^{-3}. The subsequent photoconversion event(s) occurs on the millisecond or longer time scales at 3- to 10-fold higher light intensity, suggesting that the average quantum yield for subsequent photoconversion steps is one to two orders of magnitude less than that for the initial photoconversion process. (The estimation of the range of photoconversion efficiencies for later steps ignores any effect of the changing absorbance cross section of the tetramer during the photoconversion process. This could become significant especially after two or three of the molecules in the tetramer have undergone photoconversion.)

One possible explanation of the multistep photoconversion process is as follows. Initially, the DsRed tetramers consist only of 583 nm fluorescing monomers and possibly immature green forms, depending on the growth and isolation procedures used (5,19). Energy transfer between monomers assures that the energy is rapidly localized on a 583 nm fluorescing monomer, which has an excited state lifetime of 3.6 ns. This long-lived excited state is reactive and can undergo photoconversion with a quantum yield of nearly 10^{-3}. After photoconversion of the first monomer in the tetramer to the 595 nm fluorescing form, a tetramer is created in which subsequent excitation results in rapid energy transfer from the 583 nm fluorescent species to the photoconverted 595 nm fluorescent species. The 595 nm species has a shorter lifetime (perhaps about 1.5 ns), and thus the total fluorescence decay time consists of the energy transfer time plus the decay time of the photoconverted species, giving rise to a fluorescence decay for the tetramer that is intermediate between the 3.6 ns decay time of native DsRed and that of the pure photoconverted form. Because of this energy transfer to the photoconverted form, the excited states of the 583 nm fluorescent monomers are now shorter lived and thus less likely to undergo photoconversion themselves (there are also fewer of them to absorb light). Therefore, the rate of the photoconversion process for the remaining 583 nm fluorescing monomers is slower than for the initial monomer. As photoconversion slowly occurs and more and more of the 583 nm monomers are converted to monomers fluorescing at 595 nm, the overall fluorescence lifetime continues to decrease because more and more of the photons are directly absorbed by the photoconverted form, and thus the lifetime approaches that of the pure photoconverted DsRed tetramer. Of course, as the number of 583 nm fluorescing monomers decreases, the total amount of time that these monomers are likely to spend in the excited state becomes less, both because of a decreased absorbance cross section and because of the fact that there are a greater number of long-wavelength monomers to rapidly transfer energy to. The result is that the overall yield for continued photoconversion from the 583 nm (long fluorescence lifetime) to 595 nm (short fluorescence lifetime) form in the tetramer continues to decrease.

Using the photochemical and photophysical properties of DsRed to distinguish it from other fluorophores in solution

One of the obvious uses of DsRed is as an intracellular probe in the same sense that GFP is used widely for this purpose. It has been suggested that DsRed may have some advantages in this regard, other than simply providing a long-wavelength version of an intrinsically fluorescent protein. DsRed has a lower rate of photobleaching than GFP as well as a high extinction coefficient and large quantum yield of fluorescence (5,10). Some of its other photophysical properties may also prove useful in this regard. The fact that it undergoes photoconversion could be used as a tool in its identification. During a confocal scan of a cell, for example, setting the excitation power effectively sets the average fluorescence lifetime of DsRed. Thus, one could either set the lifetime to a value different from contaminating fluorophores or perform differential scans with low and then high power, looking for the part of the signal that changes lifetime between the scans. Of course, it is often the case for cell imaging that fluorescent proteins are expressed as fusion proteins. Under these conditions, aggregation to form the tetramer may not occur or the aggregation state may be different from what is observed for DsRed alone. However, there is nothing to suggest that the photoconversion event depends on the aggregation state (other than in terms of cross section as described above), and thus although the details of the power dependence of the fluorescence lifetime may change, the ability to tune the fluorescence lifetime with laser power should be qualitatively similar.

An example of setting the DsRed lifetime and performing measurements at the single-molecule level in mixtures is shown in Fig. 6. Here, two fluorophores (DsRed and the laser dye R-6G) with similar fluorescence lifetimes at low power were mixed in solution. By using a high-intensity laser beam to probe the system, it was possible to tune the fluorescence lifetime of DsRed away from that of R-6G, using the photoconversion process described above. The fluorescence lifetime and the anisotropy (that should also be different for these two molecules because of the size difference) were measured for each particle as it passed through the beam. By correlating these two parameters, it was straightforward to assign individual bursts as either DsRed or R-6G, with nearly complete confidence. In this case, the measurement of either anisotropy or fluorescence lifetime alone would allow event identification most of the time, but by combining the two properties, the two subpopulations become almost completely resolved. As shown in Fig. 5, both burst duration and IPD are also correlated with the change in lifetime, and thus correlations with these two parameters could have been used to further distinguish between the two subpopulations. The analytical methodology used for such multiparameter correlations has been worked out previously (20). As described above, this is a case where single-molecule detection techniques become extremely useful even when average information is the desired goal. By performing the measurements at the single-molecule level, it is possible to correlate parameters with one another and in this way sort fluorophores into subpopulations, facilitating the determination of average properties of multiple subpopulations within a larger

population. This is not easily done in most cases from ensemble-averaged measurements.

Acknowledgements—This research was supported by NSF grant MCB9817388 and MCB0131776 and a donation from Phase Laser Systems. The authors thank Johan Hofkens for providing data regarding the photoconversion of DsRed before its publication and for helpful discussions.

REFERENCES

1. M. Chalfie and S. Kain (eds.) (1998) *Green Fluorescent Protein: Properties, Applications, and Protocols*, pp. 121–268. John Wiley & Sons, New York.
2. Mizuno, H., A. Sawano, P. Eli, H. Hama and A. Miyawaki (2001) Red fluorescent protein from Discosoma as a fusion tag and a partner for fluorescence resonance energy transfer. *Biochemistry* **40**, 2502–2510.
3. Rodrigues, F., M. van Hemert, H. Y. Steensma, M. Corte-Real and C. Leao (2001) Red fluorescent protein (DsRed) as a reporter in Saccharomyces cerevisiae. *J. Bacteriol.* **183**, 3791–3794.
4. Bloemberg, G. V., A. H. M. Wijfjes, G. E. M. Lamers, N. Stuurman, and B. J. J. Lugtenberg (2000) Simultaneous imaging of Pseudomonas fluorescens WCS365 populations expressing three different autofluorescent proteins in the rhizosphere: new perspectives for studying microbial communities. *Mol. Plant-Microbe. Interact.* **13**, 1170–1176.
5. Baird, G. S., D. A. Zacharias and R. Y. Tsien (2000) Biochemistry, mutagenesis, and oligomerization of DsRed, a red fluorescent protein from coral. *Proc. Natl. Acad. Sci. USA.* **97**, 11984–11989.
6. Heikal, A. A., S. T. Hess, G. S. Baird, R. Y. Tsien and W. W. Webb (2000) Molecular spectroscopy and dynamics of intrinsically fluorescent proteins: coral red (dsRed) and yellow (Citrine). *Proc. Natl. Acad. Sci. USA.* **97**, 11996–12001.
7. Wall, M. A., M. Socolich and R. Ranganathan (2000) The structural basis for red fluorescence in the tetrameric GFP homolog DsRed. *Nat. Struct. Biol.* **7**, 1133–1138.
8. Yarbrough, D., R. M. Wachter, K. Kallio, M. V. Matz and S. J. Remington (2001) Refined crystal structure of DsRed, a red fluorescent protein from coral, at 2.0-angstrom resolution. *Proc. Natl. Acad. Sci. USA.* **98**, 462–467.
9. Cotlet, M., J. Hofkens, S. Habuchi, G. Dirix, M. Van Guyse, J. Michiels, J. Vanderleyden and F. C. De Schryver (2001) Identification of different emitting species in the red fluorescent protein DsRed by means of ensemble and single-molecule spectroscopy. *Proc. Natl. Acad. Sci. USA.* **98**, 14398–14403.
10. Lounis, B., J. Deich, F. I. Rosell, S. G. Boxer and W. E. Moerner (2001) Photophysics of DsRed, a red fluorescent protein, from the ensemble to the single-molecule level. *J. Phys. Chem. B* **105**, 5048–5054.
11. Eggeling, C., J. R. Fries, L. Brand, R. Gunther and C. A. M. Seidel (1998) Monitoring conformational dynamics of a single molecule by selective fluorescence spectroscopy. *Proc. Natl. Acad. Sci. USA.* **95**, 1556–1561.
12. Malvezzi-Campeggi, F., M. Janhz, K. G. Heinze, P. Dittrich and P. Schwille (2001) Light-induced flickering of DsRed provides evidence for distinct and interconvertible fluorescent states. *Biophys. J.* **81**, 1776–1785.
13. Maus, M., M. Cotlet, J. Hofkens, T. Gensch, F. C. De Schryver, J. Schaffer and C. A. M. Seidel (2001) An experimental comparison of the maximum likelihood estimation and nonlinear least squares fluorescence lifetime analysis of single molecules. *Anal. Chem.* **73**, 2078–2086.
14. Borsch, M., P. Turina, C. Eggeling, J. R. Fries, C. A. M. Seidel, A. Labahn and P. Graber (1998) Conformational changes of the H+-ATPase from Escherichia coli upon nucleotide binding detected by single molecule fluorescence. *FEBS Lett.* **437**, 251–254.
15. Zhuang, X. W., L. E. Bartley, H. P. Babcock, R. Russell, T. J. Ha, D. Herschlag and S. Chu (2000) A single-molecule study of RNA catalysis and folding. *Science* **288**, 2048–2051.
16. Deniz, A. A., T. A. Laurence, G. S. Beligere, M. Dahan, A. B. Martin, D. S. Chemla, P. E. Dawson, P. G. Schultz and S. Weiss (2000) Single-molecule protein folding: diffusion fluorescence resonance energy transfer studies of the denaturation of chymotrypsin inhibitor 2. *Proc. Natl. Acad. Sci. USA.* **97**, 5179–5184.
17. Ha, T. J., A. Y. Ting, J. Liang, W. B. Caldwell, A. A. Deniz, D. S. Chemla, P. G. Schultz and S. Weiss (1999) Single-molecule fluorescence spectroscopy of enzyme conformational dynamics and cleavage mechanism. *Proc. Natl. Acad. Sci. USA.* **96**, 893–898.
18. Zhuang, X. W., T. Ha, H. D. Kim, T. Centner, S. Labeit and S. Chu (2000) Fluorescence quenching: a tool for single-molecule protein-folding study. *Proc. Natl. Acad. Sci. USA.* **97**, 14241–14244.
19. Garcia-Parajo, M. F., M. Koopman, E. M. H. P. van Dijk, V. Subramaniam and N. F. van Hulst (2001) The nature of fluorescence emission in the red fluorescent protein DsRed, revealed by single-molecule detection. *Proc. Natl. Acad. Sci. USA.* **98**, 14392–14397.
20. Eggeling, C., S. Berger, L. Brand, J. R. Fries, J. Schaffer, A. Volkmer and C. A. M. Seidel (2001) Data registration and selective single-molecule analysis using multiparameter fluorescence detection. *J. Biotechnol.* **86**, 163–180.

A high-speed atomic force microscope for studying biological macromolecules

Toshio Ando*†, Noriyuki Kodera*, Eisuke Takai*, Daisuke Maruyama*, Kiwamu Saito*, and Akitoshi Toda‡

*Department of Physics, Faculty of Science, Kanazawa University, Kakuma-machi, Kanazawa 920-1192, Japan; and ‡Olympus Co., 2951 Ishikawa-machi, Hachiohji, Tokyo 192-8507, Japan

Communicated by Shinya Inoué, Marine Biological Laboratory, Woods Hole, MA, July 31, 2001 (received for review May 21, 2001)

The atomic force microscope (AFM) is a powerful tool for imaging individual biological molecules attached to a substrate and placed in aqueous solution. At present, however, it is limited by the speed at which it can successively record highly resolved images. We sought to increase markedly the scan speed of the AFM, so that in the future it can be used to study the dynamic behavior of biomolecules. For this purpose, we have developed a high-speed scanner, free of resonant vibrations up to 60 kHz, small cantilevers with high resonance frequencies (450–650 kHz) and small spring constants (150–280 pN/nm), an objective-lens type of deflection detection device, and several electronic devices of wide bandwidth. Integration of these various devices has produced an AFM that can capture a 100 × 100 pixel² image within 80 ms and therefore can generate a movie consisting of many successive images (80-ms intervals) of a sample in aqueous solution. This is demonstrated by imaging myosin V molecules moving on mica (see http://www.s.kanazawa-u.ac.jp/phys/biophys/bmv_movie.htm).

One of the advantages of the atomic force microscope (AFM) (1) is its capacity to image individual biomolecules in, say, a buffered solution containing ions at physiological concentrations (2, 3). Such capacity suggests that the instrument can be used to record the dynamic behavior of such molecules. In practice, however, only very slow processes can be recorded (2, 4–6), because commercially available AFMs require minutes to form an acceptable image, and many interesting biological processes occur at much higher rates. To understand, and overcome, the factors that limit the scanning rate of an AFM, we begin by considering relations between the characteristics of the constituting components.

We consider only the "tapping mode" of AFM operation (Digital Instruments, Santa Barbara, CA). This is the mode suitable for imaging biological macromolecules, because vertical oscillation of the cantilever at (or near to) its resonance frequency reduces lateral forces between the tip and the sample (7). The oscillating tip briefly taps the surface at the bottom of each swing, resulting in a decrease in oscillation amplitude. During the x-y scan of the sample stage a feedback loop (see below) keeps this decrease (and hence the tapping force) constant; this is necessary for minimizing the deformation of soft samples. The error signal—the difference between a preset signal and the rms amplitude of the cantilever—is fed into a proportional-integral-differential (PID) feedback circuit. The PID output is amplified and then sent to the z-piezo actuator; this is repeated until the error signal returns to zero. For the three-dimentional movement of the sample stage to follow the sample topography accurately, the bandwidth of the feedback loop should be comparable to, or larger than, the frequency determined by the x-y scan velocity and the apparent width of the features on the surface. To increase the imaging bandwidth, all elements in the feedback loop have to be optimized. The first element in this loop is the cantilever. A high resonance frequency in liquid is required to generate a high tapping frequency; also required is a low spring constant, so as to minimize the tip-sample interaction force. These conflicting requirements can be met only with small cantilevers (8, 9). Every circuit in the feedback loop must have a wide bandwidth. The last element, the z-scanner, is a piezo actuator with a high resonance frequency, which in assembly must react very quickly without unwanted mechanical vibrations. Viani *et al.* (10, 11), using the tapping mode, have used small cantilevers with resonance frequencies ≈150 kHz to image DNA and GroEL–GroES complexes on mica, in liquid. Their frame rate was less than 1 s^{-1} because they used a conventional piezo-tube with a resonance frequency of ≈15 kHz in the z direction, together with feedback electronics of a limited bandwidth. Sulchek *et al.* (12), using a cantilever with an integrated zinc oxide piezo actuator (13), achieved an imaging bandwidth of 38 kHz and frame rate of ≈4/sec. However, their cantilever was too stiff to image soft samples. In the AFM assembly described below we have tried to optimize each element for its use in imaging samples in solution, using fast tapping operation, and an objective lens type of deflection detection device suitable for small cantilevers. Assembly of these selected components results in an imaging bandwidth of ≈60 kHz (fastest among the high-speed AFMs that use the tapping mode and are suitable for examining soft samples in liquid). Combination of this high speed with zooming-in capability (reduction of the scan area to 240 × 240 nm^2) allows viewing of liquid samples of proteins on mica at a rate of 12.5 s^{-1}.

Test Sample, Components, and Imaging

Sample Preparation. For test purposes, myosin V was extracted from chick brains and purified as described (14). Myosin V stored at 0°C in buffer A (25 mM KCl/25 mM Imidazole, pH 7.6/2 mM $MgCl_2$/1 mM EGTA/0.2 mM DTT) was diluted to 7 nM with buffer A. A drop (≈2 μl) of myosin V solution was placed on freshly cleaved mica (1 mm in diameter) for 3 min, rinsed with buffer A to remove unattached myosin V, and then imaged in 2 mM ATP plus buffer A without DTT.

Cantilevers. The cantilevers, made from silicon nitride using micromachining techniques, were 140 nm thick, 2 μm wide, and 9–11 μm long. The rear side of the cantilevers was coated with gold 20 nm thick. All surfaces of the cantilevers were further coated with osmium, about 2 nm thick. The tips were grown by electron-beam deposition (15), with growth rate of about 5 nm/s. The tip length was adjusted to ≈1.0 μm. The radius of the tip end was 6–8 nm. The mechanical properties of the cantilevers were tested by measuring the spectra of their thermal motion. The resonance frequencies were 1.3–1.8 MHz in air, and 450–650 kHz in water, and the spring constants were estimated to be 150–280 pN/nm.

Deflection Detection System. We used an optical lever method to measure the deflection of a cantilever. The optics must generate

Abbreviations: AFM, atomic force microscope; PID, proportional-integral-differential: S/H, sample/hold.

†To whom reprint requests should be addressed. E-mail: tando@kenroku.kanazawa-u.ac.jp.

The publication costs of this article were defrayed in part by page charge payment. This article must therefore be hereby marked "*advertisement*" in accordance with 18 U.S.C. §1734 solely to indicate this fact.

www.pnas.org/cgi/doi/10.1073/pnas.211400898

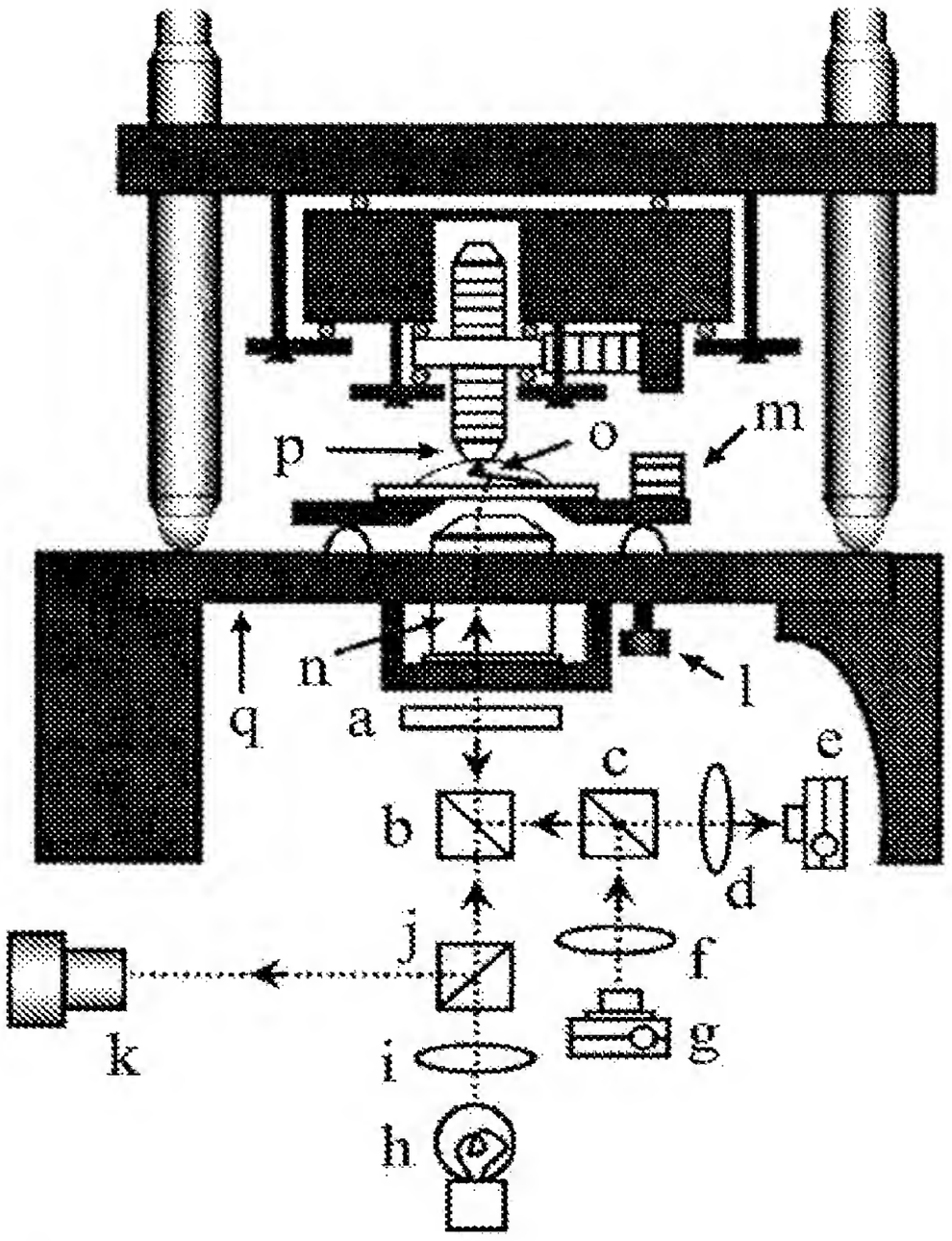

Fig. 1. Schematic drawing of the AFM head integrated with an inverted type of optical microscope. (*a*) λ/4 Plate. (*b*) Dichroic mirror. (*c*) Polarization beam splitter. (*d*) Focusing lens. (*e*) Split photodiode. (*f*) Collimator lens. (*g*) Laser diode. (*h*) Illumination lamp. (*i*) Collimator lens. (*j*) Half mirror. (*k*) Viewing system of the optical microscope. (*l*) Screw for adjusting the cantilever height. (*m*) Piezo for exciting cantilever. (*n*) Objective lens. (*o*) Cantilever. (*p*) Sample stage. (*q*) Sample stage of the optical microscope. All of the components (*a–g* and *n*) of the deflection detection system are hung down from the sample stage of the optical microscope. The scanner (see Fig. 2 also) is mounted on the same sample stage. The collimated laser beam is reflected up, incident on the objective lens at an off-centered position. The outgoing beam thus tilted about 10° from the vertical plane is focused onto the cantilever whose plane is tilted about 10° from the horizontal plane. The beam reflected at the cantilever is collimated by the objective lens, separated from the incident beam by the polarization beam splitter with λ/4 wave plate, and reflected onto the split photodiode. The optical microscope allows us to view the cantilever and the focused laser spot. The specimen is supported at the bottom of the sample stage (*p*), and an inverted cantilever (*o*) probes the specimen from below.

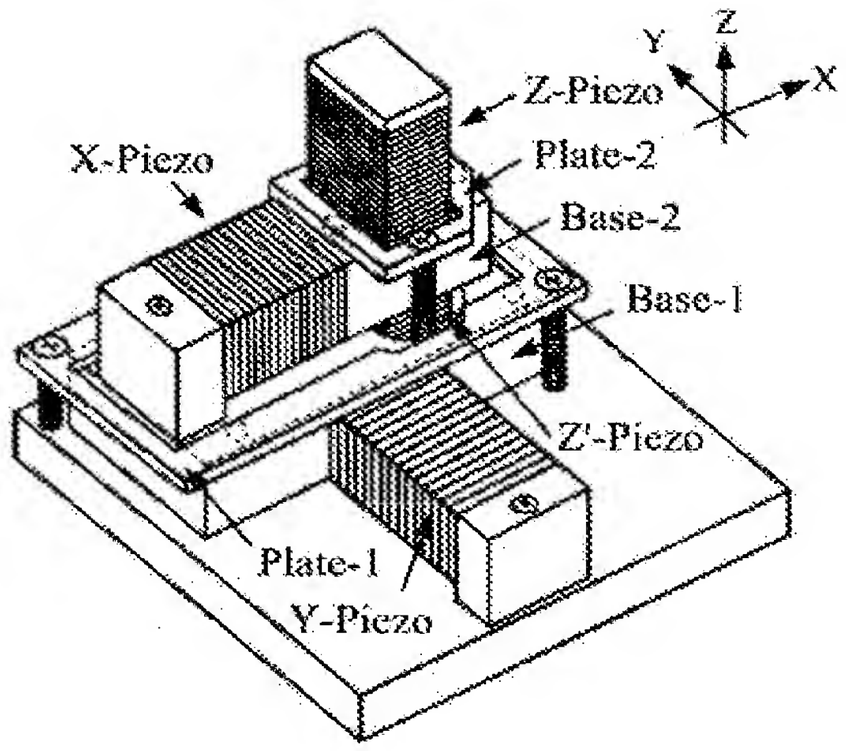

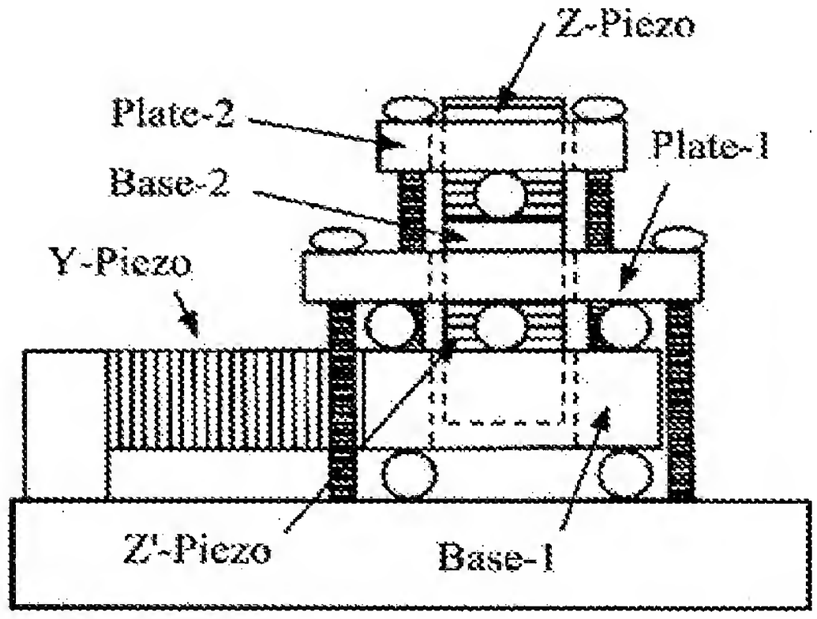

Fig. 2. Scanner assembly. (*Lower*) The side view when looked at the scanner from +x to −x. The scanner has a two-layered structure that guarantees that the x-scan and the y-scan do not interfere with each other. For structural details, see the text.

a very small incident beam spot, because our cantilevers for rapid scanning are much smaller than commercially available cantilevers. Schäffer *et al.* (16) designed an AFM using optics for small cantilevers, wherein a laser beam reflected from the rear side of the cantilever is collected and collimated with the same lenses as are used for focusing the incident laser beam onto the cantilever. We used the same method, but instead of using single lenses we used an objective lens (CFI Plan Fluor ELWD 20xC, Nikon) with a long working distance of 8 mm. As shown in Fig. 1, our AFM is integrated with an inverted type of optical microscope (IX50, Olympus, Tokyo). The focusing objective lens also is used to view the cantilever and the focused laser spot with the optical microscope. The focused spot is 2–3 μm in diameter. In the design of Schäffer *et al.*, the entire optical train is tilted from the vertical so that the incident beam is normal to the plane of the cantilever. Instead of this, we used a much simpler design wherein the vertical laser beam is incident on an off-centered position of the objective lens to make the outgoing beam axis normal to the plain of the cantilever. The incident and reflected light beams were separated by polarization using a beam splitter and a quaterwave plate. The laser beam, reflected, collimated, and then slightly converged, is fed into the two closely spaced photodetectors (S2721–02, Hamamatsu Photonics, Hamamatsu City, Japan) whose photocurrents are sent to a differential amplifier with a wide bandwidth (2.5 MHz).

Scanner. The scanner is shown in Fig. 2. Stack piezoelectric actuators (AE0203D04, Tokin, Tokyo) are used in this scanner. They have the resonance frequency of 260 kHz in free oscillation, their maximum displacement is 4.5 μm, and their capacitance is 90 nF. The y-piezo displaces base-1 on which the x- and z-scanners are mounted, while the x-piezo displaces base-2 on which the z-scanner is mounted. The z-scanner has two z-piezo actuators placed in the opposite direction to one another (the reason is described below). Base-1 is glued to the y-piezo, and base-2 is glued to the x- and z-piezo actuators. A sample stage

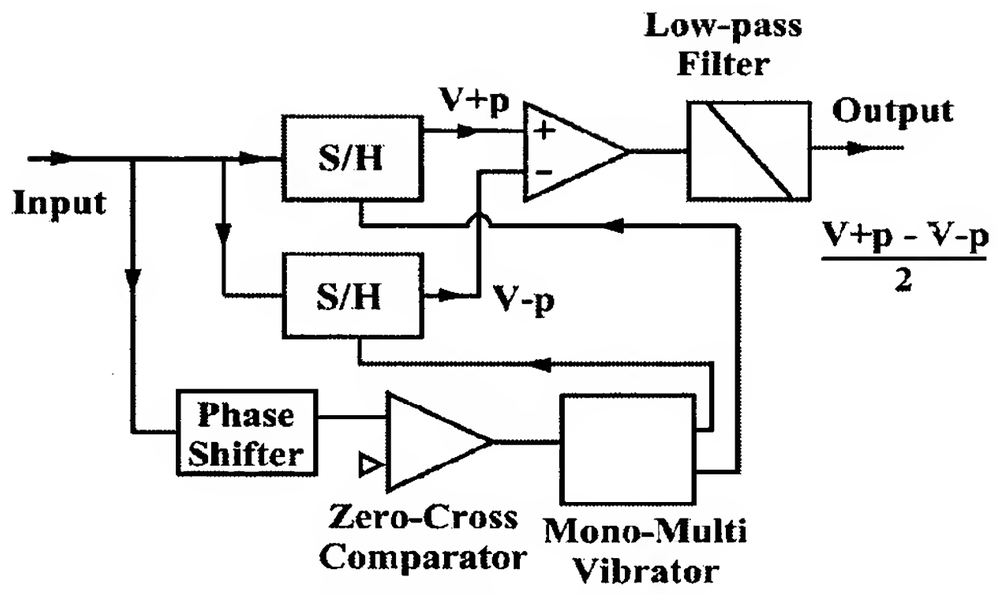

Fig. 3. Circuit for fast amplitude measurement. The output sinusoidal signal from the split-photodiode amplifier is fed to this circuit. The output of this circuit provides the amplitude of the sinusoidal input signal at periodicity of the input signal. For details, see the text.

is attached to one of the z-piezo actuators via a thin layer of vacuum grease. When the z-piezo is displaced quickly, hydrodynamic force is generated as the reaction from the sample solution to the sample stage. To minimize this reactive force, a glass of a circular-trapezoid shape with a small top surface of 1-mm diameter is used as the sample stage. To hold the mass balance, a dummy stage that has the same mass as the sample stage was attached to the other z-piezo actuator. Base-1 sits on three steel ball bearings, and its top plane is pushed down by plate-1 through three steel ball bearings. The balls are 1 mm in diameter. Base-2 is also held between base-1 and plate-2 in a similar manner. This way of holding base-1 and base-2 between two flat surfaces reduces vibrations of these bases in the z-direction and allows smooth displacements in the desired directions. However, these arrangements are not sufficient to minimize such vibrations. Quick displacements of a z-piezo exert impulsive forces on base-2, which causes vibrations of base-2, and in turn vibrates the z-piezo itself. Such impulsive forces are countered by the simultaneous displacements of the two z-piezo actuators of the same length, in the counter direction.

Electronics. The custom-made piezo-drive amplifiers have a 1-MHz bandwidth for a 90-nF capacitive load, in 2 Vp-p output. These amplifiers are used to drive the z-piezo actuators and to drive another piezo actuator (custom-made; with a 2-MHz resonance frequency) that excites the cantilever in the tapping mode AFM operation. The x- and y-piezo actuators are driven by amplifiers (HJPZ-0.15Px3, Matsusada Precision, Tokyo) with a 25-kHz bandwidth for a 90-nF capacitive load, in 100 Vp-p output. The PID and two types of rms-to-dc circuits were custom-made. The bandwidth of the PID circuit is 300 kHz. An analog type of rms-to-dc converter with a fourth-order low-pass filter can accept up to a 1-MHz input signal and requires five waves of the signal to output an accurate rms value; in other words, five tip-sample contacts are needed to measure the tapping amplitude. To increase the conversion rate, we made a novel circuit with 1-MHz bandwidth, which requires only one wave to generate the amplitude signal (Fig. 3). The input (source) signal is divided into two. One is sent to two sample/hold (S/H) circuits. The other is sent to a 90° phase shifter, and its output is fed to a zero-cross comparator to generate rectangular wave signals. These rectangular signals are sent to a mono-stable multivibrator to generate pulses at the top and bottom peaks of the input source signal. The pulses from the mono-stable multi vibrator are used as triggers to hold the source signal by the S/Hs. The outputs from the two S/Hs are sent to a differential amplifier to generate output that represents the amplitude of the source signal. The signal generation for the x-y scan, and the data sampling are made in different ways. One is made by using a digital-signal-processor (DSP) control board integrated with A/D and D/A converters. This allows flexible controls for AFM imaging, but its operation rate is limited because of our slow DSP system. The other is made by using an external circuit that generates analog signals for the x-y scan and timing pulses for data acquisition, and by using a fast A/D board for data sampling. This system allows a fast operation (the pixel clock can go up to 1 MHz).

AFM Head Assembly. The sample stage of the inverted type of optical microscope was replaced with a stainless steel plate 10 mm thick. Every mechanical and optical component of the AFM is mounted on or hung from this plate. This design reduces relative movement between these components, despite vibrations of the optical microscope itself, which is susceptible to the ambient sounds or mechanical noises because of its low resonance frequency. Because we use confocal optics for focusing the laser beam onto a cantilever, as well as for viewing the cantilever and the incident spot with the optical microscope, the rear side of the cantilever must face downward (and hence, the tip must stick upward). This setup is opposite to that widely used in commercial AFMs. The cantilever is attached to a transparent glass plate via a short cantilever holder glued to the glass plate. The scanner, with a sample stage facing downward, is mounted over the cantilever (see Fig. 1).

Imaging Bandwidth. When a piezo actuator is oscillated with its one end being fixed, its resonance frequency is half the resonance frequency when it is oscillated with both ends free. So, the z-piezo actuators must have a resonance frequency of 130 kHz, without considering the mass attached to the free end of the actuators. The z-scanner in the whole scanner assembly must have a lower mechanical resonance frequency, considering the mass (of the order of g), the size (of the order of mm), and the Young's modulus (of the order of 10^{10}–10^{11} N/m^2) of the materials such as super invar steel and resin used in the piezo actuators. Therefore, the z-scanner is the component that is most difficult to optimize for high-speed scanning. We tested the z-scanner's ability to follow a frequency modulation of the driving signal, without a feedback system, while the tip of a cantilever remained in contact with a mica surface. The sensor output is shown as a function of the driving frequency (Fig. 4). When the z-piezo for the counterbalance was not operating, the z-scanner showed resonance vibrations around 8.5 kHz, 34 kHz, and 100 kHz (Fig. 4*a*). The resonance at 100 kHz is caused by the resonance of the z-piezo actuator itself. The extra amplitudes gained by resonance at the lower frequencies are, however, relatively small compared with the oscillation amplitude without resonance, indicating the value of our scanner design in suppressing the resonance vibrations. When the counterbalancer was operating (Fig. 4*b*), the extra amplitudes at the lower resonance frequencies were reduced, and we further noticed much less variation in the amplitude over frequencies lower than 60 kHz, compared with those without counterbalance.

The bandwidth of the whole feedback loop system was assessed by measuring the system's ability to follow a modulation of the set point while the tip was in contact with a mica surface (12). Sinusoidal signals were sent to the set point input, and the output of the PID was fed to a lock-in amplifier to measure the amplitude and the phase relative to the input sinusoidal signals. The output amplitude was almost constant up to 60 kHz, and then gradually decreased with increasing frequency. This gradual decrease is caused by the resonance oscillation of the z-scanner around 100 kHz. The phase difference was zero over the frequencies tested (up to 100 kHz). These results indicate

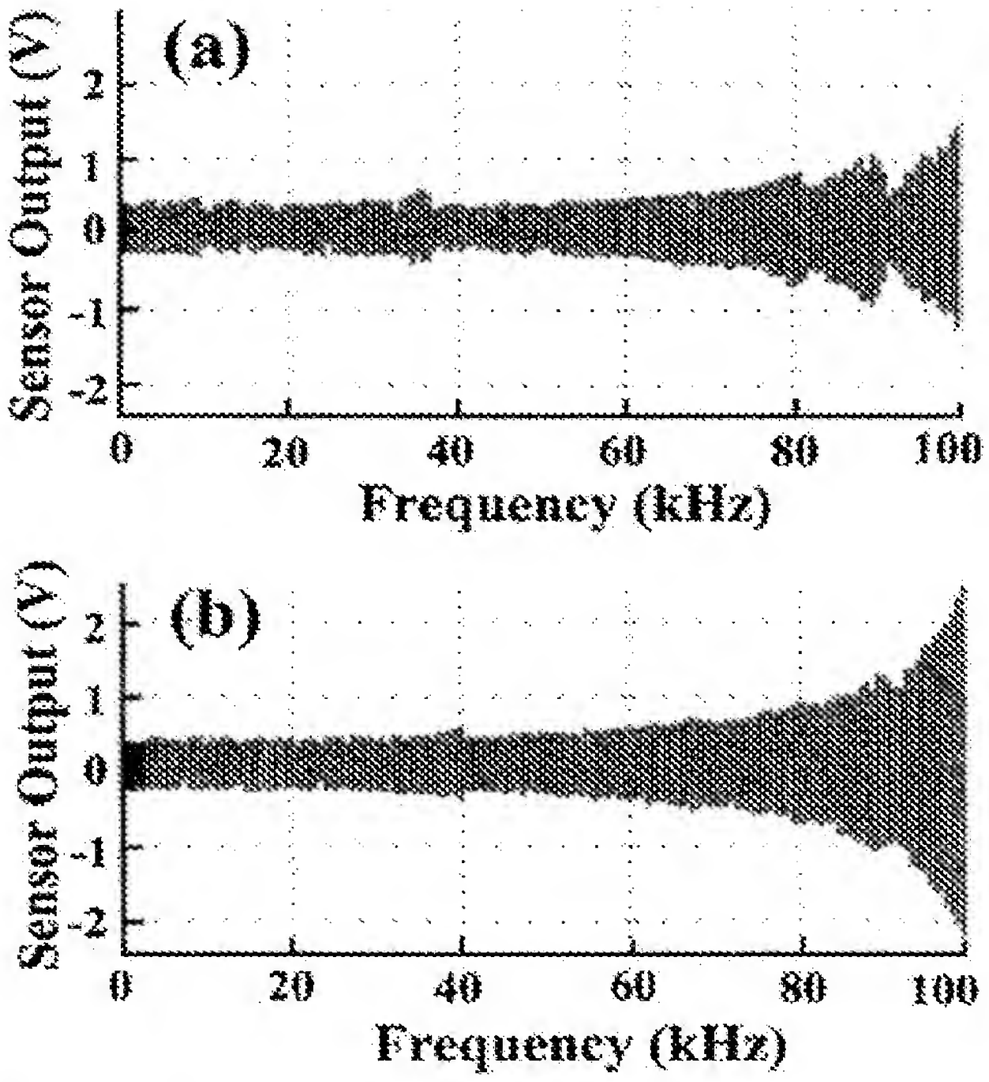

Fig. 4. Oscillation of the z-scanner as a function of the driving frequency. The amplitude of the driving signal was kept constant while sweeping its frequency. The data were obtained with (*b*) or without (*a*) operating the z-piezo for the counterbalance.

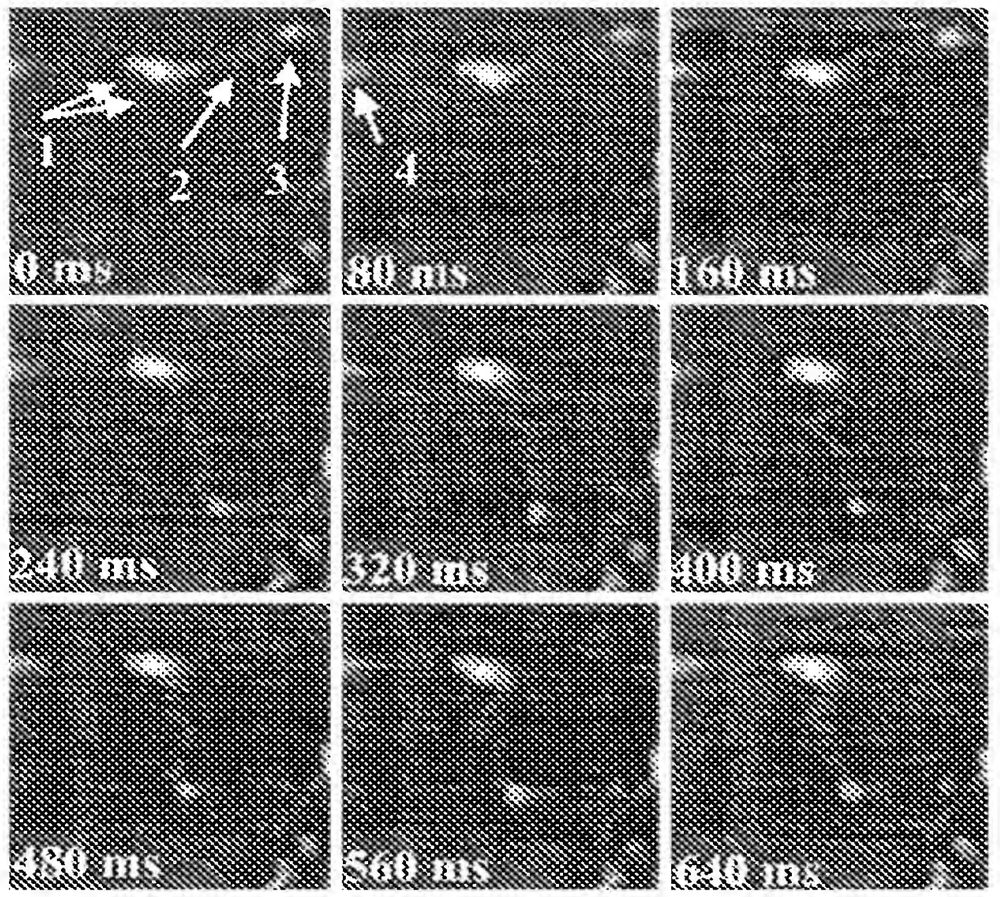

Fig. 5. Successive images of myosin V on mica in buffer solution. The same area of 240 × 240 nm^2 was imaged 50 times with 100 × 100 pixels. Only nine successive images are shown. The tip speed is 0.6 mm/s (scan rate, 1.25 kHz), and the frame rate is 12.5/s. The tapping frequency is 620 kHz, the amplitude of the cantilever's free oscillation is 12 nm, and the set point is about 11.5 nm. In the first image, the head/neck regions, the long tail, and the globular tail end are marked with arrow 1, arrow 2, and arrow 3, respectively. A mirror image of one of the head region is marked with arrow-4 in the second image. The still panels here appear noisier than the dynamic images in the movie on the web site http://www.s.kanazawa-u.ac.jp/phys/biophys/bmv_movie.htm. The two head/neck regions are overlapped in the z direction, and therefore, they are not well resolved and do not show a typical "Y" shape. Dynamic images of myosin V that show "Y" shape are also presented at http://www.s.kanazawa-u.ac.jp/phys/biophys/bmv_movie.htm.

that the component that has the lowest bandwidth in the system is the z-scanner, and therefore, the bandwidth of the system is about 60 kHz.

The minimum imaging time (t) per frame with N^2 pixels of size p is given by

$$t = N^2 p / w f_s, \qquad [1]$$

where f_s is the bandwidth of the feedback loop, and w is the apparent width of features on the surface. w is given by convolution of the tip with radius R and the sample with radius r, and is approximated as $w = \sqrt{rR}$ (17). A scan range of 200 nm and 100^2 pixels, thus a pixel size of 2 nm, can be scanned in 33 ms for $w = 10$ nm and $f_s = 60$ kHz. Because the corresponding pixel time is 1.65 μs, this scan condition requires the tapping and data sampling frequencies to be equal to, or larger than 606 kHz (the reciprocal of the pixel time). One step of the x-y scan has to be completed within this pixel time.

Imaging. We examined whether imaging can really be made at (or near to) the maximum rate expected above. Myosin V directly attached to mica, in solution containing 2 mM ATP, was imaged successively (240-nm scan range; 100^2 pixels) for 4 sec (50 frames). The scan rate was 1.25 kHz, corresponding to a tip speed of 0.6 mm/s, and the frame rate was 12.5 s^{-1}. In the myosin V molecule located on the center of the images (Fig. 5), its two head/neck regions, one long tail, and the globular tail end are clearly resolved. The tail seems to be about 100 nm long, longer than a previous estimate based on its primary structure and the electron microscopic images (18). The angle of the long tail relative to the head/neck regions changed between the eighth and ninth frames (see the third and fourth images in Fig. 5). After this quick change, the tail and the tail end are slowly moving. The reconstructed movie and the other movies that dramatically show the changes in the locations of the myosin heads, neck, and tail regions can be viewed at http://www.s.kanazawa-u.ac.jp/phys/biophys/bmv_movie.htm. We tried faster imaging (25 frames/sec for 240-nm area with 100 × 100 pixels), but it was not successful because of the inertia of the mass attached to the free end of the x-piezo. This inertia produces mirror images on the left half area of the total image. Note that even in Fig. 5 mirror images are noticed (indicated by arrow-4 in the second image).

Discussion

The components that limit the imaging rate of our AFM are first the x-scanner, and second the z-scanner and the cantilever. An upper limit of the imaging rate that is reachable by improving these components can be estimated. We used super invar steel for base-2. To minimize the inertia of the mass, we may be able to use hard ceramics for base-2, which can reduce the mass to a quarter, and therefore can increase the imaging rate four times. Cantilevers smaller than those we made can be constructed. For instance, a silicon nitride cantilever, 42 nm thick, 6 μm long, and 2 μm wide, may be possible, although this will be probably the smallest size, considering how it has to be used in practice. This small cantilever with a gold coat will have the likely resonance frequency of ≈2.5 MHz in air and the spring constant of ≈200 pN/nm. The resonance frequency in water must be around 1.2 MHz, about two times larger than that of our present cantilevers. In the tapping mode operation with this cantilever the pixel imaging time can be reduced to 0.83 μs, which corresponds to 17

ms of the imaging time, for 100^2 pixels. If the second harmonic oscillation can be used, the imaging time can be reduced to 8.3 ms. The speed limit of our z-scanner arises from the resonance frequency of the piezo actuator. Piezo actuators with higher resonance frequency are available, but their maximum displacement is shorter. Considering the necessary displacement size, say, 1 μm, the maximum resonance frequency will be about 1 MHz when one end of such a piezo actuator is fixed. This is about seven times larger than that used in this study. Considerations made here suggest that an upper limit of the imaging time seems to be 10~20 ms, as long as we use the optical deflection detection method as well as the tapping mode operation.

The long tail of a myosin V molecule changed its orientation in less than ≈30 ms (just before the change, the tail end located at y ≈ 214 nm (i.e., at almost the end of the frame scan), while just after the change the tail end located at y ≈ 64 nm). On the other hand, after the quick change the tail moved slowly. This marked contrast suggests that this quick orientational change may be driven by ATP. However, at present we must reserve judgment, because we could not observe repeated orientational change with the same myosin V molecule. To decide this, we have to record images for a much longer time, because the ATPase rate of myosin V alone is very small (≈0.05/s). At present our AFM system cannot store many images at once. In the near future we may be able to resolve this problem.

In life science, it has been a dream to view the nanometer-scale dynamic behavior of individual biopolymers in solution. The capacity of acquiring successive images every 80 ms will allow a large expansion in the scope of biological processes that can be examined in real time. In the near future we should be able to see the behavior of processive motors [such as kinesin (19) and myosin V (20)] walking along their tracks, or of molecular chaperones assisting a polypeptide chain to fold (21). Such direct observations will be a great help in understanding the mechanisms by which biomolecular machines operate.

We thank Keichi Mukai and Ryuki Tsunekawa for their help in making the AFM head, Takeshi Sakamoto and Tatsuya Kinosita for preparing myosin V, and Professor Manuel Morales (University of the Pacific) for his continuous encouragement and for reviewing this manuscript. This work was supported by the Proposal-Based New Industry Creative Type Technology R&D Promotion Program from the New Energy and Industrial Technology Development Organization (NEDO) of Japan to T.A.

1. Binnig, G., Quate, C. F. & Gerber, C. (1986) *Phys. Rev. Lett.* **56,** 930–933.
2. Drake, B., Prater, C. B., Weisenhorn, A. L., Gould, S. A., Albrecht, T. R., Quate, C. F., Cannell, D. S., Hansma, H. G. & Hansma, P. K. (1989) *Science* **243,** 1586–1589.
3. Bustamante, C., Rivetti, C. & Keller, D. J. (1997) *Curr. Opin. Struct. Biol.* **7,** 709–716.
4. Guthold, M., Bezanilla, M., Erie, D. A., Jenkins, B., Hansma, H. G. & Bustamante, C. (1994) *Proc. Natl. Acad. Sci. USA* **91,** 12927–12931.
5. Kassas, S., Thomson, N. H., Smith, B. L., Hansma, H. G., Zhu, X., Guthold, M., Bustamante, C., Kool, E. T., Kashlev, M. & Hansma, P. K. (1997) *Biochemistry* **36,** 461–468.
6. Oberleithner, H., Schneider, S. & Bustamante, J.-O. (1996) *Pflügers Arch. Eur. J. Physiol.* **432,** 839–844.
7. Putman, C. A. J., Van der Werf, K. O., De Grooth, B. G., Van Hulst, N. F. & Greve, J. (1994) *Appl. Phys. Lett.* **64,** 2454–2456.
8. Schäffer, T. E., Viani, M., Walters, D. A., Drake, B., Runge, E. K., Cleveland, J. P., Wendman, M. A. & Hansma, P. K. (1997) *Proc. SPIE* **3009,** 48–52.
9. Walters, D. A., Viani, M., Paloczi, G. T., Schäffer, T. E., Cleveland, J. P., Wendman, M. A., Gurley, G., Elings, V. & Hansma, P. K. (1997) *Proc. SPIE* **3009,** 43–47.
10. Viani, M. B., Schäffer, T. E., Paloczi, G. T., Pietrasanta, L. I., Smith, B. L., Thompson, J. B., Richter, M., Rief, M., Gaub, H. E., Plaxco, K. W., *et al.* (1999) *Rev. Sci. Instrum.* **70,** 4300–4303.
11. Viani, M. B., Pietrasanta, L. I., Thompson, J. B., Chand, A., Gebeshuber, I. C., Kindt, J. H., Richter, M., Hansma, H. G. & Hansma, P. K. (2000) *Nat. Struct. Biol.* **7,** 644–647.
12. Sulchek, T., Hsieh, R., Adams, J. D., Minne, S. C., Quate, C. F. & Adderton, D. M. (2000) *Rev. Sci. Instrum.* **71,** 2097–2009.
13. Minne, S. C., Manalis, S. R. & Quate, C. F. (1995) *Appl. Phys. Lett.* **67,** 3918–3920.
14. Cheney, R. E. (1998) *Methods Enzymol.* **298,** 3–18.
15. Keller, D. J. & Chih-Chung, C. (1992) *Surf. Sci.* **268,** 333–339.
16. Schäffer, T. E., Cleveland, J. P., Ohnesorge, F., Walters, D. A. & Hansma, P. K. (1996) *J. Appl. Phys.* **80,** 3622–3627.
17. van Noort, S. J. T., van der Werf, K. O., de Grooth, B. G. & Greve, J. (1999) *Biophys. J.* **77,** 2295–2303.
18. Cheney, R. E., O'Shea, M. K., Heuser, J. E., Coelho, M. V., Wolenski, J. S., Espreafico, E. M., Forscher, P., Larson, R. E. & Mooseker, M. S. (1993) *Cell* **75,** 13–23.
19. Vale, R. D., Funatsu, T., Pierce, D. W., Romberg, L., Harada, Y. & Yanagida, T. (1996) *Nature (London)* **380,** 451–453.
20. Sakamoto, T., Amitani, I., Yokota, E. & Ando, T. (2000) *Biochem. Biophys. Res. Commun.* **272,** 586–590.
21. Saibil, H. (2000) *Curr. Opin. Struct. Biol.* **10,** 251–258.

Anal Bioanal Chem (2003) 377 : 528–539
DOI 10.1007/s00216-003-2101-0

REVIEW

Jiří Homola

Present and future of surface plasmon resonance biosensors

Received: 20 March 2003 / Revised: 4 June 2003 / Accepted: 5 June 2003 / Published online: 19 July 2003
© Springer-Verlag 2003

Abstract Surface plasmon resonance (SPR) biosensors are optical sensors exploiting special electromagnetic waves – surface plasmon-polaritons – to probe interactions between an analyte in solution and a biomolecular recognition element immobilized on the SPR sensor surface. Major application areas include detection of biological analytes and analysis of biomolecular interactions where SPR biosensors provide benefits of label-free real-time analytical technology. This paper reviews fundamentals of SPR affinity biosensors and discusses recent advances in development and applications of SPR biosensors.

Keywords Optical sensor · Biosensor · Affinity biosensor · Immunosensor · Surface plasmon resonance

Introduction

The last two decades have witnessed remarkable progress in the development of affinity biosensors and their applications in areas such as environmental protection, biotechnology, medical diagnostics, drug screening, food safety, and security. An affinity biosensor consists of a transducer (electrochemical [1], piezoelectric [2], or optical [3]) and a biological recognition element which is able to interact with a selected analyte. Various optical methods have been exploited in biosensors including fluorescence spectroscopy [4], interferometry (reflectometric white light interferometry [5] and modal interferometry in optical waveguide structures [6]), spectroscopy of guided modes of optical waveguides (grating coupler [7] and resonant mirror [8]), and surface plasmon resonance (SPR) [9, 10]. Fluorescence-based biosensors offer high sensitivity but, due to the use of labels, they require either multi-step detection protocols or delicately balanced affinities of interacting biomolecules for displacement assays, causing sensor cross-sensitivity to non-target analytes [11]. Sensors such as optical interferometers, grating coupler, resonant mirror, and SPR rely on the measurement of binding-induced refractive index changes and thus are label-free technologies. This paper focuses on SPR biosensor technology, reviews fundamentals of SPR sensing, and discusses advances in development and applications of SPR biosensors and emerging trends in SPR biosensing.

J. Homola (✉)
Institute of Radio Engineering and Electronics,
Academy of Sciences of the Czech Republic,
Chaberská 57, Prague, Czech Republic
e-mail: homola@ure.cas.cz

Fundamentals of surface plasmon resonance (SPR) biosensors

Surface plasmon-polariton

A surface plasma wave (SPW) or a surface plasmon-polariton is an electromagnetic wave which propagates along the boundary between a dielectric and a metal, which behaves like quasi-free electron plasma [12, 13]. An SPW is a transverse-magnetic (TM) wave (magnetic vector is parallel to the plane of interface) and is characterized by the propagation constant and electromagnetic field distribution. The propagation constant of an SPW, β, can be expressed as:

$$\beta = \frac{\omega}{c}\sqrt{\frac{\varepsilon_M \varepsilon_D}{\varepsilon_M + \varepsilon_D}} \quad (1)$$

where ω is the angular frequency, c is the speed of light in vacuum, and ε_D and ε_M are dielectric functions of the dielectric and metal, respectively [12, 13]. This equation describes an SPW if the real part of ε_M is negative and its absolute value is smaller than ε_D. At optical wavelengths this condition is fulfilled for several metals of which gold is most commonly employed in SPR biosensors. The real and imaginary parts of the propagation constant describe spatial periodicity and attenuation of an SPW in the direction of propagation, respectively [12]. The electromagnetic field of an SPW is confined at the metal–dielectric boundary and decreases exponentially into both media,

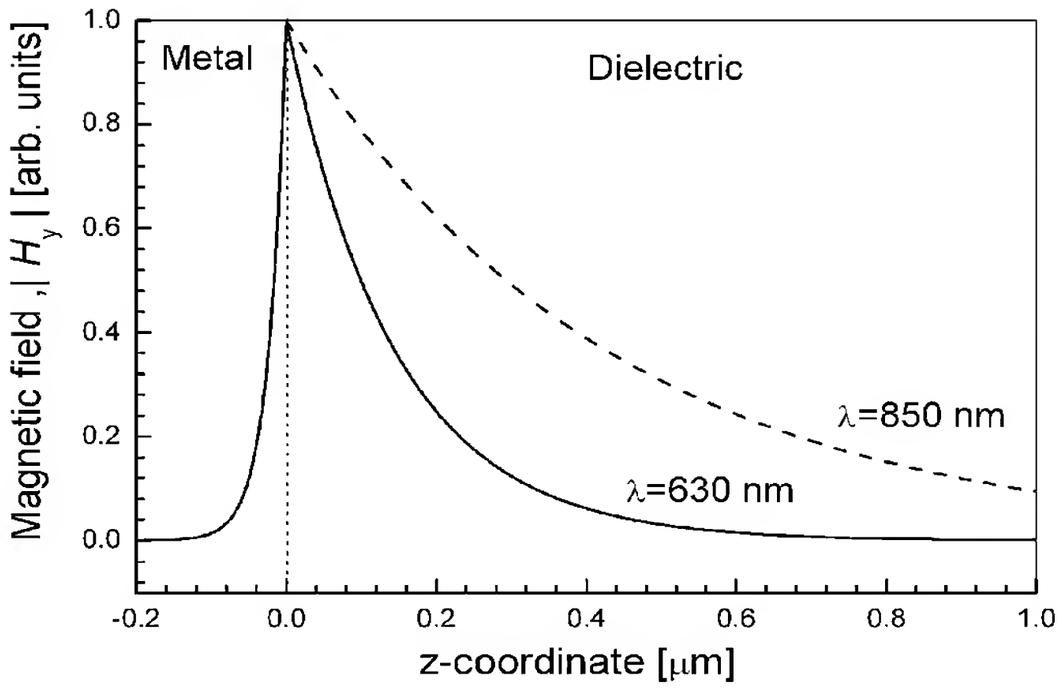

Fig. 1 Distribution of the magnetic field intensity for an SPW at the interface between gold and dielectric (refractive index of the dielectric 1.32) in the direction perpendicular to the interface calculated for two different wavelengths

Fig. 1. For an SPW at the boundary between gold and a dielectric with a refractive index of 1.32 the penetration depth (the distance from the interface at which the amplitude of the field falls to $1/e$ of its value at the metal surface) into the dielectric is typically 100–500 nm in the visible and near infrared regions [10, 13].

Concept of surface plasmon resonance biosensing

Owing to the fact that the vast majority of the field of an SPW is concentrated in the dielectric, the propagation constant of the SPW is extremely sensitive to changes in the refractive index of the dielectric. This property of SPW is the underlying physical principle of affinity SPR biosensors – biomolecular recognition elements on the surface of metal recognize and capture analyte present in a liquid sample producing a local increase in the refractive index at the metal surface. The refractive index increase gives rise to an increase in the propagation constant of SPW propagating along the metal surface (Fig. 2) which can be accurately measured by optical means.

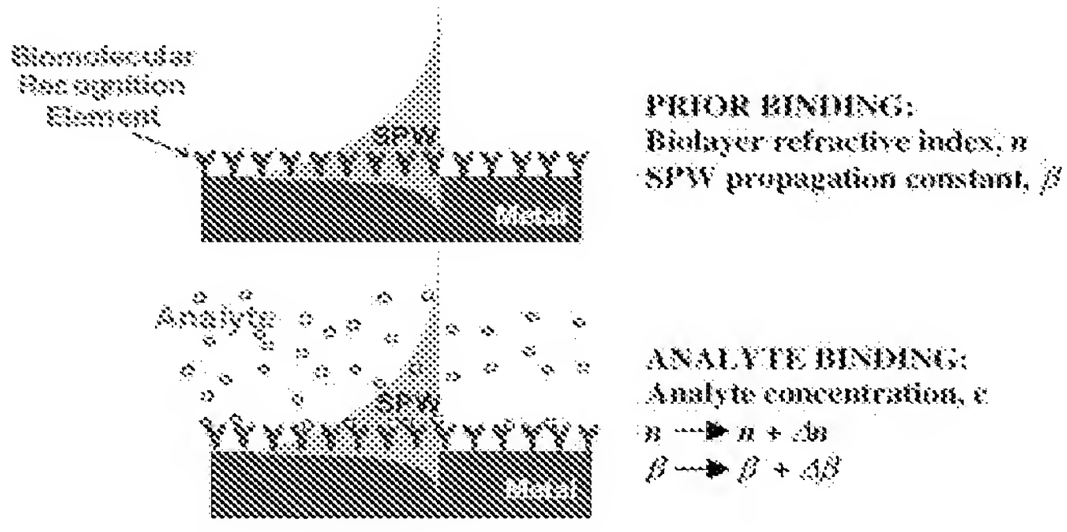

Fig. 2 Principle of SPR biosensing

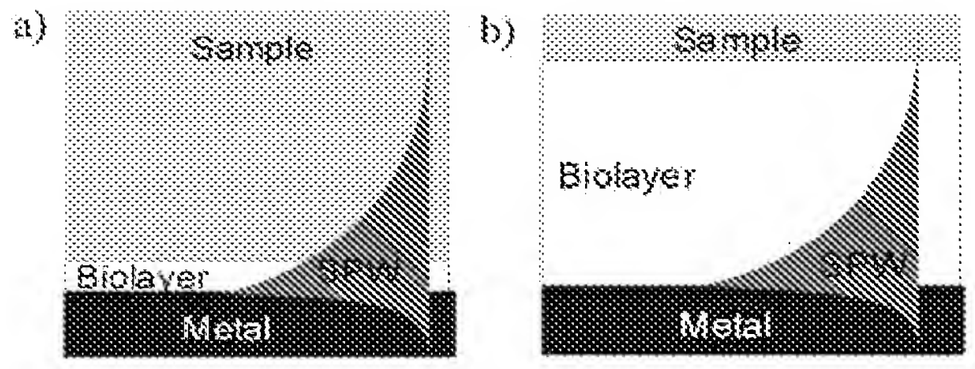

Fig. 3 Surface plasmon-polariton probing: (**a**) biomolecular interaction occurring within a short distance from metal surface, and (**b**) biomolecular interaction occurring within the whole extent of the field of a SPW

The magnitude of the change in the propagation constant of an SPW depends on the refractive index change and its distribution with respect to the profile of the SPW field. There are two limiting cases:

1. analyte capture occurs only within a short distance from the metal surface (Fig. 3a), and
2. analyte capture occurs within the whole extent of the SPW field (Fig. 3b).

Perturbation theory [14] suggests that if the binding occurs within the whole depth of the SPW field (Fig. 3b), the binding-induced refractive index change, Δn, produces a change in the real part of the propagation constant, $\Delta\beta$, which is directly proportional to the refractive index change:

$$\mathrm{Re}\{\Delta\beta\} \cong k\Delta n \tag{2}$$

where k denotes the free-space wavenumber [15]. If the refractive index change is caused by a binding event occurring within a distance from the surface d, much smaller than the penetration depth of the SPW, the corresponding change in the real part of the propagation constant can be expressed as follows:

$$\mathrm{Re}\{\Delta\beta\} \cong \frac{2n_s n_f k^2 d}{\sqrt{|\mathrm{Re}\{\varepsilon_m\}|}}\Delta n = Fk\Delta n \tag{3}$$

where n_f and n_s denote the refractive index of the biolayer and the refractive index of the background dielectric medium (sample), respectively. The binding-induced change in the propagation constant of the SPW is proportional to the refractive index change and the depth of the area within which the change occurs. The factor F ($F<1$) accounts for the fact that the interaction occurring within a thin layer is probed by only a fraction of the field of the SPW.

Excitation and interrogation of surface plasmon-polaritons

In SPR sensors, an SPW is excited by a light wave and the effect of this interaction on the characteristics of the light wave is measured. From these measurements, changes in the propagation constant of the SPW can be determined. Excitation of an SPW by light can occur only if the com-

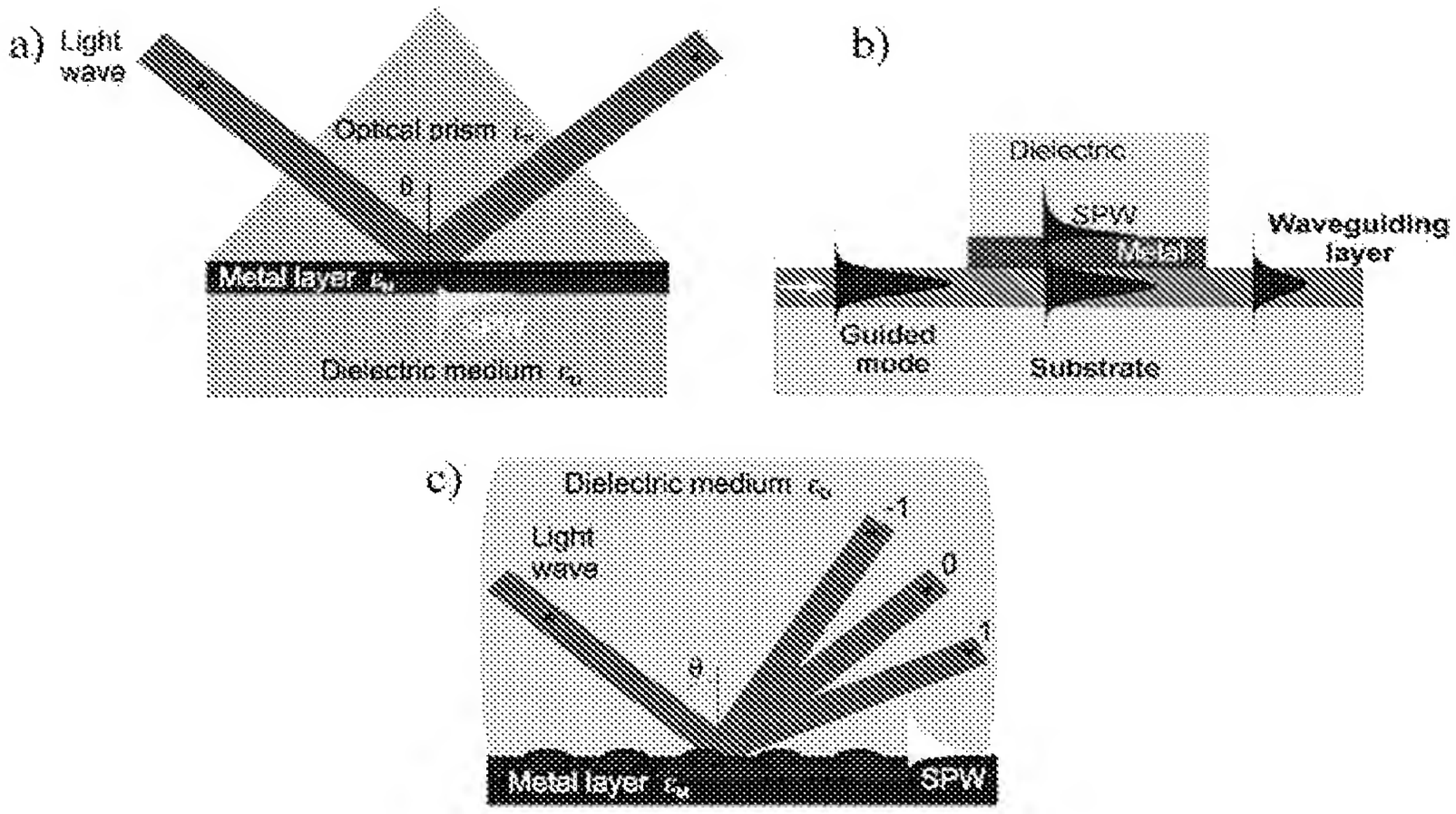

Fig. 4 Excitation of surface plasmon-polaritons: (**a**) by a light beam via prism coupling, (**b**) by a guided mode of optical waveguide, and (**c**) by light diffraction on a diffraction grating

ponent of the light's wave vector that is parallel to the metal surface matches that of the SPW. This can be achieved by means of prism coupling, waveguide coupling, and grating coupling.

In configurations based on prism coupling a light wave passes through a high refractive index prism and is totally reflected at the prism–metal layer interface generating an evanescent wave penetrating the metal layer (Fig. 4a). This evanescent wave propagates along the interface with a propagation constant which can be adjusted to match that of the SPW by controlling the angle of incidence. This method is referred to as the attenuated total reflection (ATR) method [13]. The process of exciting an SPW in an optical waveguide-based SPR structure (Fig. 4b) is similar to that in the ATR coupler. The light wave is guided by an optical waveguide and, when entering the region with a thin metal layer, it evanescently penetrates through the metal layer exciting an SPW at its outer boundary. Alternatively, an SPW can be excited by diffraction on a grating, Fig. 4c. The component of the wave vector of the diffracted waves parallel to the interface is diffraction-increased by an amount which is inversely proportional to the period of the grating and can be matched to that of an SPW [16]. The interaction of a light wave with an SPW can alter light's characteristics such as amplitude, phase, polarization and spectral distribution. Changes in these characteristics can be correlated with changes in the propagation constant of the SPW. Therefore, binding-induced changes in the refractive index at the sensor surface and, consequently, the propagation constant of the SPW can be determined by measuring changes in one of these characteristics. Based on which characteristic is measured, SPR biosensors can be classified as angle, wavelength, intensity, phase, or polarization modulation-based sensors. In SPR sensors with angular modulation the component of the light wave's wavevector parallel to the metal surface matching that of the SPW is determined by measuring the coupling strength at a fixed wavelength and multiple angles of incidence of the light wave and determining the angle of incidence

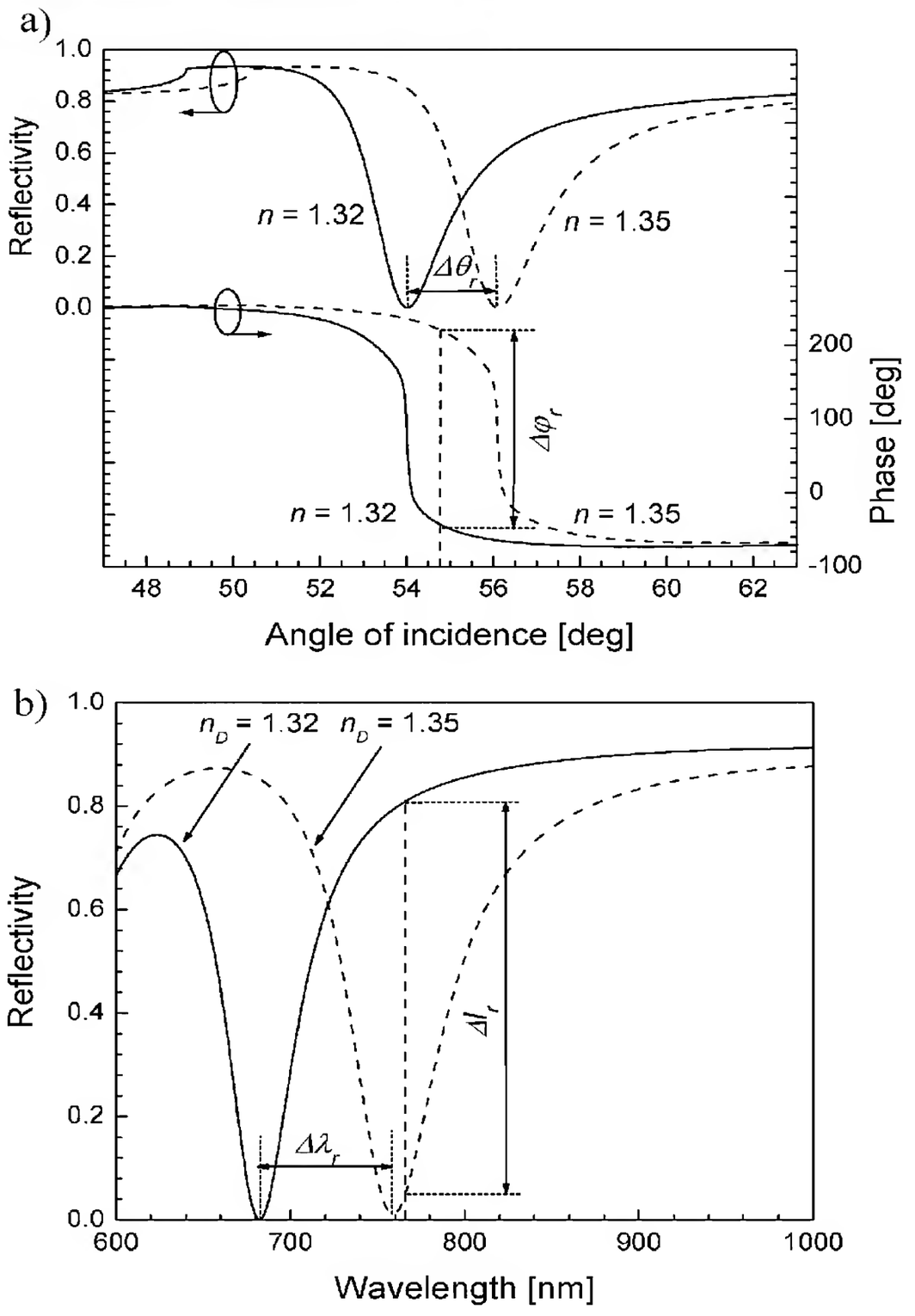

Fig. 5 Reflectivity and phase for light wave exciting an SPW in the Kretschmann geometry (SF14 glass prism – 50 nm thick gold layer – dielectric) versus (**a**) the angle of incidence for two different refractive indices of the dielectric (wavelength 682 nm), and (**b**) wavelength for two different refractive indices of the dielectric (angle of incidence 54°)

yielding the strongest coupling (Fig. 5a, upper plot). In SPR sensors with wavelength modulation the component of the light wave's wavevector parallel to the metal surface matching that of the SPW is determined by measuring the coupling strength at a fixed angle of incidence and multiple wavelengths and determining the wavelength yielding the strongest coupling (Fig. 5b). In SPR sensors with intensity modulation, the change in the intensity of the light wave interacting with the SPW is measured at a fixed wavelength and angle of incidence (Fig. 5b). In SPR sensors with phase modulation, shift in phase of the light wave interacting with the SPW is measured at a fixed wavelength and angle of incidence (Fig. 5a, lower plot). In SPR sensors with polarization modulation, changes in the polarization are measured at a fixed wavelength and angle of incidence.

Performance characteristics

The main performance characteristics relevant for SPR biosensors include sensitivity, accuracy, precision, repeatability, and the lowest detection limit. Sensor *sensitivity* S, is the ratio of the change in sensor output, P (e.g. angle of incidence, wavelength, intensity, phase, and polarization of light wave interacting with an SPW) to the change in measurand (e.g. analyte concentration, c). SPR biosensor sensitivity can be decomposed into two components – sensitivity to refractive index changes produced by the binding of analyte to biomolecular recognition elements on the sensor surface S_{RI}, and the efficiency E, with which the presence of analyte at a concentration c is converted into the change in the refractive index n:

$$S = \frac{\partial P}{\partial n}\frac{\partial n}{\partial c} = S_{RI}E \tag{4}$$

The efficiency E depends on the properties of the biomolecular recognition elements and the target analyte. The refractive index sensitivity S_{RI} can be decomposed into two terms:

$$S_{RI} = \frac{\partial P}{\partial \mathrm{Re}\{\beta\}}\frac{\partial \mathrm{Re}\{\beta\}}{\partial n} = S_1 S_2 \tag{5}$$

The first term S_1 depends on the modulation method and the method of excitation of an SPW [17, 18, 19, 20]. The S_2 term is independent of the modulation method and the method of excitation of the SPW and describes the sensitivity of SPW's propagation constant to the refractive index change, Eqs. (2) and (3).

Accuracy describes the degree to which a sensor output represents the true value of the measurand (analyte concentration). Accuracy is often confused with *precision* which refers to the way in which repeated measurements conform to themselves without a reference to any true value. *Repeatability* refers to the capacity of a sensor to reproduce output reading under the same measurement conditions over a short interval of time. The *lowest detection limit* describes the lowest concentration of analyte that can be measured by the sensor.

SPR biosensing formats

An interaction between a biomolecular recognition element on an SPR sensor surface and analyte in a liquid sample is governed by kinetic equations. In order to illustrate fundamental properties of the interaction, we shall discuss the pseudo-first-order kinetic equation:

$$\frac{\mathrm{d}R}{\mathrm{d}t} = k_a c(1-R) - k_d R \tag{6}$$

where R is the relative amount of bound analyte, c is analyte concentration, t is time, and k_a and k_d are the association and dissociation kinetic rate constants, respectively [21]. This interaction model assumes 1:1 binding, rapid mixing of the analyte from the bulk phase to the sensor surface layer, and single-step binding. Observed binding, however, may deviate from this simple model due to more complex mechanisms of interaction and mass transport limitations [22]. Equation (6) yields for R:

$$R(t) = \left[\frac{k_a c}{k_a c + k_d} - R_0\right]\left(1 - e^{-(k_a c + k_d)t}\right) + R_0 \tag{7}$$

where R_0 denotes the initial amount of analyte bound at the time t=0 [21].

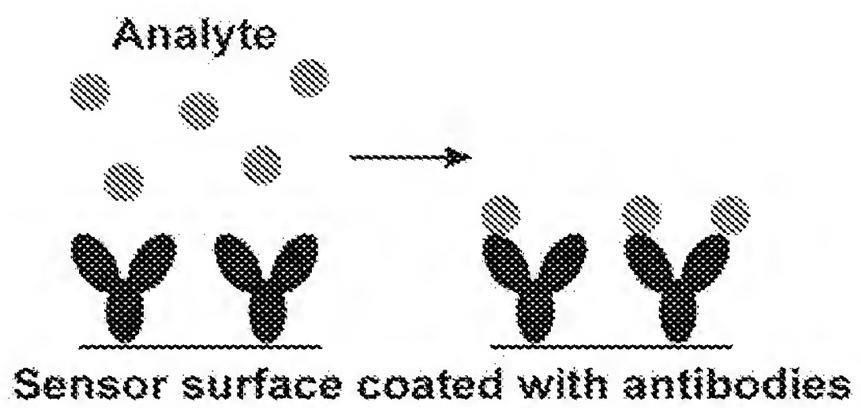

Fig. 6 Direct detection

Fig. 7 Direct detection. Binding between antibody and analyte calculated for four different concentrations of analyte, k_a=3×10^5 mol^{-1} L s^{-1}; k_d=5×10^{-4} s^{-1}

Various measurement formats have been adopted in SPR biosensing to ensure that the monitored binding event produces a measurable sensor response. The most frequently used measurement formats are direct detection, sandwich assay, and inhibition assay. In direct detection format, analyte in a sample interacts with a biomolecular recognition element (antibody) immobilized on the sensor surface, Fig. 6. The resulting refractive index change is directly proportional to the concentration of analyte.

Figure 7 which shows a kinetic model of the interaction between antibody and analyte suggests that the binding between the target analyte and antibody is fast initially. As the interaction progresses, the binding rate gradually decreases and eventually reaches a state in which the association and dissociation processes are in equilibrium. The time required for the interaction to reach the equilibrium depends on the concentration of analyte and is longer for lower concentrations of analyte.

Figure 8a shows dependence of the relative binding at equilibrium on the concentrations of analyte. At low analyte concentrations the equilibrium binding increases linearly with analyte concentration. At higher analyte concentrations, the binding sites provided by the biomolecular recognition elements are saturated and a further increase in the analyte concentration produces a smaller increase in the amount of bound analyte. The initial binding rate dR/dt (t=0) is directly proportional to the association rate constant and analyte concentration (Fig. 8b). Both the amount of analyte bound at equilibrium and initial binding rate can be used to determine analyte concentration. The measurement of the binding rate is faster and offers a larger dynamic range than measurement of the equilibrium binding. In the *sandwich assay format* the measurement consists of two steps. In the first step, sample containing analyte is brought in contact with the sensor and the analyte molecules bind to the antibodies on the sensor surface. Then the sensor surface is incubated with a solution containing „secondary" antibodies. The secondary antibodies bind to the previously captured analyte further increasing the number of bound biomolecules (Fig. 9) and thus also the sensor response.

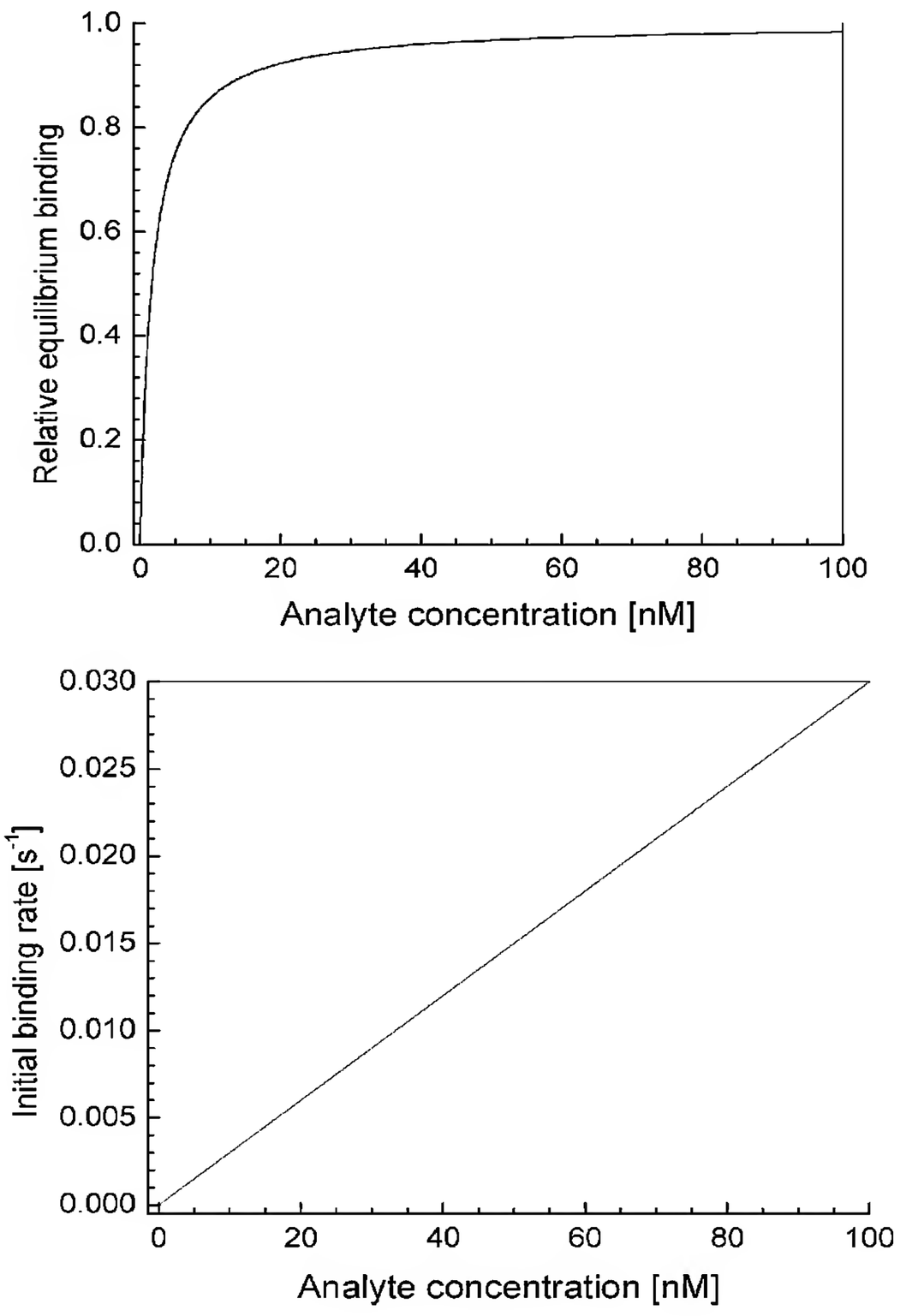

Fig. 8 Direct detection: (*top*) relative equilibrium binding as a function of analyte concentration; (*bottom*) initial binding rate as a function of analyte concentration, k_a=3×10^5 mol^{-1} L s^{-1}; k_d=5×10^{-4} s^{-1}

The *inhibition assay* is an example of a competitive assay. In this detection format, a sample is initially mixed with respective antibodies and then the mixture is brought in contact with the sensor surface coated with analyte molecules, so that the unoccupied antibodies could bind to the analyte molecules (Fig. 10).

The amount of bound analyte versus time may be estimated by calculating the equilibrium concentration of antibody which did not bind to the analyte in the sample and then simulating the interaction between the unbound antibody and the analyte-derivatized surface. Figure 11 shows the equilibrium binding and the initial binding rate as a function of analyte concentration, assuming that antibody at a concentration of 0.1 nmol L^{-1} was incubated with sample and the mixture was provided with enough time to reach equilibrium. The amount of bound antibody and the

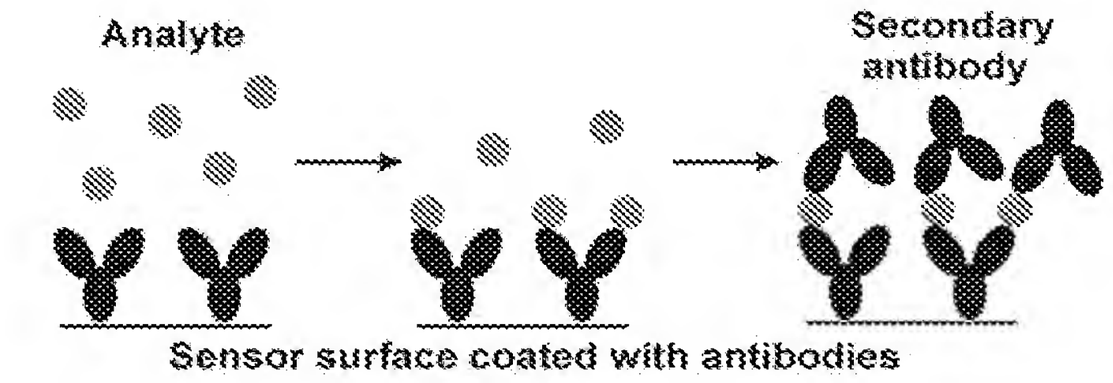

Fig. 9 Sandwich assay

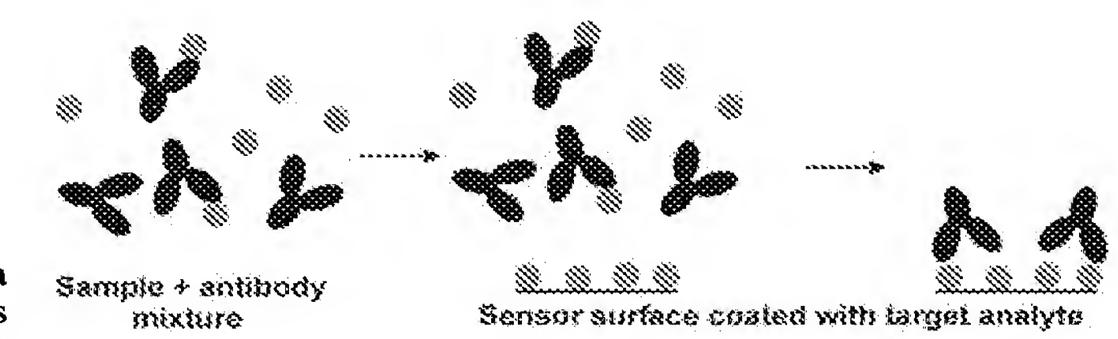

Fig. 10 Inhibition assay

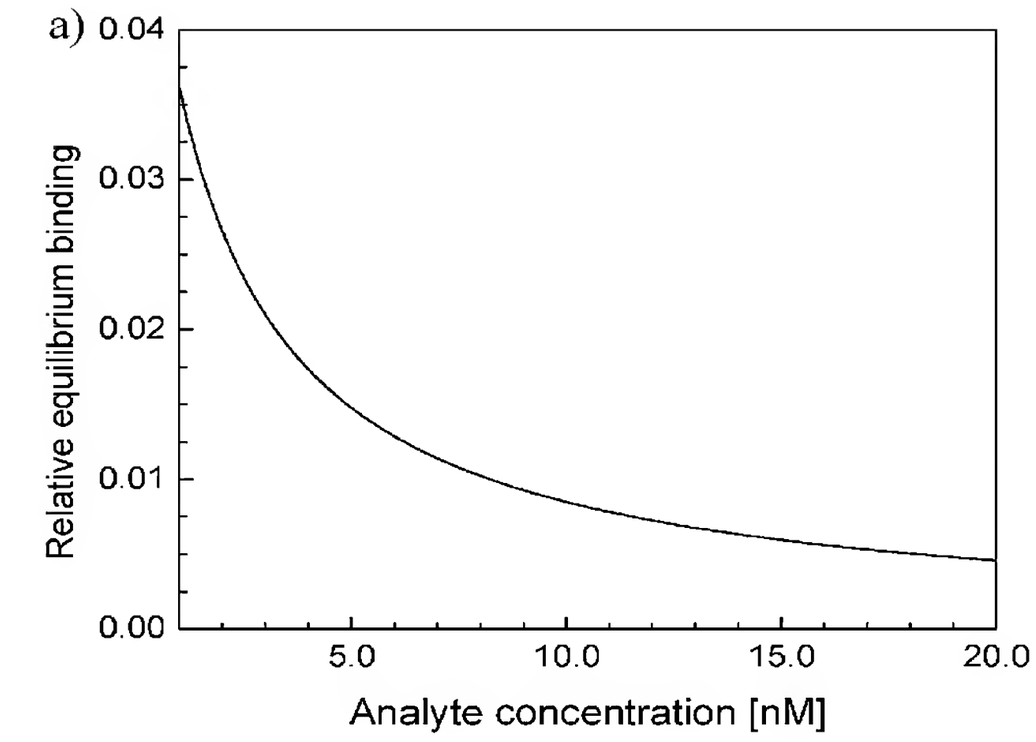

Fig. 11 Inhibition assay: (**a**) relative equilibrium binding of the antibody as a function of analyte concentration; (**b**) initial binding rate as a function of analyte concentration; k_a=3×10^5 mol^{-1} L s^{-1}; k_d=5×10^{-4} s^{-1}; antibody concentration 0.1 nmol L^{-1}

initial binding rate are inversely proportional to analyte concentration, Fig. 11.

Features and challenges

SPR biosensor technology exhibits various advantageous features. These include in particular:

1. Versatility – generic SPR sensor platforms can be tailored for detection of any analyte, providing a biomolecular recognition element recognizing the analyte is available; analyte does not have to exhibit any special properties such as fluorescence or characteristic absorption and scattering bands.
2. No labels required – binding between the biomolecular recognition element and analyte can be observed directly without the use of radioactive or fluorescent labels.
3. Speed of analysis – the binding event can be observed in real-time providing potentially rapid response.
4. Flexibility – SPR sensors can perform continuous monitoring as well as one-time analyses.

SPR biosensors exhibit two inherent limitations:

1. Specificity of detection – specificity is solely based on the ability of biomolecular recognition elements to recognize and capture analyte. Biomolecular recognition elements may exhibit cross-sensitivity to structurally similar but non-target molecules. If the non-target molecules are present in a sample in a high concentration, sensor response due to the non-target analyte molecules may conceal specific response produced by low levels of target analyte.
2. Sensitivity to interfering effects – similar to other affinity biosensors relying on measurement of refractive index changes, SPR biosensor measurements can be compromised by interfering effects which produce refractive index variations. These include non-specific interaction between the sensor surface and sample (adsorption of non-target molecules by the sensor surface), and background refractive index variations (due to sample temperature and composition fluctuations).

Advances in SPR biosensor technology

This paper follows up an SPR sensor technology review paper published in *Sensors and Actuators B* in 1999 [9], and therefore focuses primarily on recent advances in SPR biosensor technology. In this section the following areas are discussed in particular: SPR sensor platforms, data analysis, and biomolecular recognition elements.

Instrumentation

In recent years, research into optical platforms for SPR biosensors has been increasingly application-oriented, targeting specific application areas and providing solutions meeting unique requirements of specific applications. Two important representatives of this trend are: development of laboratory SPR sensor platforms with a large number of sensing channels for high-throughput screening applications and development of mobile SPR sensor platforms for analysis of complex samples in the field.

In traditional multichannel SPR sensors, SPWs were excited via a prism coupler in multiple areas which were arranged perpendicularly to the direction of propagation of SPWs; angular [23] or spectral [24] distribution of reflected light was analyzed to yield information about the measurand in each channel. While this spectroscopic approach led to development of high-performance SPR sensing devices [23], the number of sensing channels which could be realized using this approach was rather limited (<10). In order to increase the number of sensing channels, various SPR sensor platforms have been proposed [25, 26, 27, 28]. One approach is based on SPR imaging

in which a collimated light beam from a polychromatic light source passes through a prism and is made incident on an SPR-active metal layer; the reflected light is detected with a CCD camera after passing through a narrow-band interference filter [25]. This approach has been demonstrated for monitoring of adsorption of a single-stranded DNA-binding protein on to single-stranded DNA patterned into an array of 500×500-micron squares [29]. The choice of operating wavelength for imaging SPR sensors have been discussed by Johansen et al. [30]. An alternative approach [26] is based on detection of spatial changes in the phase of light exciting an SPW and interferometry. Two interferometric schemes have been proposed. In the Mach–Zehnder interferometer-based scheme monochromatic light was split into reference and signal beams; the signal beam passed through a prism and, after reflection from an SPR-active metal layer, was recombined with the reference beam producing an interference pattern on a CCD camera [28]. In the TE–TM polarization interferometer TE and TM polarized beams passed through a prism and, after reflection from an SPR-active surface, were shifted with respect to each other and recombined by means of a polarizer producing an interference pattern on a CCD camera [26]. Another interesting approach is based on SPR microscopy [31] and uses surface scanning and SPWs excited by means of an objective lens [27]. Most recently a new approach has been proposed which is based on spectroscopy of SPW on an array of diffraction gratings [32].

A great deal of research has been focused on development of mobile SPR sensor platforms with referencing capabilities enabling applications of SPR biosensors in out-of-laboratory environments and for analysis of complex samples. The traditional approach consisted in simultaneous SPR measurements in two sensing channels containing different biomolecular recognition element coatings, one with (signal channel) and one without (reference channel) affinity for the analyte, and subtraction of the reference channel response from that of the signal channel [24]. Recently, a new approach to multichannel SPR sensing has been developed which is based on excitation of surface plasmons in different sensing channels at different wavelengths and encoding information from different sensing channels into different regions of the light spectrum. This can be accomplished in a sensing element of special design in which light is made incident on the SPR-active metal at different angles of incidence (Fig. 12a) [33], or by employing a thin dielectric overlayer which shifts the resonant wavelength for a part of the sensing surface to longer wavelengths (Fig. 12b) [34]. This approach has been demonstrated to have capacity to discriminate effects occurring in the proximity of the sensor surface (specific binding, non-specific adsorption) from those occurring in the whole medium (interfering background refractive index fluctuations) which is a prerequisite for advanced referencing [35]. Referencing approaches have been studied [36, 37]. It was found that a residual error for compensation of interfering background refractive index variations is typically 1–3% of the total refractive index change;

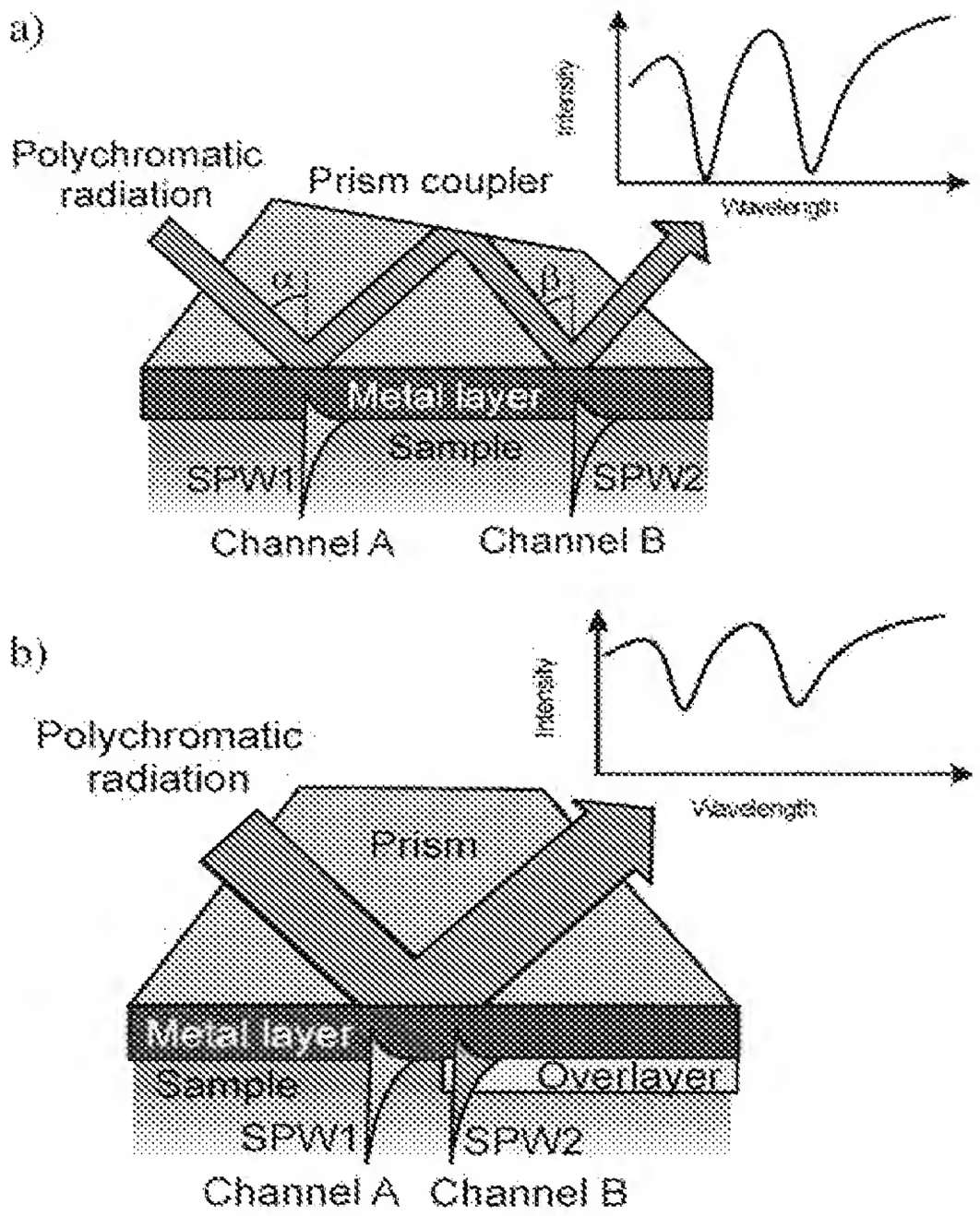

Fig. 12 Dual-surface-plasmon spectroscopy. (**a**) Geometry with two different angles of incidence [33]. (**b**) Geometry with a high refractive index overlayer [34]

compensation for temperature variations is less accurate with an error of 5–10% of the total response due to the temperature change [37].

There is continuing effort to develop miniature SPR platforms based on miniaturized prism couplers [38] and optical fibers. The first fiber optic SPR sensors were based on wavelength-modulation in multimode optical fibers with partly removed cladding and a metal film deposited symmetrically around the exposed section of fiber core [39] or on intensity-modulation in single-mode optical fibers which were side-polished and coated with a thin metal film [40]. These SPR sensors suffered from modal noise (multimode fiber-based sensors) and polarization instability (single-mode fiber-based sensors). Two methods of overcoming the limitation originating from the need to precisely control polarization of light in the single-mode optical fiber-based SPR sensors have been developed. In the first method, light from a polychromatic light source passes through a Lyott fiber optic depolarizer which produces unpolarized light which is then coupled into a fiber optic SPR sensing element. The transmitted light is analyzed with a spectrograph [41]. The second method uses a polarization-maintaining fiber to control polarization of light in the fiber-optic SPR sensing element, Fig. 13. This approach provides best suppression of polarization effects due to fiber

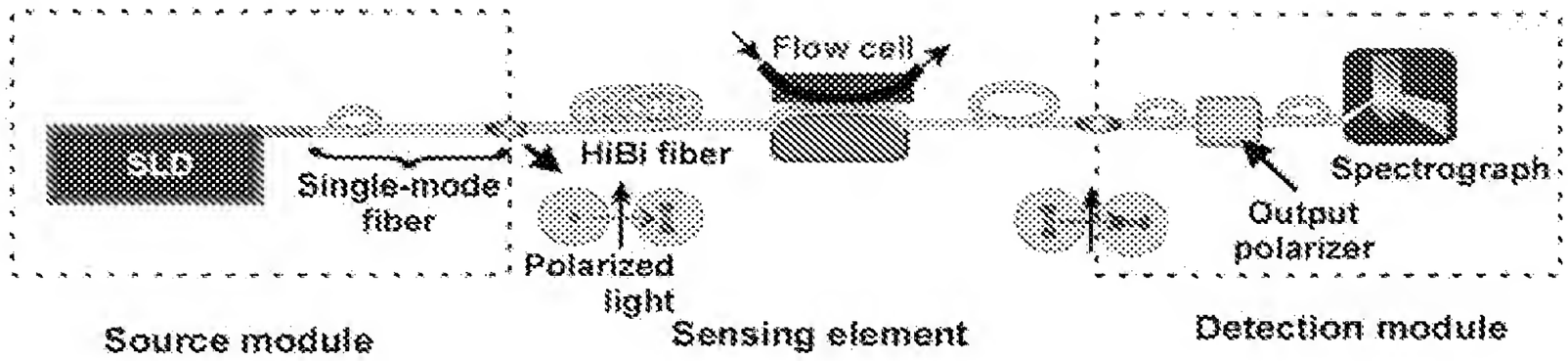

Fig. 13 SPR sensor based on a polarization-maintaining single-mode optical fiber

deformations resulting in enhanced-stability fiber optic SPR sensors with performance comparable to bulk-optic SPR sensors [42].

Research is also carried out to improve detection capabilities of SPR biosensors by exploiting a special type of an SPW, the so-called long-range surface plasmon. The use of long-range surface plasmons provides two benefits – increased sensitivity and very narrow angular or spectral dips, which makes it possible to determine the spectral position of the SPR dip with a high accuracy [43]. As long-range surface plasma waves penetrate deeper into the probed medium, their use benefits especially biosensors with extended matrices of biomolecular recognition elements [44].

Sensor data analysis

Detection limits of SPR biosensors are ultimately constrained by the noise-based precision of the SPR instrument itself. The precision depends on noise contributions made by individual components of an SPR sensor and data processing method. Therefore, study of noise in SPR sensors and development of optimized algorithms for processing data from SPR sensors have received much attention lately. Earlier approaches to understanding the performance of SPR sensor data analysis have included studies of the effects of noise and comparisons between algorithms. Locally-weighted parametric regression and other methods were compared for low- and high-noise detectors, demonstrating that a small number of low-noise detector pixels may outperform a larger but noisier detector array [45]. Linearization of data processing algorithms and an optimal linear data analysis method were proposed as a means of optimizing algorithm parameters [46]. Contribution of analog-to-digital converter resolution and number of pixels in the detector array to the performance of a number of SPR data-analysis algorithms was studied [47]. Also, effects of sensitivity deviations on concentration analyses and kinetic studies have been investigated [48]. Most recently, sources of noise were investigated for a wavelength-modulated SPR sensor. Shot noise of the detector was found to be the dominant source of noise and an analytical formula was derived which allows prediction of the noise of the sensor output based on the detector noise [49].

Biomolecular recognition elements and their immobilization

The main types of biomolecular recognition elements used in SPR biosensors include antibodies, nucleic acids and biomimetic materials. Antibodies are used most frequently because of their high affinity, versatility, and commercial availability. Various immobilization chemistries have been developed to attach antibodies to SPR-active gold films. Traditional approaches include formation of streptavidin layer on the gold surface followed by attachment of biotinylated antibodies [50], use of self-assembled alkanethiol films with suitable reactive groups [51], use of a hydrogel matrix composed of carboxyl-methylated dextran chains which can be modified allowing antibodies to be attached via surface-exposed amine, carboxyl, sulfhydryl, and aldehyde groups [52]. Alternatively, SPR sensing surfaces may be functionalized by thin polymer films to which antibodies are coupled via amino groups [53]. Protein contact printing has been examined for spatially-controlled attachment of bovine serum albumin (BSA) and dinitrophenylated BSA onto adjacent reference and signal channels of a dual-channel SPR sensor [54]. DNA can be immobilized on gold SPR sensor surfaces by formation of a streptavidin layer on a gold surface followed by attachment of biotinylated DNA [55]. A multistep surface modification based on alkanethiol self-assembled monolayers has also been used to attach DNA to gold surfaces [56]. Recently, biomimetic materials consisting in molecularly imprinted polymers (MIPs) have been exploited in SPR biosensors [57].

Applications of SPR biosensors

Two major application areas for SPR biosensing are in detection and identification of biological analytes and biophysical analysis of biomolecular interactions. This review focuses on applications for detection and identification of biological analytes; recent advances in SPR-based biomolecular interaction analysis can be found in Ref. [58].

Numerous SPR biosensors have been developed for detection and identification of specific analytes. These biosensors use a number of platform designs, biomolecular recognition elements and detection formats. The choice of detection format for a particular application depends on size of target analyte molecules, binding characteristics of biomolecular recognition element, and the range of ana-

lyte concentrations to be measured. Direct detection is usually preferred in applications where direct binding of analyte of concentrations of interest produces a sufficient response. If necessary, the lowest detection limits of the direct SPR biosensors can be improved by using sandwich assay. The secondary antibodies may also be coupled to large particles such as latex particles [59] and gold beads [60] to further enhance the SPR sensor response. Smaller analytes (molecular weight <1000) are usually measured using inhibition assay.

Detection of small analytes

SPR biosensors have been demonstrated for small analytes relevant to environmental protection (simazine and atrazine), medicine (morphine, methamphetamine, and theophyline), and food safety (fumonisin B1, sulfamethazine, and sulfadiazine). Minunni and Mascini used an SPR sensor and binding inhibition assay to detect atrazine [61]. Monoclonal antibodies against atrazine were mixed with a sample containing atrazine and free antibody concentration was determined by exposing the sample to an atrazine derivative-coated SPR biosensor. A detection limit of 0.05 ng mL^{-1} was achieved [61]. Figures 14 and 15 show typical sensorgrams for binding inhibition assay detection of atrazine using a wavelength-modulated SPR sensor; the antibody concentration was 4 μg mL^{-1}.

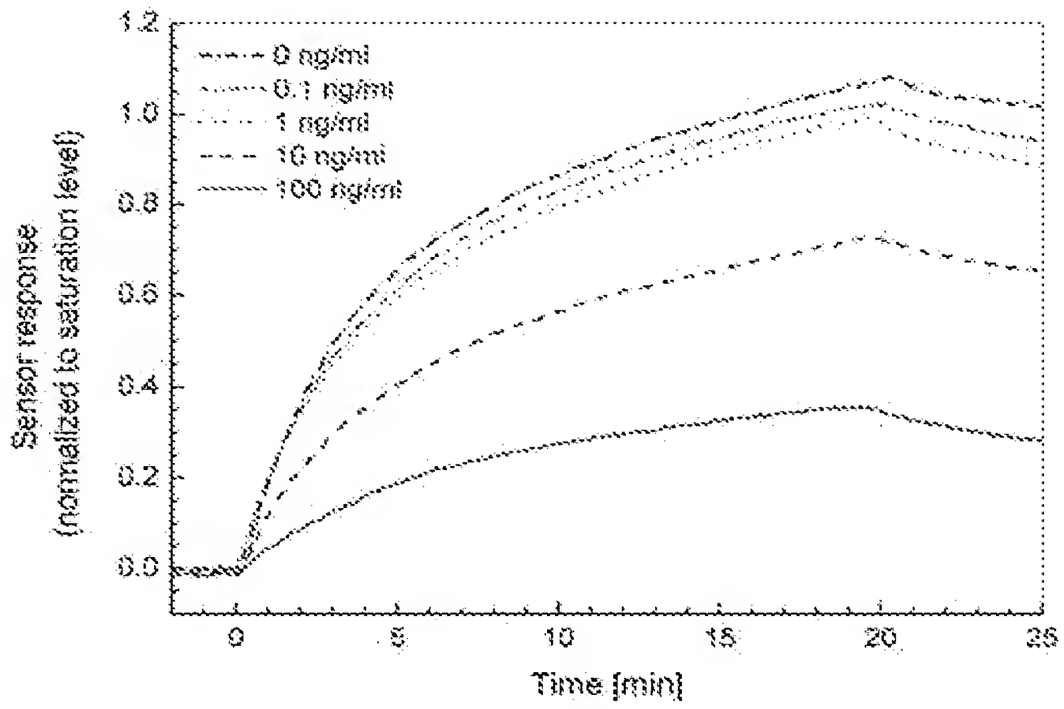

Fig. 14 Detection of atrazine using inhibition assay. Kinetic response

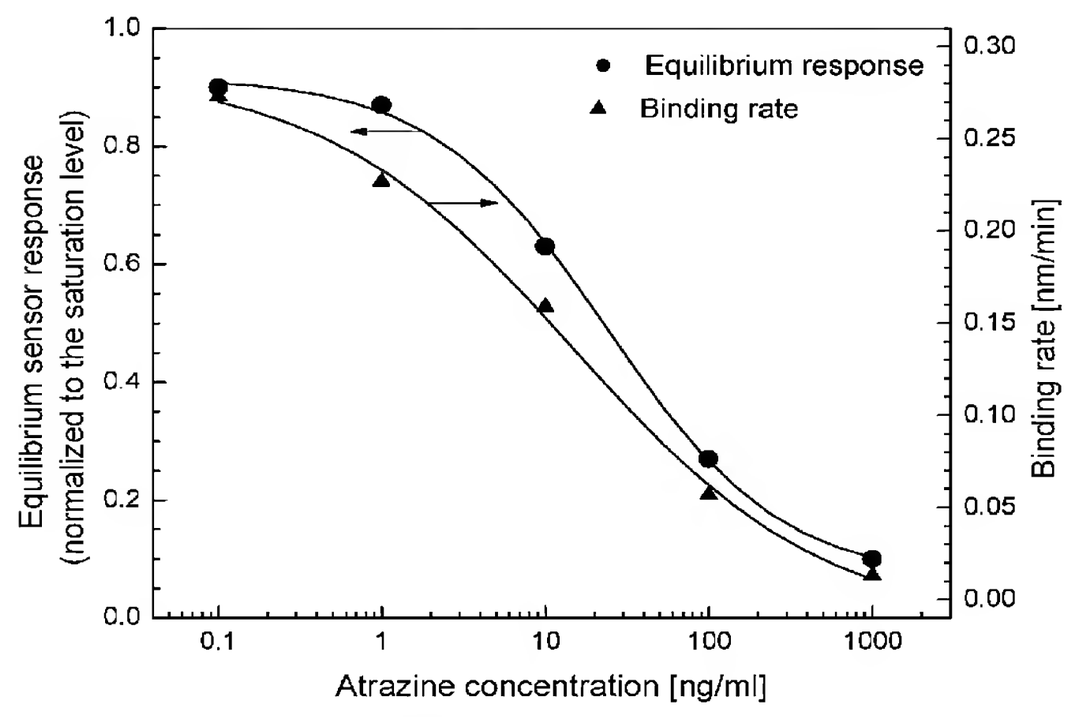

Fig. 15 Detection of atrazine using inhibition assay. Equilibrium response and initial binding rate as a function of atrazine concentration

Detection of the triazine herbicide simazine in water samples was demonstrated using an integrated optical SPR sensor and binding inhibition assay involving anti-simazine IgG antibodies or anti-simazine Fab fragments [62, 63]. The lowest detection limit for simazine was determined to be 0.16 ng mL^{-1} for anti-simazine IgG antibodies and 0.11 ng mL^{-1} for anti-simazine Fab fragments [63]. Morphine detection based on an SPR sensor and binding inhibition assay was reported by Miura et al. [64], who detected morphine at concentrations down to 0.1 ng mL^{-1}. Sakai et al. developed an SPR biosensor for detection of methamphetamine using binding inhibition assay; the lowest detection limit was determined to be 0.1 ng mL^{-1} [65]. Direct detection of fumonisin B1 in aqueous samples was demonstrated by Mullet et al. using a laboratory SPR system with angular modulation and polyclonal antibodies [66]. The detection limit was determined to be 50 ng mL^{-1}. Sulfamethazine in milk was detected using a commercial SPR system based on angular modulation (Biacore) and binding inhibition assay involving anti-sulfamethazine polyconal antibodies. The lowest detection limit for sulfamethazine was determined to be 1 ng mL^{-1} [67] and 2 ng mL^{-1} [68]. Baxter et al. demonstrated SPR biosensor-based detection of streptomycin in milk using a commercial SPR biosensor (Biacore 2000) and inhibition assay involving polyclonal anti-streptomycin antibodies. The lowest detection limit of the SPR biosensor for streptomycin was determined to be 4 ng mL^{-1} [69]. Elliott et al. demonstrated detection of sulfadiazine in pig bile using a commercial SPR biosensor (Biacore) and inhibition assay with a detection limit of 20 ng mL^{-1} [70]. A laboratory SPR biosensor with angular modulation was combined with a molecularly imprinted polymer for detection of theophylline by Lai et al. For aqueous samples the lowest detection limit was estimated at 0.4 mg mL^{-1} [57].

Detection of medium-size analytes

Examples of medium-size analytes detected by SPR biosensor technology include food safety-related analytes such as staphylococcal enterotoxin B, botulinum toxin, and *E. coli* enterotoxin. Choi et al. demonstrated a direct SPR biosensor for botulinum toxin using a commercial SPR biosensor (Biacore X) and monoclonal antibodies; this biosensor was able to detect botulinum toxin in buffer at a concentration of 2.5 μg mL^{-1} [71]. Spangler et al. demonstrated direct detection of *E. coli* enterotoxin in aqueous solutions; the lowest detection limit was established to be 6 μg mL^{-1} [72]. Detection of staphylococcal

enterotoxin B was performed using a commercial angular sensor (Biacore 3000) [73] and laboratory wavelength modulation-based SPR sensors [74]. The lowest detection limits were 1–10 ng mL^{-1} (in milk and meat) [73], 5 ng mL^{-1} (direct detection in buffer), and 0.5 ng mL^{-1} (sandwich assay in buffer and milk) [74]. A typical sensorgram for detection of Staphylococcal enterotoxins B (SEB) is shown in Fig. 16 [74]. Figure 17a shows the equilibrium sensor response for both the direct capture of SEB and amplification by secondary antibodies as a function of SEB concentration. The use of secondary antibodies provides 10-fold increase in the sensor response. In Fig. 17b, initial binding rates for SEB and secondary antibody concentration are shown for several SEB concentrations [74].

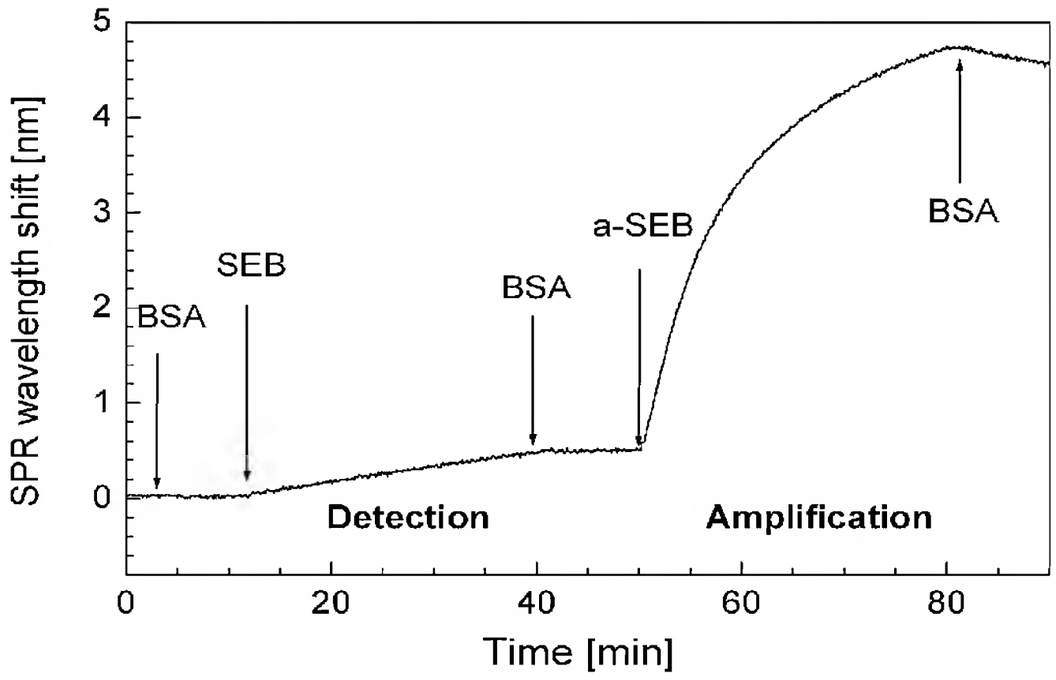

Fig. 16 Detection of Staphylococcal enterotoxin B using sandwich assay. Kinetic response [74]

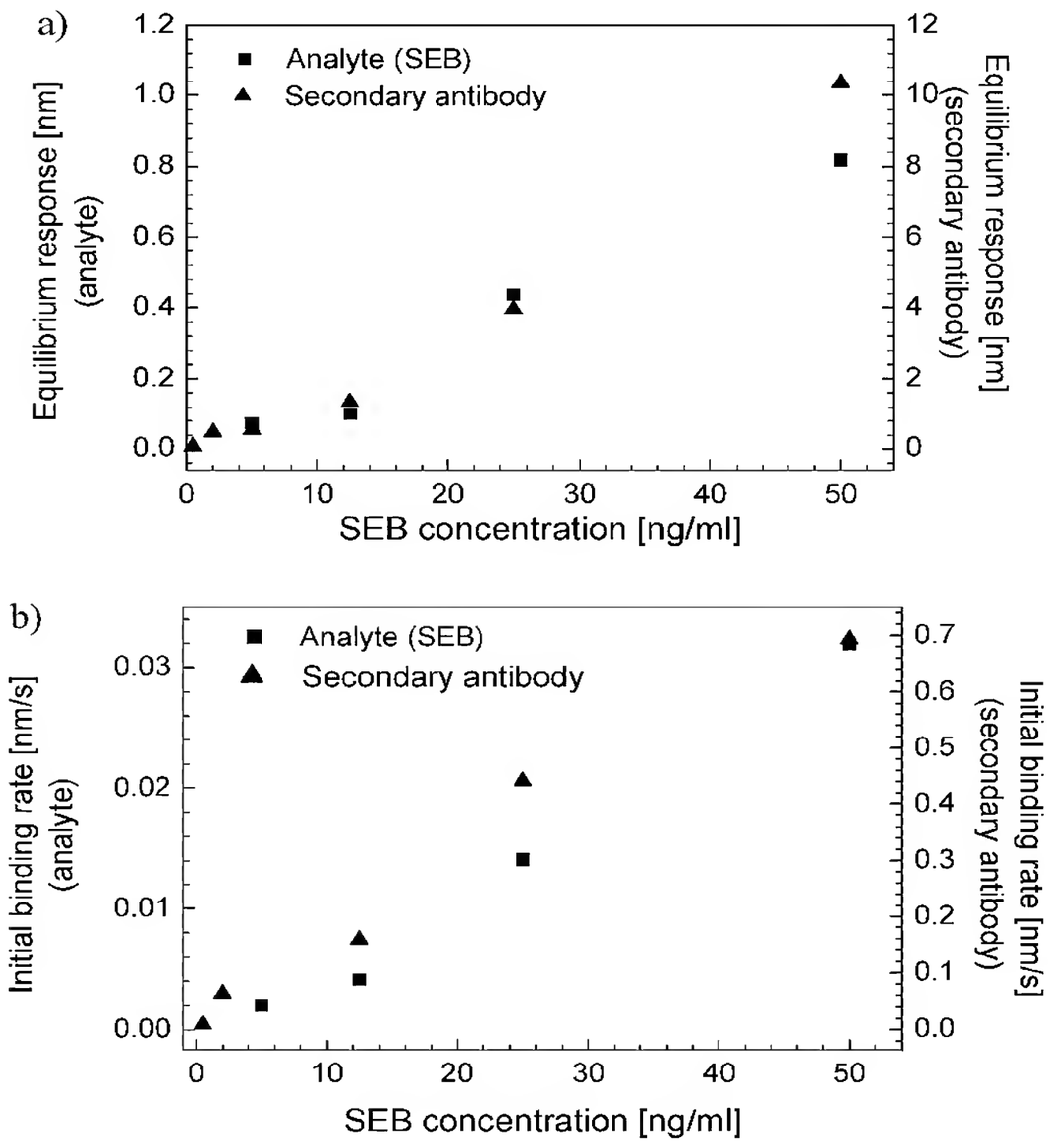

Fig. 17 Detection of Staphylococcal enterotoxin B. (**a**) Equilibrium response for different concentrations of SEB. (**b**) Initial binding rate for different concentrations of SEB [74]

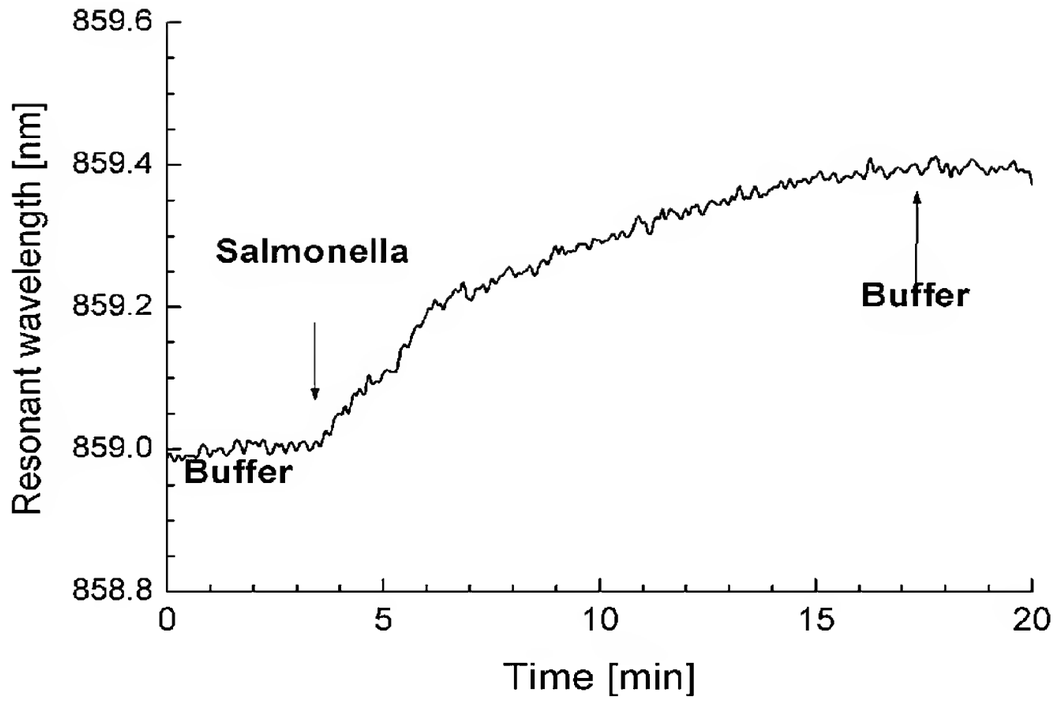

Fig. 18 Direct detection of *Salmonella enteritidis*. Kinetic response to Salmonella at a concentration of 10^6 cfu mL^{-1}

Detection of large analytes

Representatives of large analytes targeted by SPR biosensor technology include bacterial pathogens such as *Escherichia coli*, *Salmonella enteritidis*, and *Listeria monocytogenes*. Detection of *Escherichia coli* O157:H7 was performed by Fratamico et al. who used an angular-modulation commercial SPR sensor and sandwich assay [75]. They used monoclonal antibodies immobilized on the sensor surface for capturing *E. coli* and polyclonal secondary antibodies for enhancing the specific sensor response. The lowest detection limit for *E. coli* was established at 5×10^7 cfu mL^{-1}. Direct detection of *Salmonella enteritidis* and *Listeria monocytogenes* at concentrations down to 10^6 cfu mL^{-1} was demonstrated by Koubová et al. using a laboratory wavelength-modulated SPR sensor and monoclonal antibodies [76]. A sensorgram illustrating direct detection of *Salmonella enteritidis* is shown in Fig. 18.

The main challenges in detecting bacterial analytes at lower levels include the low concentration of a particular antigen relative to total cellular material and slow diffusion of bacterial cells to sensor surface [77].

Commercialization of SPR biosensors

The first commercial SPR biosensor was launched by Biacore International AB in 1990. In the following decade, Biacore has developed a range of laboratory SPR instruments (Biacore 1000, Biacore 2000, Biacore 3000, Biacore C, Biacore X, Biacore J, Biacore Q) [78]. Most recently the Biacore S51 has been developed which offers

higher sensitivity and throughput. Other SPR sensors have been developed by British Windsor Scientific (IBIS) [79], Nippon Laser and Electronics Laboratory (SPR-670 and SPR-CELLIA) [80], Texas Instruments (Spreeta) [81], and Analytical μ-Systems (BIO-SUPLAR 2) [82].

Outlook

Over the past ten years, surface plasmon resonance (SPR) biosensor technology has made great strides, and a large number of SPR sensor platforms, biomolecular recognition elements, and measurement formats have been developed. There has been growing interest in commercialization of SPR biosensor technology leading to a number of systems available on today's market. SPR biosensors have played a significant role in research into biomolecules and their interactions and have been increasingly used for detection and identification of chemical and biological substances. SPR biosensors have been particularly successful for detection of small and medium size analytes, a number of which have been detected at practically relevant levels. Detection limits for large analytes such as bacteria and viruses still need to be improved to meet today's needs.

Undoubtedly, future development of SPR biosensors will be driven by the needs of the consumer. SPR biosensor technology has the potential to benefit numerous important fields including pharmaceutical research, medical diagnostics, environmental monitoring, food safety, and security. Applications in these areas present unique challenges and impose special requirement on analytical technologies. Pharmaceutical research, which was fast to adopt optical biosensors, needs laboratory-based high-throughput systems with high sensitivity to facilitate parallel screening. Medicine would benefit from high-throughput diagnostic tools for centralized laboratories and from compact diagnostic systems dedicated to selected diagnostic applications which could be used at clinics. In addition, there is a growing interest in tools for home medical (self-) diagnostics. Mobile analytical systems enabling rapid detection of food-borne pathogens in food would be important for food producers, processors, distributors and regulatory agencies and thus benefit the food safety. Environmental monitoring would benefit from detection systems which could be deployed in the field for continuous monitoring and from mobile systems enabling fast identification of environmental threat. SPR biosensors could also play an important role in defense, where fast, portable and rugged units are needed for early detection and identification of biological warfare agents in the field. Development of these systems will require significant advances in miniaturization of SPR biosensing platforms, development of robust biomolecular recognition elements with high specificity and long storage life, integration of SPR sensor platforms with microfluidic devices, and application-specific sampling systems.

Acknowledgement This work was supported by the Grant Agency of the Czech Republic under contracts 102/03/0633, 303/03/0249, and 203/02/1326.

References

1. Ghindilis AL, Atanasov P, Wilkins M, Wilkins E (1998) Biosens Bioelectron 13:113–131
2. Chu X, Lin ZH, Shen GL, Yu RQM (1995) Analyst 120: 2829–2832
3. Gauglitz G (1996) Opto-chemical and opto-immuno sensors, sensor update, vol 1. VCH, Weinheim
4. Rowe-Taitt CA, Hazzard JW, Hoffman KE, Cras JJ, Golden JP, Ligler FS (2000) Biosens Bioelectron 15:579–589
5. Piehler J, Brecht A, Gauglitz G (1996) Anal Chem 68:139–143
6. Heideman RG, Kooyman RPH, Greve J (1993) Sens Actuators B 10:209–217
7. Clerc D, Lukosz W (1994) Sens Actuators B 19:581–586
8. Cush R, Cronin JM, Stewart WJ, Maule CH, Molloy J, Goddard NJ (1993) Biosens Bioelectron 8:347–353
9. Homola J, Yee S, Gauglitz G (1999) Sens Actuators B 54:3–15
10. Homola J, Yee S, Myszka D (2002) Surface plasmon biosensors. In: Ligler FS, Taitt CR (eds) Optical biosensors: present and future. Elsevier
11. Rabbany SY, Lane WJ, Marganski WA, Kusterbeck AW, Ligler FS (2000) J Immunol Methods 246:69–77
12. Boardman AD (1982) (ed) Electromagnetic surface modes. Wiley, Chichester
13. Reather H (1983) Surface plasmons on smooth and rough surfaces and on gratings, Springer tracts in modern physics, vol 111. Springer, Berlin Heidelberg New York
14. Snyder AW, Love JD (1983) Optical waveguide theory. Chapman and Hall, London
15. Parriaux O, Voirin G (1990) Sens Actuators A 21–23:1137
16. Hutley MC (1982) Diffration gratings. Academic Press, London
17. Kooyman RPH, Kolkman H, van Gent J, Greve J (1988) Anal Chim Acta 213:35–45
18. Yeatman EM (1996) Biosens Bioelectron 11:635–649
19. Homola J (1997) Sens Actuators B 41:207–211
20. Homola J, Koudela I, Yee S (1999) Sens Actuators B 54:16–24
21. Edwards PR, Leatherbarrow RJ (1997) Anal Biochem 246:1–6
22. Vijayendran RA, Ligler FS, Leckband DE (1999) Anal Chem 71:5405–5412
23. Löfås S, Malmqvist M, Rönnberg I, Stenberg E, Liedberg B, Lundström I (1991) Sens Actuators B 5:79
24. Nenninger GG, Clendenning JB, Furlong CE, Yee S (1998) Sens Actuators B51:38
25. Jordan CE, Frutos AG, Thiel AJ, Corn RM (1997) Anal Chem 69:4939
26. Nikitin PI, Beloglazov AA, Kabashin AV, Valeiko MV, Kochergin V E (1999) Sens Actuators B54:43
27. Kano H, Knoll W (2000) Optics Communications 182:11–15
28. Kabashin A V, Nikitin P I (1998) Opt Commun 150:5–8
29. Nelson BP, Frutos AG, Brockman JM, Corn RM (1999) Anal Chem 71:3928–3934
30. Johnasen K, Arwin H, Lundström I, Liedberg B (2000) Rev Sci Instrum 71:3530–3538
31. Rothenhäusler B, Knoll W (1988) Nature 332:688
32. Dostálek J, Homola J, Miler M (2002) EUROPT(R)ODE VI, Manchester, UK, Book of Abstracts, 265
33. Homola J, Dostálek J, Čtyroký J (2001) Proc SPIE 4416:86
34. Homola J, Lu HB, Yee S (1999) Electr Lett 35:1105
35. Homola J, Lu HB, Nenninger GG, Dostálek J, Yee S (2001) Sens Actuators B76:403–410
36. Ober RJ, Ward E S (1999) Anal Biochem 271:70–80
37. Homola J, Dostálek J, Piliarik M, Yee S (2002) EUROPT(R)ODE VI, Manchester, UK, Book of Abstracts, 71
38. Stemmler I, Brecht A, Gauglitz G (1999) Sens Actuators B 54:98–105
39. Jorgenson RC, Yee S (1993) Sens Actuators B12:213
40. Homola J (1995) Sens Actuators B 29:401–405
41. Homola J, Piliarik M, Slavík R, Čtyroký J (2001) SPIE Proc 4416:82–85
42. Piliarik M, Homola J, Maníková Z, Čtyroký J (2003) Sens Actuators B 90:236–242

43. Nenninger GG, Tobiška P, Homola J, Yee S (2001) Sens Actuators B74:145
44. Liedberg B, Lundstrom I, Stenberg E (1993) Sens Actuators B11:63
45. Johnston KS, Booksh KS, Chinowsky TM, Yee S (1999) Sens Actuators B 54:80–88
46. Chinowsky TM, Jung LS, Yee S (1999) Sens Actuators B 54: 89–97
47. Johansen K, Stålberg R, Lunström I, Liedberg B (2000) Meas Sci Technol 11:1630–1638
48. Johansen K, Lundström I, Liedberg B (2000) Biosens Bioelectron 15:503–509
49. Nenninger GG, Piliarik M, Homola J (2002) Meas Sci Technol 13:2038–2046
50. Morgan H, Taylor DM, (1992) Biosens Bioelectron 7:405–410
51. Duschl C, Sevin-Landais A, Vogel H (1995) Biophys J 70: 1985
52. Löfås S, Malmqvist M, Rönnberg I, Stenberg E, Liedberg B, Lundström I (1991) Sens Actuators B 5:79
53. Nakamura R, Muguruma H, Ikebukuro K, Sasaki S, Nagata R, Karube I, Pedersen H (1997) Anal Chem 69:4649
54. Lu HB, Homola J, Campbell CT, Nenninger GG, Yee S, Ratner BD (2001) Sens Actuators B 74:91–99
55. Watts HJ, Yeung D, Parkes H (1995) Anal Chem 67:4283–4289
56. Brockman JM, Frutos AG, Corn RM (1999) J Am Chem Soc 121:8044–8051
57. Lai EPC, Fafara A, VanderNoot VA, Kono M, Polsky B (1998) Can J Chem 76:265–273
58. Rich RL, Myszka DG (2002) J Mol Recognit 15:352–376
59. Severs AH, Schasfoort RBM (1993) Biosens Bioelectron 8:365
60. Leung PT, Pollard-Knight D, Malan GP, Finlan MF (1994) Sens Actuators B22:175
61. Minunni M, Mascini M (1993) Anal Lett 26:1441
62. Mouvet C, Harris RD, Maciag C, Luff BJ, Wilkinson JS, Piehler J, Brecht A, Gauglitz G, Abuknesha R, Ismail G (1997) Anal Chim Acta 338:109
63. Harris RD, Luff BJ, Wilkinson JS, Piehler J, Brecht A, Gauglitz G, Abuknesha RA (1999) Biosens Bioelectron 14:377
64. Miura N, Ogata K, Sakai G, Uda T, Yamazoe N (1997) Chem Lett 8:713
65. Sakai G, Nakata S, Uda T, Miura N, Yamazoe N (1999) Electrochim Acta 44:3849
66. Mullett W, Edward PC, Yeung MJ (1998) Anal Biochem 258: 161–167
67. Sternesjo A, Mellgren C, Bjorck L (1996) ACS Symp Ser 621:463–470
68. Gaudin V, Pavy M-L (1999) JAOAC Int 82:1316–1320
69. Baxter GA, Ferguson JP, O'Conner MC, Elliott CT (2001) J Agric Food Chem 49:3204–3207
70. Elliot CT, Baxter GA, Crooks SRH, McCaughey WJ (1999) Food Agric Immunol 11:19–28
71. Choi K, Seo W, Cha S, Choi J (1998) J Biochem Mol Biol 31:101–105
72. Spangler BD, Wilkinson EA, Murphy JT, Tyler BJ (2001) Anal Chim Acta 444:149–161
73. Rasooly A (2001) J Food Prot 64:37–43
74. Homola J, Dostálek J, Chen S, Rasooly A, Jiang S, Yee S (2002) Int J Food Microbiol 75:61–69
75. Fratamico PM, Strobaugh TP, Medina MB, Gehring AG (1998) Biotechnol Tech 12:571–576
76. Koubová V, Brynda E, Karasová L, Škvor J, Homola J, Dostálek J, Tobiška P, Rošický J (2001) Sens Actuators B 74: 100–105
77. Perkins EA, Squirrell DJ (2000) Biosens Bioelectron 14:853
78. Biacore websitewww.biacore.com
79. IBIS Technologies website www.ibis-spr.nl
80. Nippon Laser and Electronics Laboratory website www.nle-lab.co.jp/English/ZO-HOME.htm
81. Texas Instruments website www.ti.com/sc/docs/products/msp/control/spreeta
82. Analytical μ-Systems website www.micro-systems.de